UNIVERSITY OF NAPLES FEDERICO II

PH.D. THESIS IN

INDUSTRIAL PRODUCT AND PROCESS ENGINEERING

DEPARTMENT OF CHEMICAL, MATERIALS AND INDUSTRIAL PRODUCTION ENGINEERING (DICMAPI)

XXXV CYCLE

Elucidation of TFEB nuclear translocation dynamics in human cells by means of Quantitative Modelling and Microfluidics

Supervisor
Ch.mo Prof. Diego di Bernardo

Candidate
Iacopo Ruolo
Matr. DR993926

ACADEMIC YEAR 2022/2023

Abstract

Mammalian cells are dynamic systems capable of detecting, adjusting and responding to time-varying inputs. Transcriptional regulatory networks, which are important for directing cell homeostasis response to environmental stimuli, acquire information about the extracellular and intracellular environments via signaling pathways, which are critical in cell state regulation. The nucleo-cytoplasmic shuttling of transcription factors allows the cell to control how genes are expressed in response to its environment.

The Transcription Factor EB (TFEB) has recently been discovered as a master regulator in the transcriptional control of lysosomal biogenesis and autophagy in response to starvation. The kinase mTOR controls TFEB activity. In nutrient-rich conditions, mTOR sequesters TFEB in the cytoplasm and phosphorylates it there. Unphosphorylated TFEB translocates into the nucleus and controls the expression of its target genes when mTOR is suppressed during starvation.

The purpose of this Thesis is to characterize the dynamics of TFEB nuclear shuttling on the basis of experimental and computational investigations, in line with the general framework of Systems Biology.

Specifically, I took advantage of the experimental data to study the nuclear localisation of TFEB in real time on individual cells growing in two complementary microfluidics-based platforms. Following starvation, TFEB translocates to the nucleus but later partially relocalises to the cytoplasm, exhibiting a previously unknown "overshoot" dynamic. These experimental features were then employed in the subsequent modelling efforts aiming at discriminating among alternative hypotheses that most likely explain the experimental results, and thus help determine the mechanism that is responsible for the observed shuttling dynamics. The results suggest that Calcium-Calcineurin signaling drives TFEB overshoot

dynamic.

In this Thesis, I will introduce the Systems Biology fundamentals and I will review TFEB signalling in Chapter 1; I will then describe the technological experimental platform in Chapter 2. Here, I will also provide details on the methods used to conduct experimental and computational analyses, including the image analysis algorithms and the modelling approach. Chapters 3 and 4 will represent the body of the Thesis. Particularly, I will focus on the experimental data in the former (Chapter 3), starting with the preliminary data that revealed the overshoot dynamics, and consequently I will explain the experiments that followed and that were based on the suppression of critical TFEB signaling regulators to identify the source of this novel mechanism. In Chapter 4, I will investigate and explore *in silico* the role of each individual reaction involved in TFEB nuclear shuttling which has been reported in literature and derive the optimal model based on the preexisting literature to recapitulate the experimental features. Finally, in Chapter 5, I will provide some concluding remarks on future studies to empirically verify the computational results I obtained.

Contents

List of Figures

List of Tables

Chapter 1

Introduction

Transcription factor EB (TFEB) has been identified as as a key player in the transcriptional regulation of lysosomal biogenesis and autophagy. It controls different biological processes, has diverse functions in numerous signaling pathways, and has been connected to a variety of human disorders.

Several studies revealed how complicated and sophisticated TFEB signaling is. With the aim to explore and characterize its behaviour following nutrient deprivation stimuli, I chose to study its translocation dynamics using a novel approach from the field of Systems Biology, which combines theoretical mathematical modeling with high-throughput experimental measurements to elucidate biological functions.

In this Chapter, I will first introduce the concept of Systems Biology, describing the general approach and the rational behind this novel research field. Then, I will introduce the functions and the signalling of the biological system under investigation.

1.1 Introduction to Systems Biology

Any biological system is composed of a variety of physical components, or parts, that influence one another through their interaction and are physically and functionally separated from their surroundings [98].

Within a cell, gene products do not work alone, while cells isolated from their tissue lose a lot of their structural and functional characteristics.

Most biological processes are governed by multi-scale dynamic complex systems made of interacting macromolecules and metabolites. These interactions between macromolecules, both locally and globally, are able to produce system characteristics and behaviors that are essential for life [102].

Networks of interactions between proteins, RNA, DNA, and small molecules involved in signaling and energy transfer can be seen as the building blocks of cell life.

Through the processing of external information and the induction of appropriate cellular responses and internal activities, such as gene expression, these networks enable the fundamental operations of cells and complete organisms. Signals that transport data from the environment are inputs to the networks.

The transcriptional network is a dynamic system because a cell is not an isolated system; it continuously responds to external stimuli in order to either follow a specific developmental program or to adapt to changes in the environmental conditions. When an input signal is received, transcription factor activities change thus modifying the rate at which proteins are produced [2].

By their very nature, biological systems are resistant to accurate quantitative and mathematical representation. They are made up of several components that are intricately related through interactions and activities that occur at various organizational levels (molecular,cellular,in tissue, whole animals and ecological). Due to the presence of several gradients that are outside of the thermodynamic equilibrium, these processes take place simultaneously in an open system and ultimately result in very complex non-linear dynamics between the system's components. The employment of mathematical models in a quantitative and dynamic way to comprehend biological systems has been hampered by this scenario.

However, two technical developments in the last two decades have made it possible to build and resolve mathematical models for biological systems. The processing capacity necessary for the administration of information and the calculation of massive systems is generally accessible and nearly ubiquitous. On the other hand, a lot of dynamic information on the structure and behavior of biological systems has been produced as a result of the advancement of high throughput methods to measure level of protein, RNA, and DNA on a

gene-by-gene basis as well as the post-translational modification and localisation of proteins, and not the least the development of the "omics" sciences (genomics, transcriptomics, proteomics, signalomics, and metabolomics).

Progress in molecular biology, particularly in genome sequencing and high-throughput measurements, enables us to collect comprehensive data sets on system performance and learn more about the underlying molecules. It is now cheaper and simpler than ever to gather, process, and store this information. All of the aforementioned factors have contributed to the emergence of Systems Biology as the multidisciplinary, quantitative method to studying the complex relationships and collective behavior of a cell, an organism, or an ecosystem in the twenty-first century. The focus on organization and biological function is what makes Systems Biology unique [38, 39, 98].

Research using a Systems Biology perspective is less concerned with the parts as they are seen individually and more concerned with the connections between the structural elements of biological systems and their function as well as the characteristics of the interactions that take place between various sub-systems. Systems Biology focuses on the problem of reconstructing and integrating the available biological data [98].

Systems Biology is a comprehensive quantitative analysis of the manner in which all the components of a biological system interact functionally over time [1].

It is the study of how complex biological structures and processes behave in terms of their underlying molecular elements. It is based on physiology for its special interest in adaptive states of the cell and organism, on developmental biology for the significance of defining a succession of physiological states in that process, and on evolutionary biology and ecology for the understanding that all aspects of the organism are products of selection, a selection we rarely understand on a molecular level. It is also based on molecular biology for its special concern for information transfer.

In order to identify and characterize parts and investigate how their interactions with one another and the environment contribute to the maintenance of the entire system, Systems Biology is a method of biomedical research that consciously combines reduction and integration of information across various spatial scales.

Systems Biology provides a window into how evolution has shaped the phenotype by

relating genomes and phenotypes, which are connected in both directions through intricate networks of interaction.

All of this is attempted by Systems Biology using numerical measurement, modeling, reconstruction, and theory. Without the use of advanced computer modeling tools, it would be difficult to investigate the landscapes made up of highly dynamic and mutually interacting characteristics [38, 40].

The Systems Biology method relies on mathematical modeling to depict and comprehend the intricate relationships between various biological entities and components and to analyze the cellular systems dynamically. The general approach used in Systems Biology is depicted in Figure 1.1.

Mathematical modeling becomes a means to analyze the structure and dynamics of cellular and organismal activity in order to comprehend biology at the system level. Because dynamic analysis can provide helpful predictions of previously undiscovered relationships, study of dynamics and structure based on network dynamics are really overlapping processes [39, 40].

A model is an abstract or numerical representation of a system used to analyze and characterize it. Every model is a simplified form of the reference system that the scientist is trying to comprehend and measure. In the end, it serves as a method of organizing the information and facts that are currently known and understood about a certain occurrence.

The nature of mathematical models might vary greatly. Dynamical models, which may be divided into deterministic and stochastic types, take changes in the elements over time into account. The concentration of the species and the model's parameters are the sole factors affecting the dynamics in the deterministic ones. The stochastic ones, on the other hand, depend on the random noise of the system since there is uncertainty in systems with statistically uncommon constituents. Static models aim to comprehend the organization of the connectivity of the elements, which remains constant across time under particular circumstances. By identifying the key hypotheses and deriving insights into the complex biological processes they represent, mathematical models not only aid in system understanding but also enable the study of the effects of modifications to the system's components and environmental factors on its behavior [98].

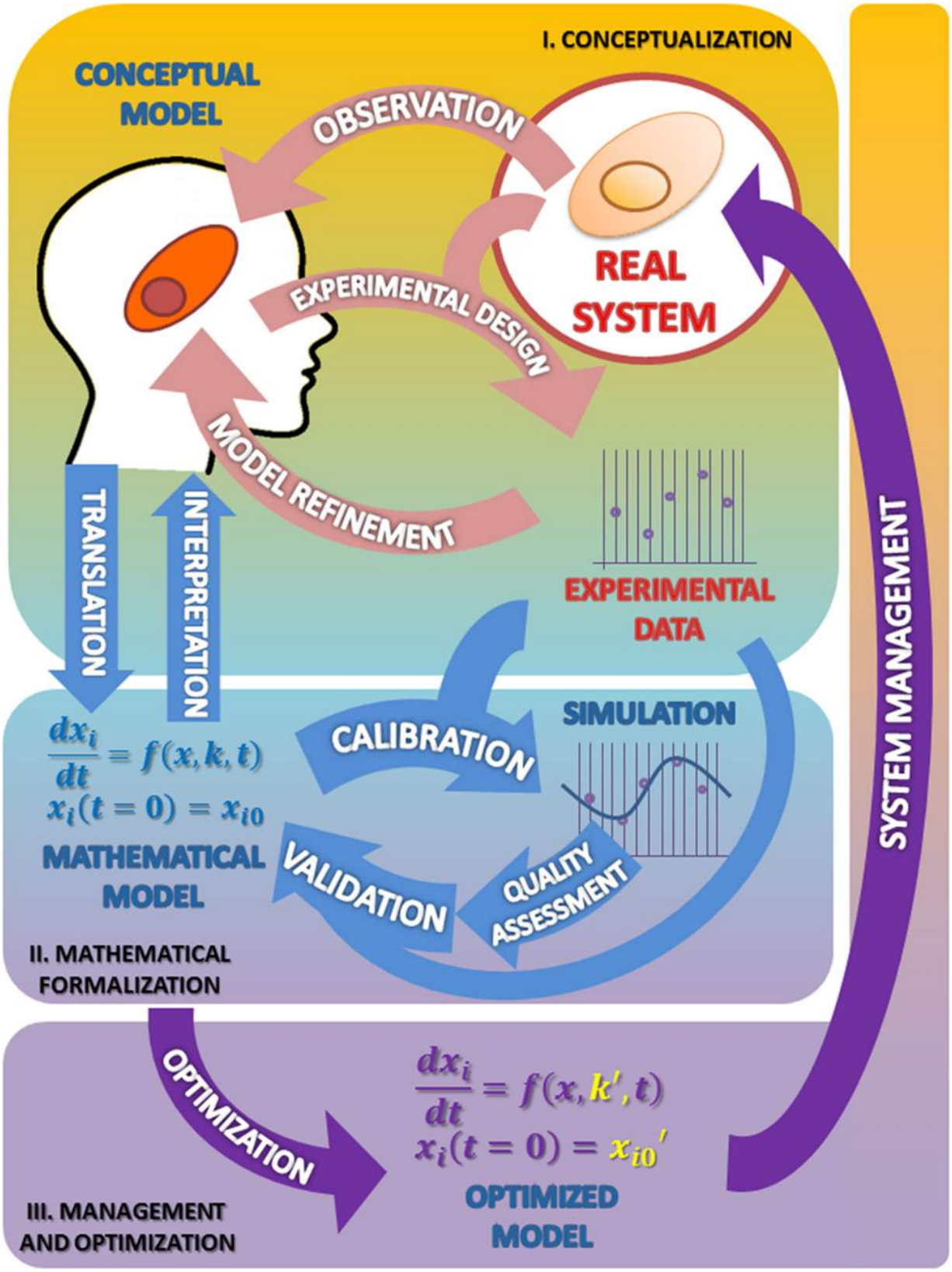

Figure 1.1: **Systems biology approach.** Systems biology aims to interpret and analyse signalling pathways and biological systems relying on experimental and computational analysis. The primary steps in this process are observation, then mathematical modeling, simulation, analysis, and optimization, before turning to observation. In this cycle, the mathematical model is in the center, directly behind the actual system. From [98]].

The essential steps are observation, mathematical modeling, simulation, analysis, and optimization, followed by a return to observation. The model is built in stages, with the first version presenting an initial selection of variables, processes, and interactions that are thought to be relevant based on the information at hand and a set of well-founded hypotheses (conceptual model). The model's first mathematical formulation is drawn from this suggestion (mathematical model). To get here, it is necessary to exercise the integration of theories and data, which results in a new, deeper level of understanding of the system [98].

Complex biological systems constitute a challenge because, based on our current understanding, models are still incredibly incomplete. In order to enhance models and calibrate confidence, there will therefore be a role for both positive and negative validation for some time to come [40].

Once the model is complete and precise, it is feasible to predict how the system will behave in the presence of any disturbance [1].

Systems Biology is still in its early stage, but it has immense promise for both scientific and practical advancement. A shift in biology from the molecular to the system level promises to transform our understanding of intricate biological regulatory systems and open up a wealth of new prospects for the application of this knowledge in real-world settings [39].

1.2 Introduction to the transcription factor EB (TFEB)

Transcription factor EB (TFEB), a member of the MiT/TFE family of basic helix-loop-helix leucine zipper transcription factors, is a well-known essential regulator of the autophagy/lysosomal-to-nucleus signaling pathway. Because of its extensive involvement in numerous signaling pathways, including the mTORC1, Wnt, calcium, and AKT signaling pathways, TFEB is now widely recognized as a regulator of various processes, including energy homeostasis, stress response, metabolism, autophagy and lysosomal biogenesis. TFEB was first identified as an oncogene. Additionally, TFEB has been linked to a number of human diseases, including cancer, lysosomal storage disorders, neurodegenerative

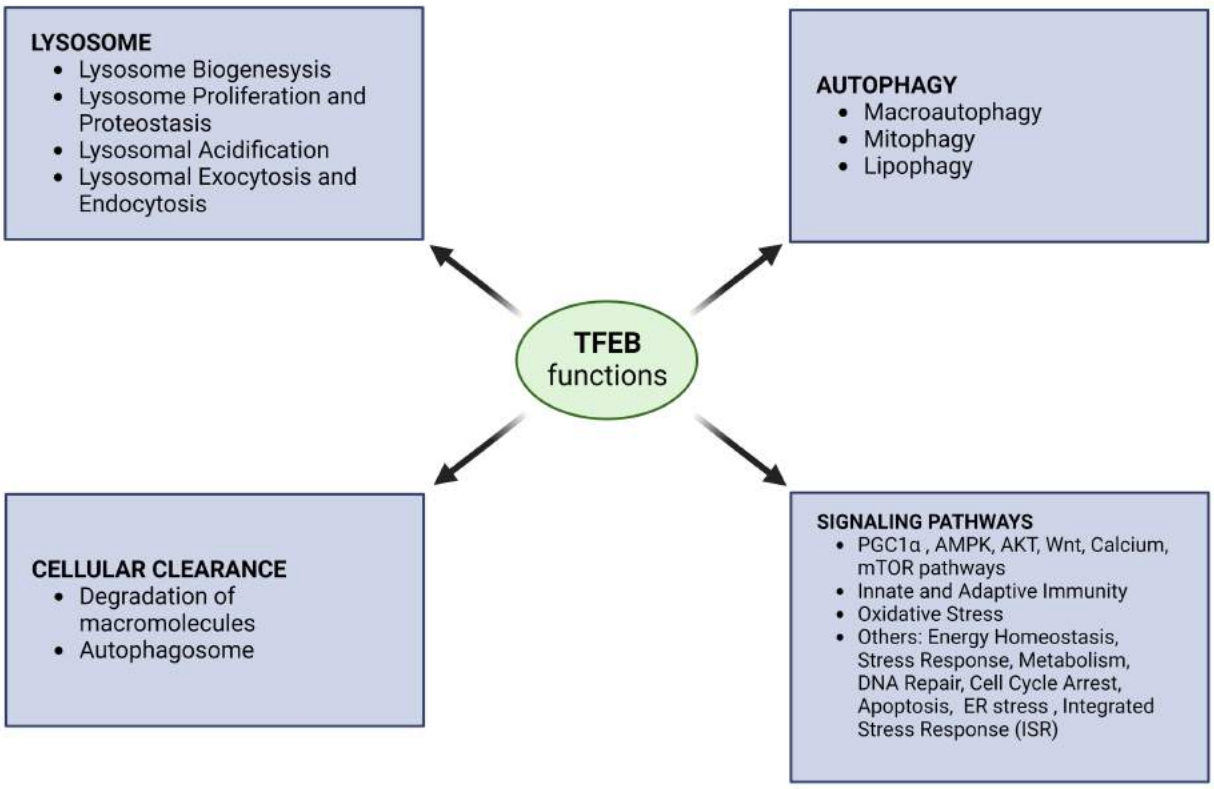

Figure 1.2: **TFEB functions.** The majority of cellular processes controlled by TFEB activity are shown in the picture, including lysosome formation and function, autophagy, mitophagy, lipophagy, lysosomal exocytosis, and endocytosis, as well as a number of signaling pathways. Adapted from [7, 8]].

diseases, and metabolic disorders. Consequently, it has been identified as a potential novel therapeutic target for clinical and regenerative applications [97].

1.2.1 TFEB functions

Evolutionarily, TFEB and the other MiT/TFE proteins are conserved. The expression of the MiT/TFE transcription factors varies greatly depending on the cell types and tissues, and they are ubiquitously expressed. A palindromic ten base pair motif (GTCACGTGAC), known as the coordinated lysosomal expression and regulation (CLEAR) element, has been found to be preferred by MiT/TFE proteins, according to extensive investigation of the promoters of several autophagy-lysosomal genes [8, 64, 76, 97].

A number of genes with the CLEAR regulatory motif in their proximal promoters have been demonstrated to be positively affected by TFEB's direct binding. The primary TFEB roles in cellular processes are reported in Figure 1.2. TFEB positively controls the

expression of lysosomal genes and produces an increase in the number of lysosomes, which enhances the capacity of cells to digest lysosomal substrates. This is consistent with its function as a modulator of the CLEAR network genes [86]. Additionally, TFEB controls the expression of other genes that contribute to an increase in the autophagic flux and lysosomal exocytosis [58, 89].

Therefore, the lysosomal biogenesis, autophagy, and lysosomal exocytosis processes are all modulated by TFEB, which controls a transcriptional program that can govern the major cellular degradative pathways and encourage intracellular clearance.

More recently, it has been shown that TFEB also affects lysosomal positioning, causing them to shift toward the cell's center in response to nutrient restriction [103], as well as endocytic gene expression, which increases cellular endocytosis and activates autophagic processes [67]. Additionally, it was recently shown that TFEB participates in DNA damage response, enhancing p53-dependent transcription of genes involved in DNA repair, cell cycle arrest, and apoptosis, as well as ER stress response by promoting apoptosis [11,53]. TFEB role was also demonstrated in autophagy and lysosome-dependent cell death (LDCD), lipid catabolic pathways (such as fatty acid oxidation and lipophagy) and in lysosomal-independent autophagy [76, 97].

It is interesting to note that many factors that control TFEB activity, such as RagD, the lysosomal "platform", and the Ca^{2+} channel MCOLN1, are also transcriptionally controlled by TFEB. This suggests that lysosomal adaptation to environmental changes is a self-sustaining process that is controlled by numerous feedback loops [20, 90]. As an additional feedback loop that helps to maintain lysosomal signaling and function, TFEB activation also stimulates its own transcription [90].

As nexus for nutritional sensing and resolution of any supply-demand imbalance, TFEB can also improve the integrated stress response (ISR) in addition to increasing lysosome formation in response to amino acid restriction. In fact, amino acid deprivation causes the ISR pathway to be repressed, reducing the cell's overall rate of protein synthesis. However, because it is a transcription factor, TFEB needs protein synthesis to control the autophagic flow, which is in competition with the inhibition of all translation. To do this, TFEB regulates GADD34 transcriptionally to allow translation of the starvation-induced

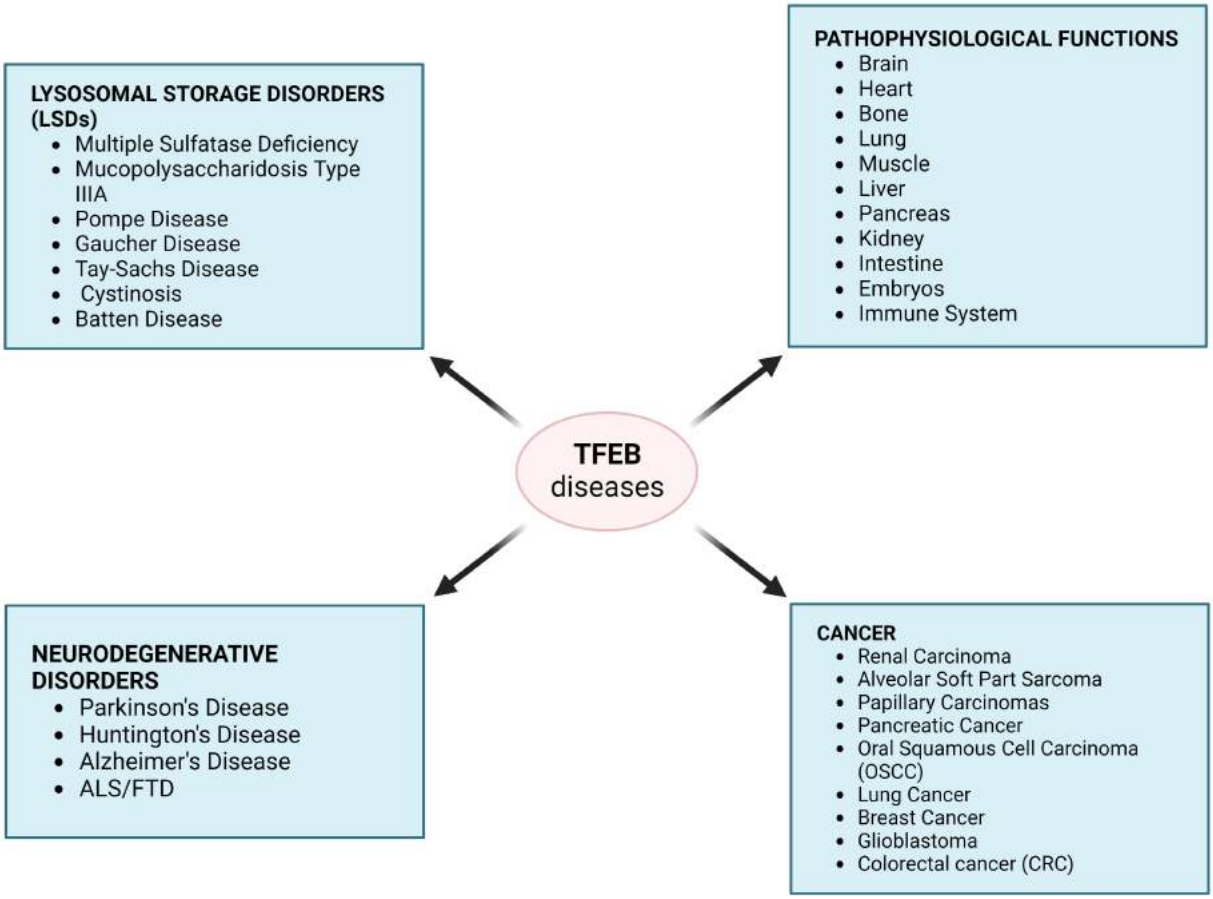

Figure 1.3: **TFEB in disease.** A number of disorders, such as Lysosomal Storage Disorders (LSDs), neurodegenerative illnesses, and many cancer types are affected by TFEB disfunctions, which also has a physiological effect on a number of different organs and tissues. Adapted from [8, 97]].

transcriptional program, which in turn fine-tunes protein synthesis during starvation [27].

Finally, the physiological impact of TFEB protein was observed in a variety of organs and tissues including brain, heart, bone, lung, muscle, liver, pancreas, kidney, intestine, embryos and immune system [76, 97].

1.2.2 TFEB in diseases

In many clinical disorders linked to autophagy or lysosomal abnormalities, TFEB has emerged as a significant factor because of its capacity to enhance intracellular clearance [8, 76, 97]. TFEB roles in disease are reported in Figure 1.3.

The pathological phenotype of Lysosomal Storage Disorders (LSDs), a class of diseases brought on by genetic defects in particular lysosomal proteins that result in the accumulation of toxic aggregates inside the lysosomal lumen, has been shown to be improved by inducing

TFEB activity in cellular or mouse models [50, 69, 70].

Accordingly, TFEB overexpression enhanced lysosomal function and autophagy in models of multiple sulfatase deficiency, mucopolysaccharidosis type IIIA, Batten disease, Pompe disease, Gaucher disease, Tay-Sachs disease, and cystinosis by promoting a significant decrease in undigested material. [58, 78, 94, 95].

In addition to LSDs, it has been demonstrated that TFEB activity induction is advantageous in neurodegenerative disorders including Parkinson's, Huntington's, and Alzheimer's disease. Toxic protein aggregation, which is frequently brought on by or linked to abnormalities in autophagy or lysosomal function, is a hallmark of these diseases [60]. Genetic or pharmacological activation of TFEB in Parkinson's disease decreases the buildup of α-synuclein aggregates and restores healthy lysosome activity [17, 18, 36]. At the same way, TFEB activation reduces protein aggregation and enhances the neurological phenotype in Huntington's disease models [86, 99]. Finally, in cellular and mouse models of Alzheimer's disease, overexpression or activation of TFEB prevents aggregate formation and neurodegeneration [13, 73, 104, 105].

Additionally, it was demonstrated that TFEB overexpression helped various liver diseases, such as α1-antitrypsin deficiency and obesity, by enhancing autophagy or lipophagy [71,90], respectively.

New research suggests that cancer cells use TFEB-mediated transcriptional stimulation of autophagy-lysosomal biogenesis for their oncogenic survival. TFEB was specifically linked to many cancer forms, including renal carcinoma [4,15,44], alveolar soft part sarcoma [45], papillary carcinomas with liver metastases [12] pancreatic ductal adenocarcinoma (PDAC) tumorigenesis and pancreatic cancer cell proliferation [51, 72], besides of Birt-Hogg-Dubé (BHD) syndrome [63]. Oral squamous cell carcinoma (OSCC) and non-small cell lung cancer (NSCLC) cell lines with TFEB depletion showed decreased migratory and invasive behaviors, indicating that it may control cellular migration [28, 82]. Finally, in another study, p53, a tumor suppressor, was found to regulate the TFEB-dependent autophagy-lysosomal pathway in lung cancer cells [109].

1.2.3 Conditions that promote TFEB nucleo-cytoplasmic shuttling

By controlling its subcellular location through post-translational modifications, protein-protein interactions, and spatial organization, TFEB activity is rigorously regulated. When inactive, TFEB is primarily positioned in the cytosol, but specific stimuli quickly cause TFEB to go into the nucleus, where it then activates the transcription of its target genes [8, 76, 89].

In cells fed with sucrose, which accumulates in lysosomes and replicates the lysosomal accumulation seen in lysosomal storage diseases, the first proof of stimulus-induced TFEB nucleo-cytoplasmic shuttling was discovered [86]. Other pharmacological treatments that result in lysosomal stress, such as chloroquine, bafilomycin or trehalose, also cause TFEB nuclear translocation [69, 79, 91].

TFEB localisation was demonstrated to be extremely sensitive to nutrient levels in addition to lysosomal stress. As a result, nutrient restriction triggers a quick and powerful nuclear translocation of TFEB, which peaks about an hour after amino acid and serum withdrawal. Additionally, refeeding cells with nutrients causes TFEB nucleus-to-cytoplasm relocalisation [52, 79, 89]. Many other stimuli have been demonstrated to promote TFEB translocation in addition to lysosomal stress and starvation, including infection, bacterial phagocytosis, inflammation, physical exercise, mitochondrial damage and ER stress [76]. Recently, other drug treatment have been reported to promote nuclear translocation of TFEB as Torin 1, which inhibits mTORC1 kinase activity upstream of TFEB [56, 62, 76]. In addition, TFEB subcellular localisation is influenced by changes in intracellular calcium levels. Indeed, calcium chelators (Bapta AM) block starvation-induced TFEB nuclear translocation, while calcium ionophores (Thapsigargin, Ionomycin and SF-51) promote TFEB nuclear translocation by promoting Ca^{2+} ions intake that activate the Calcineurin phosphatase upstream of TFEB [56, 76, 97].

1.2.4 The mTOR-mediated TFEB signalling pathway

The most well-studied mechanism for regulating TFEB's activity and subcellular localisation is the phosphorylation of particular serine residues in the TFEB protein

[8, 64, 76, 97]. In this context, TFEB activity is mainly controlled by the mammalian target of rapamycin (mTOR) [91]. This signalling pathway is described in Figure 1.4.

mTOR is central for regulation of the autophagic activity and senses the energy status by integrating signals from, for example, growth factors, amino-acids, and glucose [61]. mTOR exists as two structurally and functionally distinct complexes, mTORC1 and mTORC2. In particular, mTORC1 is an evolutionarily conserved kinase that regulates numerous

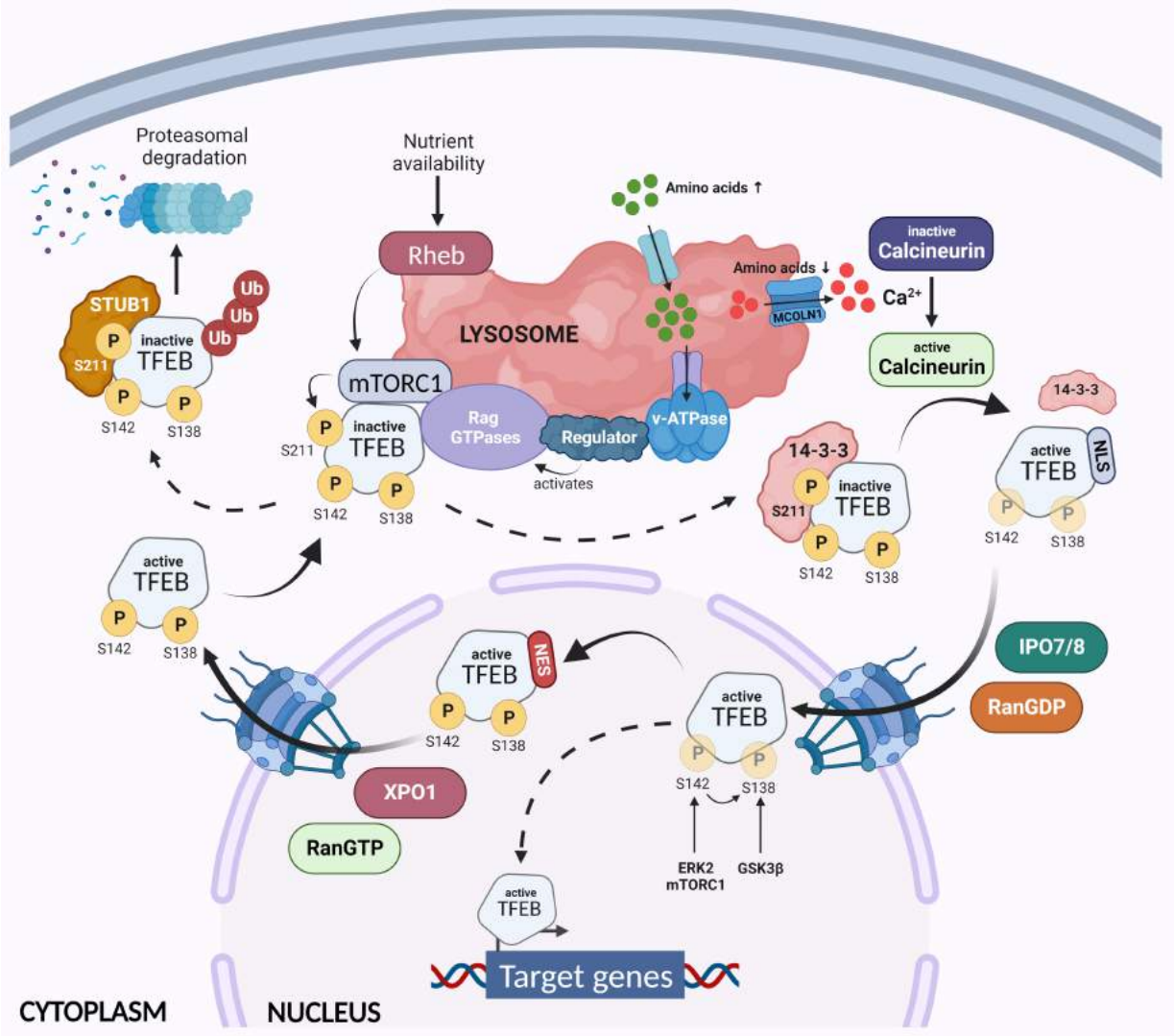

Figure 1.4: **TFEB nucleo-cytoplasmic shuttling in relation to the availability of amino acids.** Under normal growth condition, TFEB is inhibited inside the cytoplasm through a phosphorylation on S211 by mTORC1 complex. When inhibited, TFEB could either be targeted (ubiquitination) for proteasome degradation or bound by chaperone 14-3-3. During amino acids decrease mTORC1 is inhibited, contemporary TFEB is activated through a dephosphorylation by Calcineurin and translocates inside the nucleus promoting the activation of its target genes. Following refeeding, TFEB is hierarchically phosphorylated in the nucleus on S142 and S138 and exposes a nuclear export signal that causes its nuclear export via the exportin XPO1. Adapted from [26, 47, 97]].

cellular processes, including cell growth, proliferation, cell cycle and autophagy. mTORC1 localises to the lysosomal membrane and this distribution is crucial for its ability to sense and respond to variations of amino acid content in the lysosome.

mTORC1 is recruited to the lysosomal membrane in nutrient-rich contexts, specifically when amino stimulation is present. The lysosomal membrane allows amino acids to readily pass and accumulate inside the lysosomes. By means of the v-ATPase-Ragulator complex, these amino acids are "sensed" by the lysosomal lumen and communicate with the Rag GTPases [110]. At the lysosomal surface, GTP-bound Ras homolog enriched in the brain (Rheb) promotes the activation of mTORC1 [84, 85, 110]. Notably, TFEB is also recruited to the lysosomal surface by active Rag GTPases [54], where it is phosphorylated by the mTORC1 complex at a number of serine (S) residues.

Particularly, three residues have been discovered to be crucial for TFEB localisation despite the existence of at least 10 distinct phosphorylation sites [19]: S138, S142 and S211 [47]. Through the hierarchical phosphorylation of these serine residues, mostly by mTORC1, nutrient availability controls TFEB nucleo-cytoplasmic shuttling [62]. This process guarantees that only a TFEB phosphorylated on all three residues is entirely cytosolic and inactive, demonstrating that nutrient levels precisely regulate TFEB subcellular localisation through modification of its shuttling kinetics.

Specifically, TFEB cytoplasmic retention is brought on by mTORC1-mediated phosphorylation of TFEB at S211. In fact, S211 functions as a recognition site for TFEB binding to chaperon 14-3-3 and cytosolic retention, most likely by concealing its nuclear localisation signal (NLS) [52, 79, 91, 101].

When there is a deficiency of amino acids, mTORC1 detaches from the lysosomal membrane and turns inactive thus blocking the phosphorylation of TFEB. Interestingly, the nutritional restriction simultaneously causes the release of lysosomal Ca^{2+} through the calcium channel mucolipin 1 (MCOLN1). This activates the phosphatase Calcineurin, which then dephosphorylates TFEB [56]. Detachment from chaperon 14-3-3 and the conformational shift caused by TFEB dephosphorylation enable the NLS signal to be exposed, facilitating its nuclear translocation via importin IPO7 or IPO8 through the Nuclear Pore Complex (NPC) [72, 106]. Nuclear TFEB that has been dephosphorylated is

in an active state and can control the transcription of its target genes [76, 81, 97].

Following refeeding, TFEB nuclear export is promoted by hierarchical phosphorylation of S138 and S142 residues [47]. Due to their proximity to the TFEB nuclear export signal (NES), serine residues S142 and S138 are thought to have a role in TFEB nuclear export by controlling how the exportin chromosomal maintenance 1 (CRM1 aka XPO1), identified as a strong TFEB interactor [37], interacts with its hydrophobic export signal [47, 62].

The two primary protein kinases known to phosphorylate TFEB in most cell types under nutrient-rich contexts are mTORC1 and extracellular signal-regulated kinase 2 (ERK2, also known as MAPK1). Generally, S142 is a site for both ERK- and mTOR-mediated phosphorylation, whereas S138 has been proposed to be a GSK3β-phosphorylated site [47]. Neverthless, it has been demonstrated that phosphorylation on both S142 and S138 completely depends on mTOR activity [62], indicating that mTOR-mediated phosphorylation is the primary mechanism regulating TFEB subcellular localisation. In fact, the phosphorylation of TFEB is insensitive to Rheb activity brought on by growth factors and is solely dependent on the amino acid-mediated activation of Rags [20, 63].

Recently, chaperone-dependent E3 ubiquitin ligase known as STUB1 was discovered to control TFEB activity by selecting phosphorylated TFEB (S142 and S211) for ubiquitin-mediated proteasomal destruction. This implies that TFEB's phosphorylation state affects both its intracellular location and stability [92].

1.2.5 Other kinases and upstream regulators of TFEB

Other kinases were discovered that phosphorylate TFEB in addition to mTORC1 [8, 76, 97].

For example, mitochondrial stress has the ability to activate TFEB independently of mTOR. PINK1 and Parkin are required for the nuclear localisation of TFEB upon oligomycin or antimycin-induced mitophagy [65].

In osteoclasts, PKCβ phosphorylates a number of serine residues in the human TFEB C-terminus. Although TFEB subcellular location is unaffected, TFEB protein stability depends on these serines being phosphorylated by PKCβ [22].

As discussed in the previous Subsection, ERK2 was identified as responsible for S142

phosphorylation [47, 89], while GSK3β as responsible for S138 phosphorylation, besides of S134 [47, 48].

AKT phosphorylates TFEB at serine residue S467, according to a recent research, and treatment of cells with an AKT inhibitor promotes TFEB nuclear translocation [69].

TFEB nuclear translocation is promoted by the curcumin analogue C1 in a manner that is phosphorylation independent, according to a different recent study. In this instance, C1 binds to TFEB directly, interfering with TFEB's ability to connect to 14-3-3 proteins [93].

As a new central mechanism upstream of TFEB has been identified Foliculin, a well-known tumor suppressor gene for Birt-Hogg-Dubé (BHD) syndrome [10, 66]. Indeed, upon activation by amino acid-stimulation or growth factors, Foliculin activates Rags [85]. Secondly, it is necessary for mTORC1 to localise on the lysosomal membrane and for the Rheb protein to activate it so that it may phosphorylate and inactivate TFEB.

Chapter 2

Methods

Based on the principles of Systems Biology, I first conducted a set of experiments to characterize TFEB shuttling dynamics. Then, I carried out computational analyses in order to develop a model able to explain the experimental results. Here, I present the methods for experimental and computational analyses.

In particular, the experiments were conducted with two technological platforms based on a microfluidic device where the model cell line is loaded and that is connected with a time-lapse microscope for imaging and an input for treatments.

The platforms support long-term imaging, and once the experiment is finished, the data are subjected to image analysis to extrapolate the level of nuclear and cytoplasmic TFEB concentration over time.

A deterministic modeling-based computational analysis was carried out using the experimental findings as well as knowledge from the literature to yield a baseline.

2.1 Experimental Platform

Figure 2.1 provides a broad overview of the two experimental platforms utilized to conduct the experiments [25, 68, 75]. A time-lapse microscopy apparatus [74, 75], a specific microfluidic device, and an input system are the building blocks for the two platforms.

The microfluidic devices used for cell culture are designed to simulate physiological environments, allowing to investigate individual living cells in finely regulated microenvi-

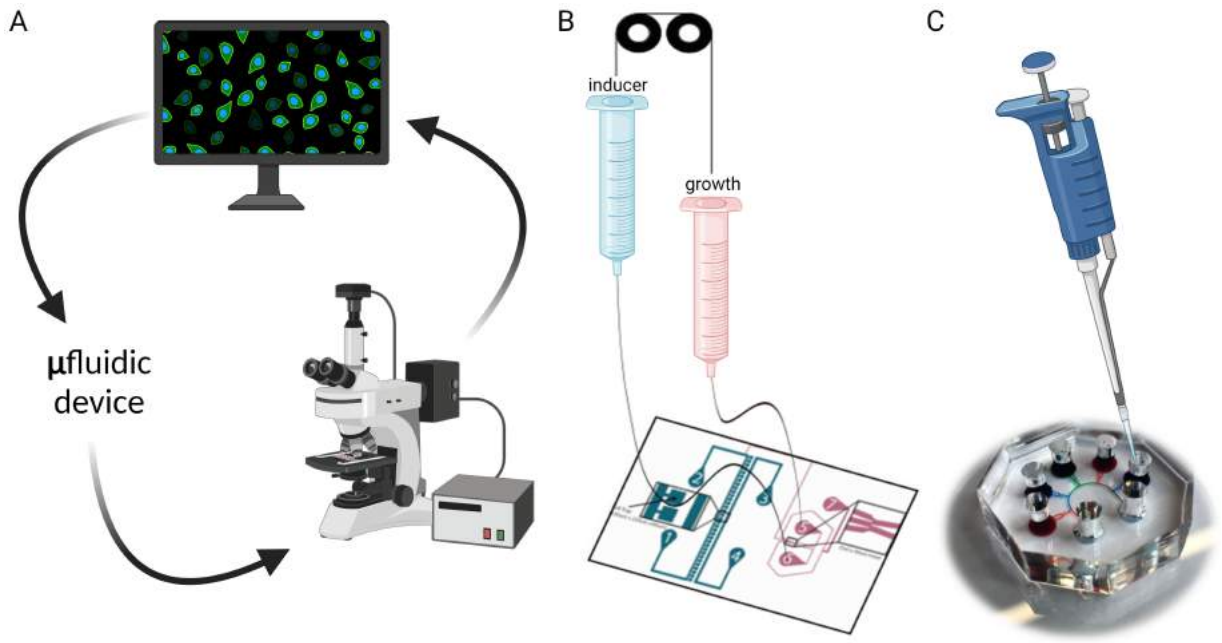

Figure 2.1: **Technological Platforms.** (A) The two platforms consist of a time-lapse microscopy apparatus, a specific microfluidic device, and an input system [74, 75]. (B) The first microfluidic device used is designed by Kolink and colleagues [41]. In order to dynamically administer various inputs to the cells that are loaded within, it is connected to a system of automated syringes that are controlled by a computer. (C) The second microfluidic device is called VersaLive and is designed by Nocera and colleagues [68]. In this instance, the treatment is given using a standard pipette to the cells that are loaded within.

ronments.

The micro-environment can be precisely controlled in both space and time thanks to microfluidics, which also optimizes reagent quantity, consumables, and time. Additionally, microfluidic devices enable for the constant refreshing or changing of cells' growth medium in order to prevent nutrient depletion from cell consumption and isolation of the cells from outside disturbances.

The ability to expose cells to a time-varying inducer signal is of particular significance since such dynamic stimulation most closely mimics the ever-changing natural environment in which cells normally reside [24, 41].

The development of these devices was initially hampered by the difficulties of mammalian microfluidic cell culture. Mammalian cells are very sensitive to minute changes in pH, osmolarity, shear stress, and other environmental conditions. A perfusion flow of media, which continuously replenishes the culture volume, is frequently employed to address issues with pH and osmolarity variation. To sequester cells in areas with strong resistance to fluid

flow and shield them from harmful shear effects, a variety of trapping geometries can be utilized.

Here, the experiments are carried out with two different microfluidic devices depending on their specific needs. The VersaLive platform described in Subsection 2.1.1 is used for multiple conditions experiments (Figure 2.1 C), whereas the platform described in Subsection 2.1.2 is preferred for dynamic input experiments (Figure 2.1 B).

Particularly, the conditions in the microfluidic device are changed manually for the VersaLive platform by using a pipette, while are changed automatically in the other device by using a set of automated syringes all controlled by a computer [25]. Cells are continuously imaged at a specific sampling time and the images are then processed to obtain the single cells fluorescence signals.

2.1.1 The VersaLive microfluidic device

VersaLive is a flexible and user-friendly microfluidic device for perfusion cell culture that can be used for a variety of applications using only standard pipettes [68]. It is utilized in mammalian cell lines and primary cells for a variety of applications, including time-lapse live cell imaging, immunostaining, cell recovery, cell lysis, and plasmid transfection. VersaLive may take the place of common cell culture formats in a range of applications, thus lowering costs and improving lab-to-lab replicability.

This PDMS microfluidic chip consists of five (or six) chambers that are each 250 microns wide (Figure 2.2 A). Each chamber has a connection to the main common channel on one side, and an individual input channel on the other. Through ports that serve as reservoirs with adjustable inputs, access to channels is ensured.

Active pumps are not required since hydrostatic pressure drives the flow from the ports to the chambers. Each culture chamber has a cell filter inserted on one side to keep cells inside the chamber by obstructing passage of objects wider than 5 microns.

There is a fluidic resistor between the culture chamber and the input to lower the flow velocity and, as a result, the shear stress on the cells. For a uniform and constant distribution, the flow deflectors assist in distributing the chemical input throughout the whole chamber area.

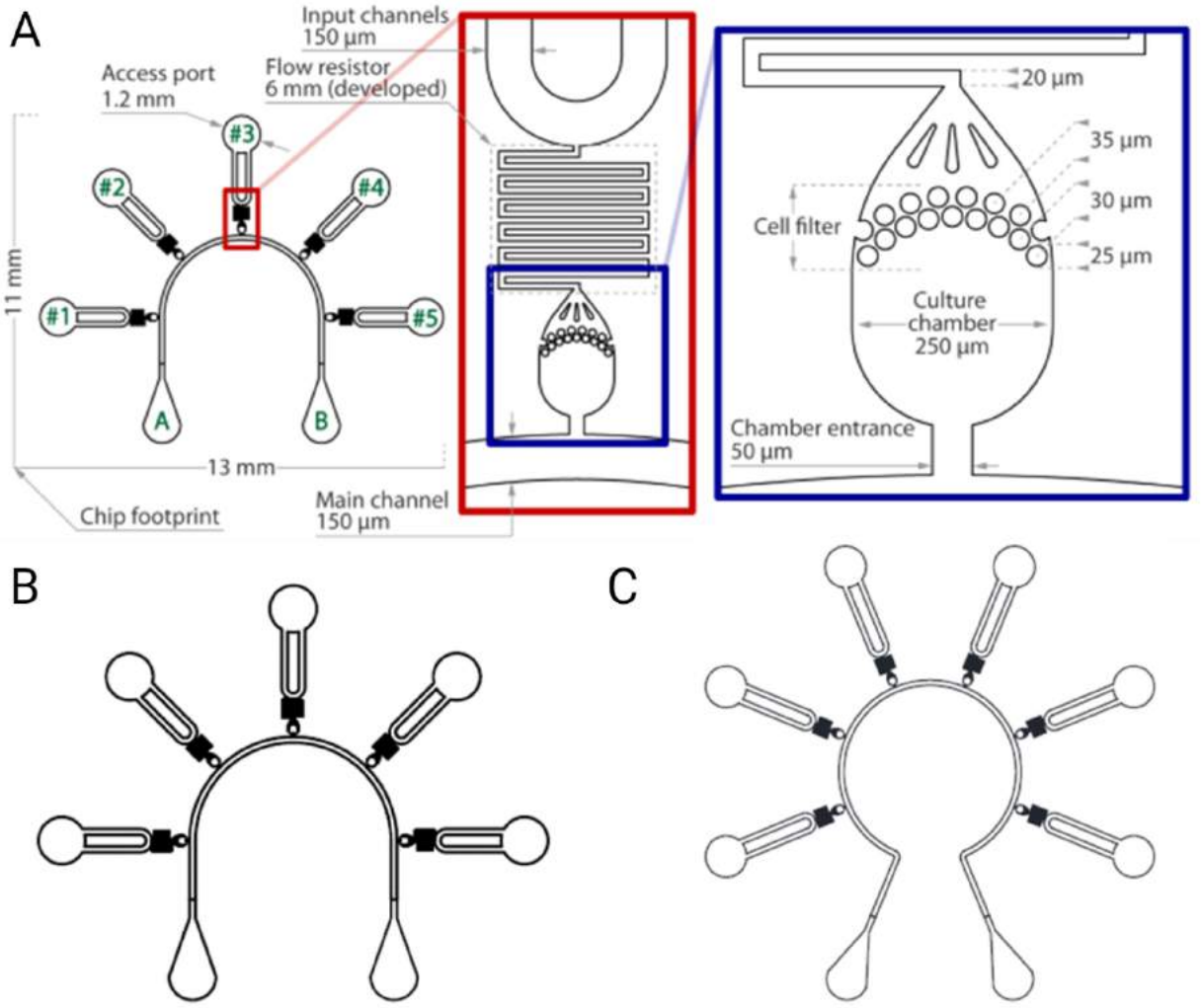

Figure 2.2: **Outline of the VersaLive microfluidic platform.** (A) The primary channel that runs from port A to port B connects all chambers. Each chamber has a separate connection (ports 1 to 5 on the schematics) that may independently supply fluids to each chamber. When using the device, shear stress to the cells is prevented by the serpentine, a flow resistor. Flow deflectors guarantee a uniform distribution of the fluid over the chamber's whole surface area. Objects bigger than 5 microns cannot pass through the cell filter. (B) VersaLive outline for five ports. (C) VersaLive outline for six ports. Adapted from [68].

The five ports version of the chip layout is shown in Figure 2.2 B, and the six ports version used in the experiments conducted in this study is shown in Figure 2.2 C.

VersaLive can run in two distinct ways: in single-input mode (Figure 2.3 A), where the same input is supplied to every cell chamber, or in multi-input mode, where a separate input can be delivered to each of the five or six chambers.

In this scenario, the input reservoirs are left empty while all chamber reservoirs are filled (Figure 2.3 B). With this set up, each chamber has an active flow that is sufficient to both reduce shear stress on the cells and prevent backflow into the main channel.

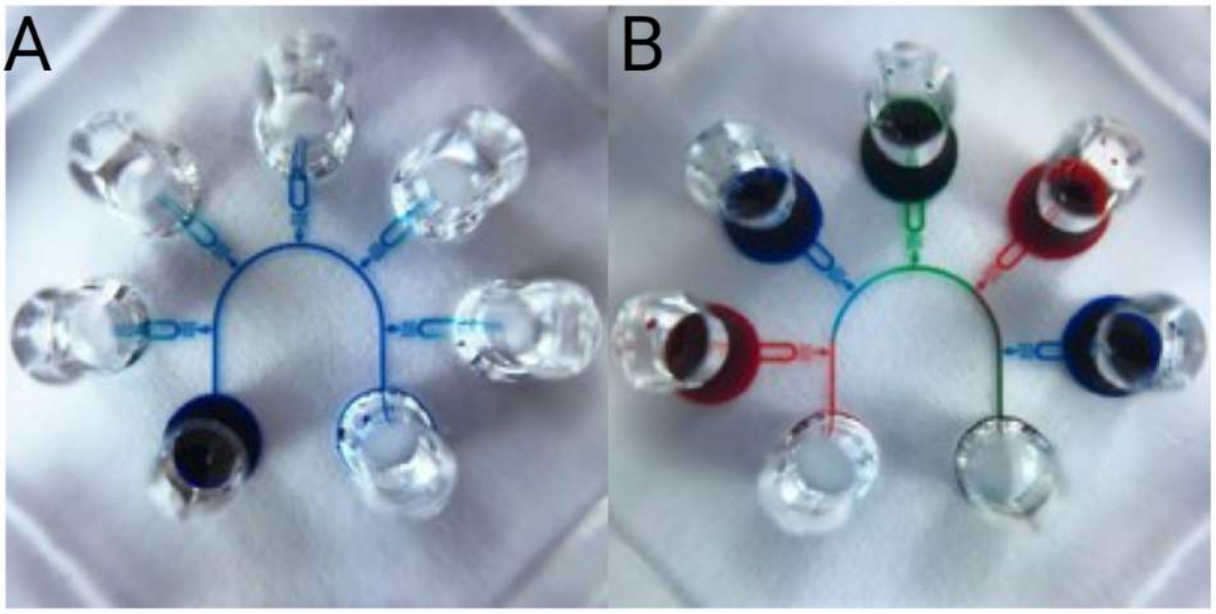

Figure 2.3: **VersaLive modes of operation.** (A) The main channel is utilized to simultaneously provide the same medium to all chambers in the "perfusion" Single-Input Mode. (B) The Multi-Input Mode prevents cross contamination by delivering a distinct medium to the cell chamber through each dedicated input reservoir. Adapted from [68].

Further details about the protocols for microchips fabrication and cells loading are discussed in the Appendix B.

2.1.2 Microfluidic Device for Dynamic Stimulation

The microfluidic device created by Kolink and colleagues [41] for automated dynamic stimulation is a PDMS chip where fluid dynamics at the microliter scale are exploited. It consists of thirty-three individual cuboid culture chambers (each has a 230 by 230 microns footprint, 40 microns height) adjoined to a main perfusion channel of identical height via a 50 microns wide opening on one side of each chamber (Figure 2.4 A). A separate channel for application of a temporary vacuum runs parallel to the column of culture chambers at a distance of 160 microns between the wall of this channel and the closest wall of each cuboid chamber (Figure 2.4 A). It allows to rapidly load a high density of cells into individual trapping regions that are extremely isolated from the shear stress effects of the main perfusion channel. Once captured in the traps, the cells remain undisturbed even at high flow rates.

A fluidic mixer network named the Dial-a-Wave (DAW) is used to deliver any desired

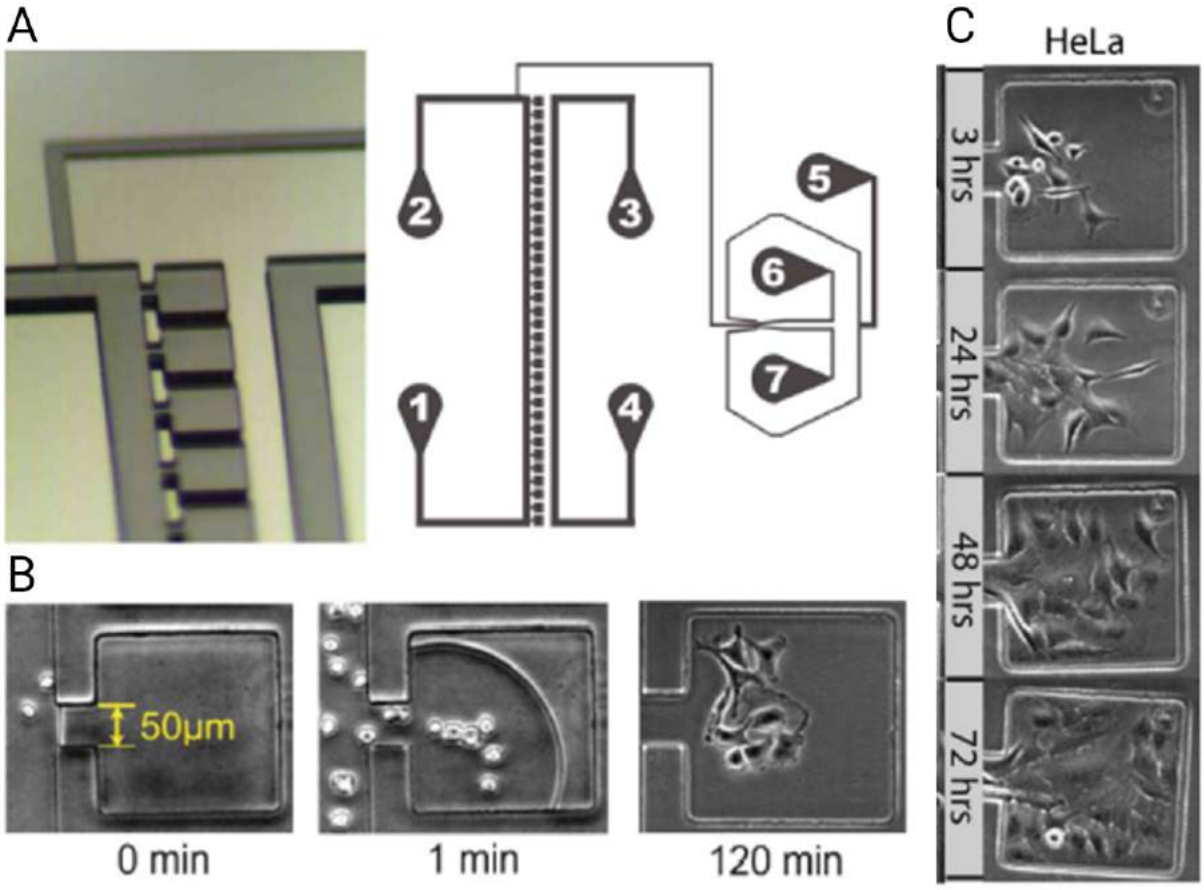

Figure 2.4: **Device design and vacuum-assisted cell.** (A) Each of the thirty-three cuboid culture chambers is connected via a narrow opening to a main perfusion channel that runs between ports 1 and 2. A separate air channel between ports 3 and 4 allows the application of a temporary vacuum at the PDMS interface to draw fluid from the main perfusion channel into the culture chambers. Ports 5–7 are connected to the DAW dynamic stimulation generator. (B) Upon application of a vacuum in the air channel at time zero, fluid containing cells is rapidly drawn into the culture chambers and fills the traps. HeLa cells attach and begin to spread out within 1–2 h after loading during continuous perfusion culture. (C) After initial vacuum loading into the culture chambers, HeLa cells rapidly colonize the glass growth area of the device during continuous media perfusion. Adapted from [41].

waveform of biochemical inducer for dynamic stimulation of cells inside the culture chambers [23, 41].

The working principle of the DAW mixer is to precisely combine two incoming fluid streams (inducer and control media) in any desired ratio by adjusting the hydrostatic pressure of the corresponding inputs (ports 6 and 7) in a manner that increases the pressure at one input while decreasing the pressure at the other input by exactly the same amount (Figures 2.5 B and C). Thus, the ratio of the inputs from port 6 and 7 leaving the junction to the cell chamber is determined by modulating the difference in hydrostatic pressures at

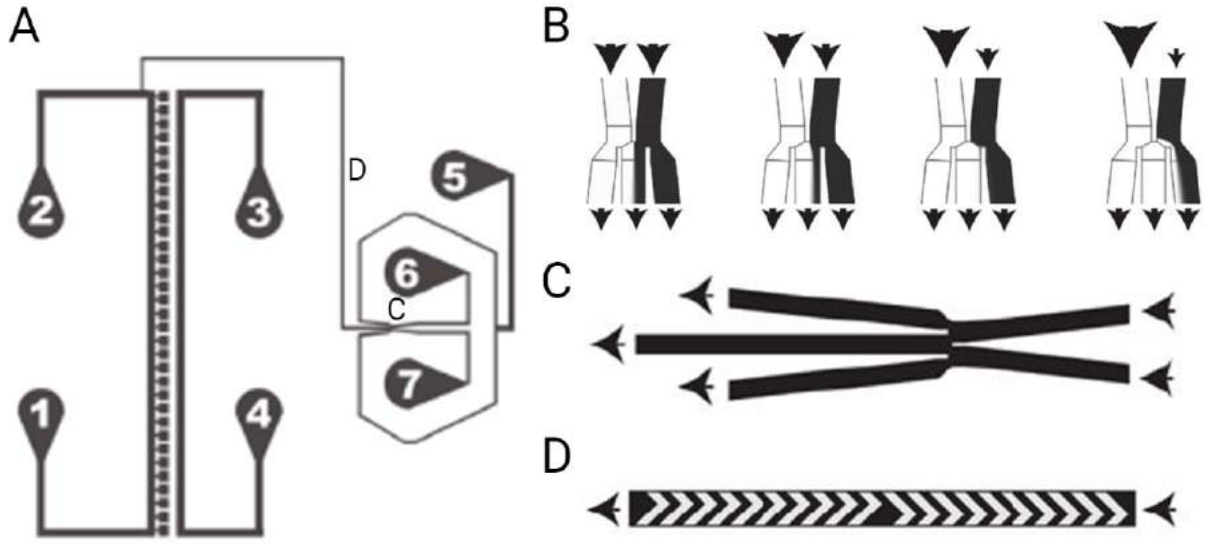

Figure 2.5: **DAW junction and staggered herringbone mixers.** (A) Outline of the microfluidic device for dynamic input experiments geometry. (B, C) The flow from the inlets (6 and 7) converges in a ratio dependent on the inlet pressures of each trough the DAW junction. (D) The SHM immediately follows the DAW junction. It enhances diffusive mixing of the combined laminar flow streams before the fluid reaches the main perfusion channel and the adjoining culture chambers. Adapted from [23, 41].

the two inlets. Excess fluid is diverted through a shunt network to port 5, which is a waste port [24].

The DAW output signal is directed to the cells via a channel which contains staggered herringbone mixers (SHM) to enhance diffusive mixing of the combined laminar flow streams before the fluid reaches the main perfusion channel and the adjoining culture chambers (Figure 2.5 D) [96]. In this way, the fluid leaving the central fork of the junction for the cell chamber is mixed into a uniform concentration by the SHM.

Further details about the protocols for microchips fabrication and cells loading are discussed in the Appendix B.

2.1.3 Actuation System

As previously mentioned, the platform described in Section 2.1.2 is chosen for dynamic input experiments because it automatically changes conditions by means of a set of automated syringes that are all operating under the control of a computer [25]. Here is a description of the actuation system for the automated syringes.

In order to modulate the concentration of compounds within a cell trap, in the microflu-

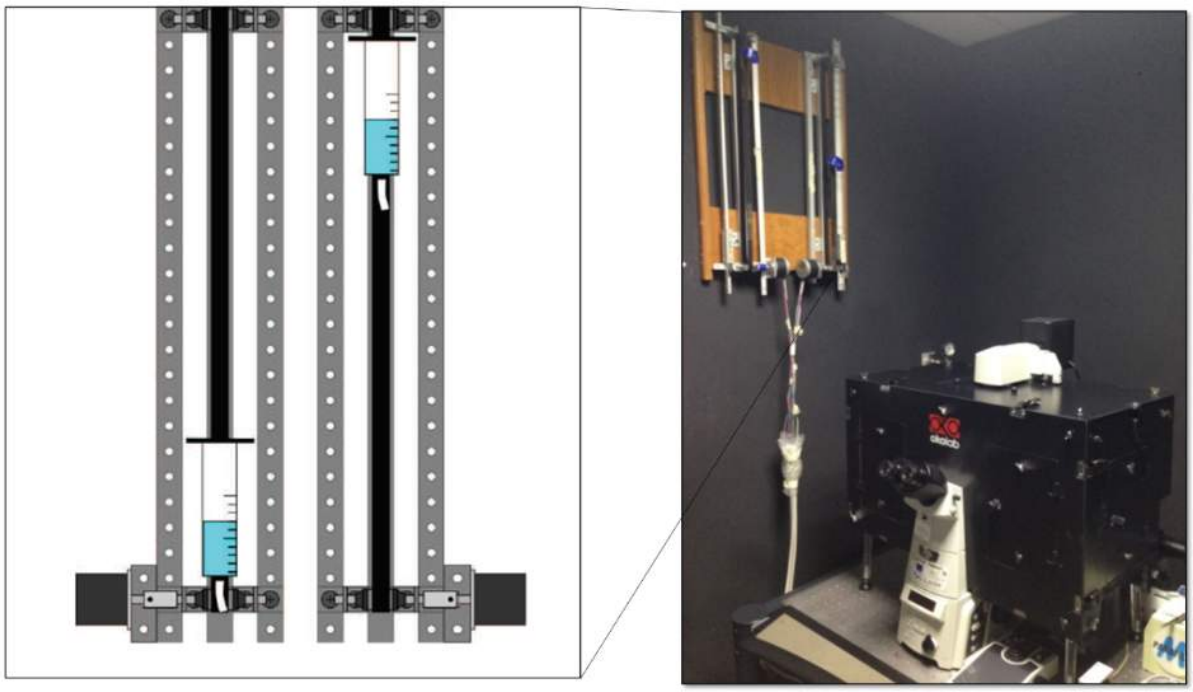

Figure 2.6: **Linear actuators.** The two designed linear rails are presented in this 2D model. The external frame sustains the holder for the stepper motor and the two pulleys on which the timing belt is meant to slide. The sliding element is mechanically secured to the belt in order to allow coherent movements [24, 59].

idic device, a pressure source is needed. For this reason, the DAW junction was designed. The DAW junction (Figure 2.5 B) works by changing the relative pressures at DAW ports, while keeping the total pressure the same; thus the input ratio to cells is the result of the pressure difference at ports 6 and 7. The actuation aim is to establish this difference in order to appropriately modulate the inputs concentration in the fluid reaching the cell trap [24, 59].

Physically, this can be achieved by changing the relative height of the syringes connected to the two inlet ports. Indeed, each syringe will exert a hydrostatic force over the fluids in the channel that is simply proportional to its height. Hence, when the two syringes are set at different heights, a differential pressure will be generated at the level of the junction.

To accomplish this task, two vertically mounted linear actuators were designed (Figure 2.6) [24, 59]) to be controlled by a computer algorithm to allow fast and precise operations. In particular, the actuation system is formed by two linear guides; each one of these is designed to move independently from the other; the motion is realized through two stepper motors, while the transmission by using a timing belt and two pulleys. The transmission gear

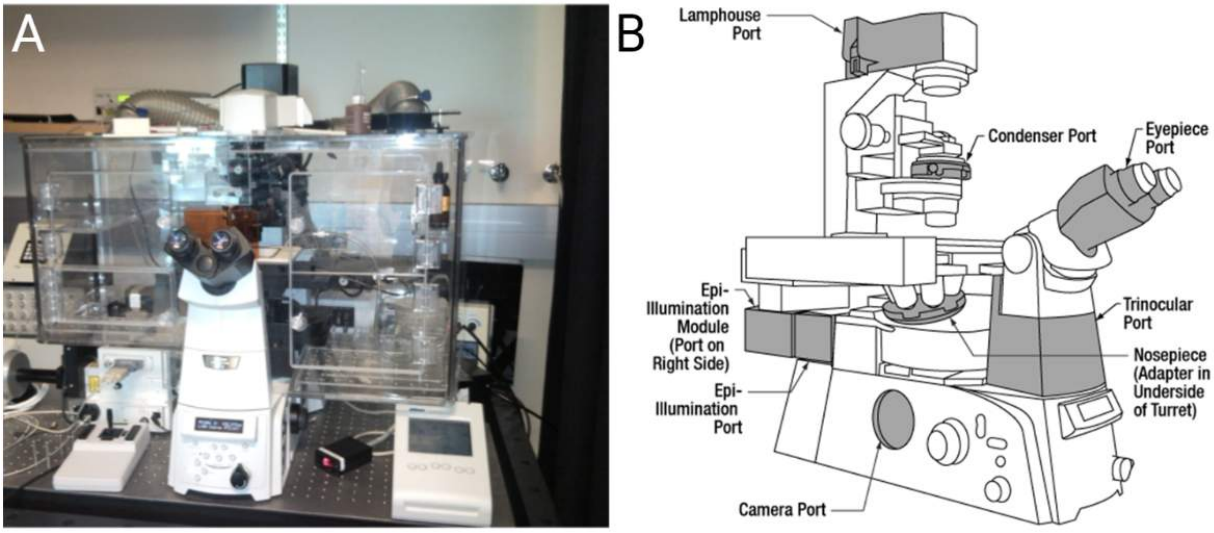

Figure 2.7: **Nikon Eclipse TI fuorescence microscope.** (A) The inverted fluorescence microscope (Nikon Eclipse TI) used in this study was equipped with a EMCCD high sensitivity camera and an incubator to control gasses and temperature of cell environment. (B) In this configuration the objectives are assembled on a motorised nosepiece. The optical train conveys light to either eyepieces of a CCD camera that digitises the image and sends it to the computer controlling the acquisition. Adapted from [24, 59].

adopted is an ideal solution, with no need of high torques, to guarantee good performance in terms of actuation speed.

The simplest and least expensive way to achieve this result is by using a stepper motor. This motor is controlled by using a proper excitation sequence of the stator circuit (using particular electronic drivers), and because each rotor position corresponds to a step (specific excitation status of the stator circuit), it is known as a stepper motor.

2.1.4 Time-Lapse Microscopy

The platforms described above, employs an inverted fluorescence Nikon-TI Eclipse microscope (Figure 2.7) [24, 59]. The microscope is equipped with an automated and programmable stage, an incubator to guarantee fixed temperature and gasses to cell environment and a high sensitivity Electron Multiplying CCD (EMCCD) Camera (Andor iXON Ultra897). The microscope and the camera can be programmed to acquire, at regular time intervals, images from a fixed area of the cell trap as well as from different points of the microfluidic device. In this configuration, images are taken by objectives that are mounted on the base of the microscope instead of on the tower.

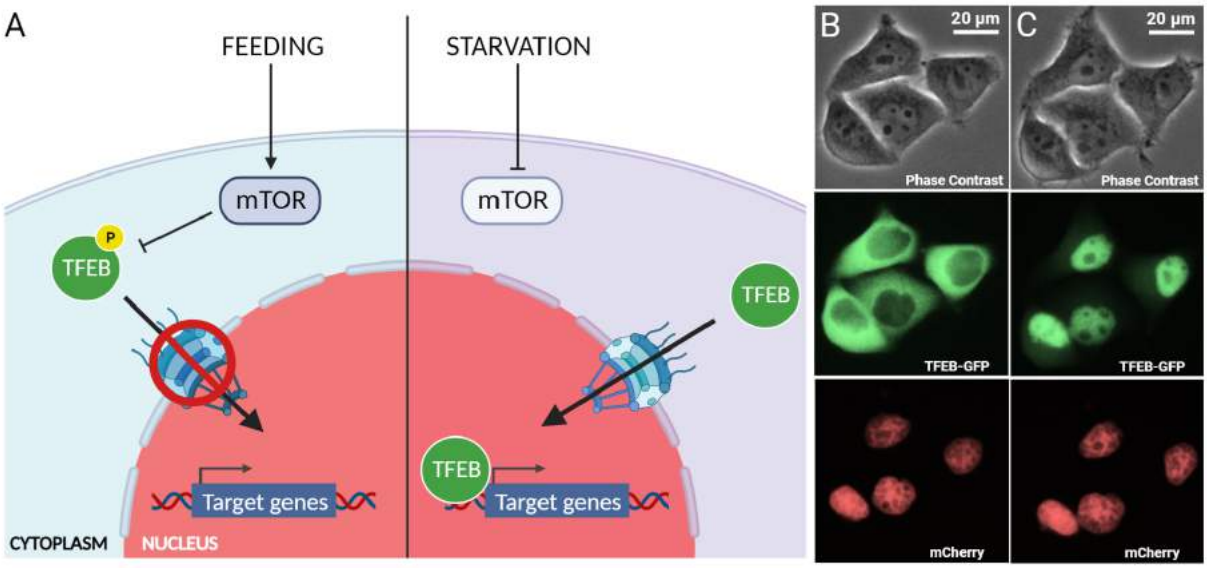

Figure 2.8: **Model of TFEB-GFP translocation.** (A) Scheme of the translocation process in the HeLa TFEB-GFP monoclonal cell line. In fed conditions, the fusion protein TFEB-GFP is phosphorylated by mTOR and trapped in the cytoplasm. In starvation condition, mTOR is inhibited, TFEB-GFP is no longer phosphorylated, and it is able to translocate into the nucleus. HeLa monoclonal cell line images taken in phase contrast and fluorescence (TFEB-GFP and nuclear mCherry) under growth (B) and starvation (C) conditions. Here, TFEB-GFP is cytoplasmic during growth (B), and nuclear during starvation (C).

2.2 Experimental Analysis Methods

2.2.1 Microfluidic Experiments

The studies were conducted with a human HeLa cell line overexpressing the fusion protein TFEB-GFP in order to explore the dynamics of TFEB nuclear shuttling. Additionally, a nuclear mCherry protein is expressed by this cell line to facilitate image processing [75] (Figure 2.8).

When cells are in nutrient-rich conditions, TFEB-GFP is phosphorylated by mTORC1 and subsequently sequestered in the cytoplasm, as shown in Figures 2.8 A and B. In the absence of amino acids (starvation), mTORC1 is inhibited thus TFEB-GFP is no longer phosphorylated and translocates to the nucleus, as shown in Figures 2.8 A and C.

Using the technological platforms mentioned in Section 2.3, I performed a set of experiments. Specifically, the cells were loaded in one of the microfluidic devices (described in Subsections 2.1.1 and 2.1.2) and allowed to grow up over night in a cell culture incubator (for more details see Appendix B). Then, the device was put under the time-lapse microscope

and the images acquisition and the experiment were started.

The microscope is programmed to acquire two types of images: phase contrast images and fluorescence images (one for the green spectrum for GFP and one for the red spectrum for the nuclear mCherry). As shown in the following Subsection, image analysis techniques can be used after cells have been imaged to estimate their fluorescence. Fluorescence microscopy and image processing allowed for the quantitative assessment of TFEB nuclear and cytoplasmic localisation in individual cells.

2.2.2 Image Analysis

The fluorescence and phase-contrast images acquired by the microscopy apparatus need to be processed in order to obtain the percentage level of nuclear TFEB. I utilized the algorithm described in [64] to accomplish this task.

The algorithm uses a machine-learning approach (FastER) together with a MATLAB script to selectively segment, track, and measure the HeLa TFEB-GFP monoclonal cell line (Figure 2.9).

FastER, a machine-learning method [30], processes the raw phase-contrast pictures acquired during the image acquisition phase and generates a binary mask of the cells that is entered into the MATLAB script, which also processes the green and red fluorescence images.

The MATLAB script uses the nuclear fluorescent protein H2b-mCherry to locate the cells' nuclei in the red spectrum images and eliminates the background pixels from fluorescence images.

To prevent contacting nuclei from being mislabelled, these images are then binarized and further modifications are made. To create a mask for monitoring the cytosolic fluorescence, the acquired nuclei mask and whole cell FastER mask are logically combined as shown in Figure 2.9. The pixel intensity is used to estimate the green fluorescence of the entire cell as well as of the various compartments (cytoplasm and nucleus).

Finally, a customized offline cell tracking algorithm is used to monitor single-cell traces. This algorithm minimizes a cost function to find the correlation between the nucleus centroids in two subsequent red fluorescence images. Lastly, a visual inspection of the

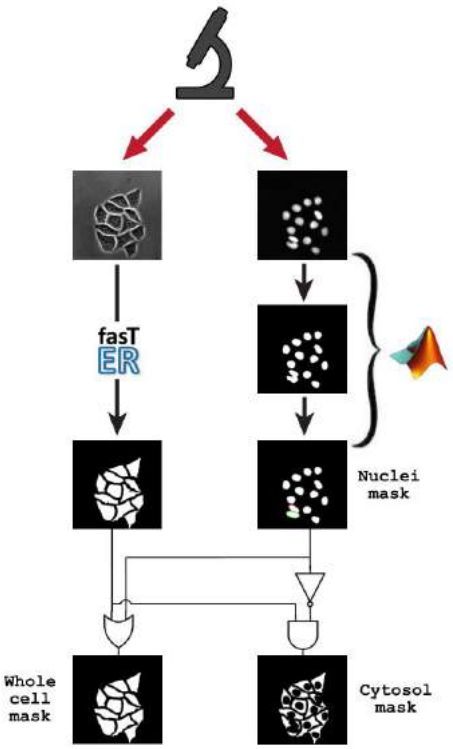

Figure 2.9: **Segmentation pipeline.** Upon processing the acquired images, a total cell mask, a nuclei mask, and a cytosol mask are obtained. Using a machine-learning based algorithm (FastER), the raw phase-contrast images are processed [30]. Red spectrum images are processed using a custom MATLAB program. The final masks are created by applying logic operations. From [64].

fluorescence signal is done by the human operator to exclude non-fluorescent cells and cut the signals during cell division and death as these processes might impair the performance of the tracking module. Further details are provided in [64]. The nuclei fluorescence was normalized with respect to the cells fluorescence and the percentage of nuclear TFEB was then measured.

2.3 Computational Methods

2.3.1 Dynamical Modelling

Once the experiments were completed, I designed and optimised a mathematical model in order to account for the experimental results and comprehend the dynamics of TFEB translocation. I took advantage of the literature described in Chapter 1 to construct the model's overall framework.

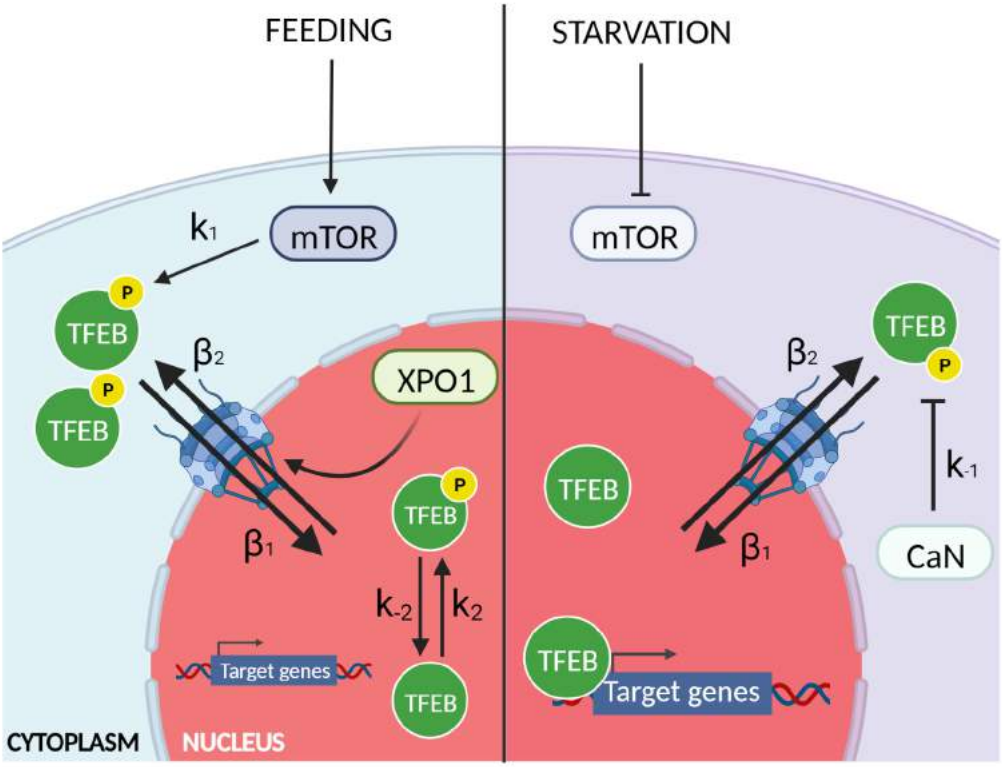

Figure 2.10: **Simplified scheme of TFEB-GFP translocation in the HeLa monoclonal reporter cell line.** Under fed conditions, mTOR phosphorylates the fusion protein TFEB-GFP at a rate k_1 and traps it in the cytoplasm. At the same time, nuclear TFEB-GFP is phosphorylated at rate k_2 and is exported by XPO1 at a rate β_2. In starvation condition mTOR is inhibited, TFEB-GFP is dephosphorylated by Calcinceurin at a rate k_{-1}, and it is able to translocate into the nucleus at rate β_1. Adapted from [81].

A simplified scheme of the translocation process under investigation is reported in Figure 2.10, which summarizes the known TFEB regulatory mechanisms that were previously described in details in Figure 1.4. Figure 2.10 also takes into account that the biological model being studied is the monoclonal Hela reporter cell line, which stably expresses mCherry in the nucleus and overexpresses the fusion protein TFEB-GFP [81].

Figure 2.10 is a simplified scheme that highlights the reaction rates of interest and the critical phases of TFEB shuttling between the two compartments, nucleus and cytoplasm.

In order to maintain generality and reliability, stochastic dynamic modeling is typically adopted since cellular processes depend on unpredictable biological events. The experiments I performed revealed that TFEB translocation dynamics are highly preserved in each single cell signal, and every cell exhibits the same behavior, indicating that the phenomenon under study transcends beyond the context's inherent stochasticity. More details about the

experimental results will be discussed in Chapter 3.

Hence, I operated in a deterministic environment despite the fact that the general approach is single-cell based. Consequently, all the proposed models in Chapter 4 are based on ordinary differential equations (ODEs) and have the general form $\dot{x} = f(x, u)$, where $x \in \mathbb{R}^n$ is the state vector and $u \in \mathbb{R}^m$ is the input vector. Models and simulations were developed, analyzed and simulated in *Mathworks Matlab R2019a*.

Chapter 3

Experimental Investigation of TFEB nuclear shuttling dynamics

As previously mentioned, the literature shows how TFEB activity is significantly influenced by its cellular localisation and its shuttling activity in response to nutrients availability. In this Chapter, I describe a cutting-edge method to track translocation dynamics with the aim of analyzing the transcription factor behavior at the single cell level. I specifically performed a series of experiments in real time that tracked the nuclear localisation of TFEB in separate cells growing in a microfluidics device.

In preliminary tests, stimulation alternated between nutrient-rich and starvation media. The results of the experiments revealed complex dynamics exhibiting an "overshoot" in which, in response to starvation, TFEB translocated to the nucleus but subsequently partially relocalised to the cytoplasm. These findings revealed the existence of a novel adaptation mechanism never described before and raised curiosity regarding its origin.

Consequently, I conducted novel tests in order to identify the key players in this behavior. Specifically, I repeated the previous experiments where blocking specific pathways related to TFEB shuttling by using small molecules.

Through the identification of their function and involvement, this investigation enabled a full characterisation of this novel mechanism. Not less significant, the findings presented here serve as the basis for the quantitative modelling as described in the next Chapter.

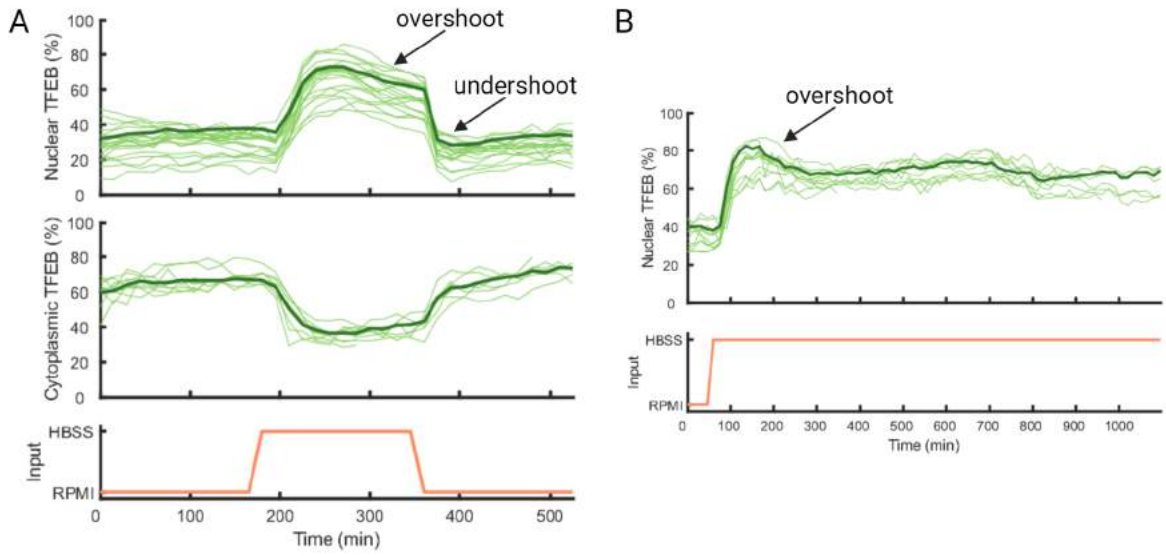

Figure 3.1: **Preliminary experimental measurements of TFEB translocation in the nucleus.** TFEB translocation following a pulse (A) and step (B) of starvation medium (HBSS). The figures in the top panel of (A) and in (B) show the single-cell traces of nuclear TFEB fluorescence.The figure in the bottom panel of (A) shows the single-cell traces of cytoplasmic TFEB fluorescence. The average of the single-cell traces is highlighted with a solid line.

3.1 Microfluidics experiments to observe TFEB dynamics

The preliminary experiments that I performed were aimed at analyzing the translocation dynamics of TFEB following starvation and growth stimuli. In particular, the starvation condition was induced using HBSS, a saline solution, or RPMI deprived of amino acids to promote cytoplasm to nucleus translocation. Feeding condition was induced using complete RPMI to promote nucleus to cytoplasm translocation. The details are discussed in Appendix B.

3.1.1 TFEB translocation dynamics following starvation

The first two experiments were realized alternating starvation and growth media following a pulse (Figure 3.1 A) or a step input (Figure 3.1 B), respectively [80, 81]. The input was dynamically changed by modifying the relative heights of two syringes connected to the microfluidics device, as previously described [25].

In the pulse experiment (Figure 3.1 A), cells were treated for three hours with complete

RPMI, followed by three hours with HBSS, and then again three hours with complete RPMI. At fifteen minutes intervals, cells were imaged in the microfluidics device for a total of nine hours.

In the step response experiment (Figure 3.1 B), cells were supplied with growth medium (complete RPMI) for one hour and then the starvation medium (HBSS) was provided to the cells for nineteen hours. Cells were imaged for a total of twenty hours in the microfluidics device at fifteen minutes intervals.

Figures 3.1 A top panel and B show the TFEB nuclear level as a percentage of the whole cell fluorescence, whereas Figure 3.1 A bottom panel shows the TFEB cytoplasmic percentage. The single-cell signals are depicted with thin green lines and their average with a bold green line. The two experiments exhibit similar features. With particular attention to the experiment shown in Figure 3.1 A, TFEB is mostly cytoplasmic at the start of the experiment when the growth medium is supplied, with around 30 percent of it being nuclear. Then, after changing from a nutrient-rich medium to a starvation medium, TFEB accumulates in the nucleus and reaches a high of around 80 percent in about thirty minutes. Then, during the starving phase, TFEB nuclear level gradually drops with a distinct overshoot, leading to a cytoplasmic relocalisation. When refeeding cells, TFEB nuclear level quickly drops but then slightly increases, generating a dynamics that I named "undershoot".

The same translocation dynamics were observed in the step response starvation experiment (Figure 3.1 B).

The observed overshoot dynamics are an example of adaptation, which is a unique regulatory mechanism that develops as a physical system reacts to environmental changes [100].

In order to determine whether the observed adaptation phenomenon depends on the stimulus duration, I then carried out two more tests by changing the input (Figure 3.2).

I performed a first experiment by treating cells with a starvation double pulses train (Figure 3.2 A). Here, the cells received complete RPMI treatment for one hour before the starving double pulses train, which consists of a variable-duration first pulse (one, two, or three hours), fifteen minutes of complete RPMI treatment, and a three hours HBSS pulse,

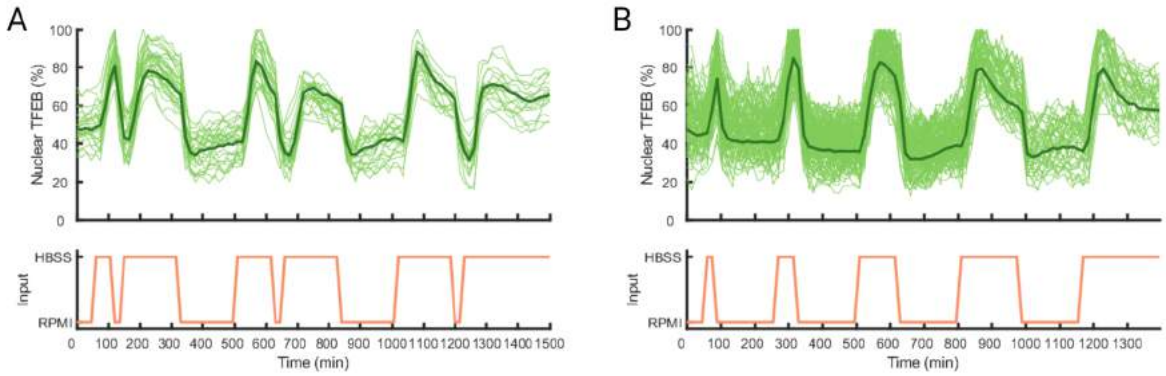

Figure 3.2: **Experimental measurements of TFEB translocation in the nucleus following pulses of different geometry.** TFEB translocation following starvation (HBSS) double pulses train (A) and starvation pulse train of different temporal duration (B). The figures show the single-cell traces of nuclear TFEB fluorescence. The average of the single-cell traces is highlighted with a solid line.

followed by three hours of complete RPMI treatment. Cells were imaged for a total of twenty-five hours in the microfluidics device at fifteen minutes sampling interval.

In a second experiment, cells were subjected to a train of starvation pulses with varying temporal durations (Figure 3.2 B). In this instance, cells were treated with complete RPMI for one hour prior to the starvation pulse train, which alternated complete RPMI pulses lasting three hours with HBSS pulses of varying duration (half, one, two, and three hours). Both results show that TFEB shuttles between the nucleus and cytoplasm in a manner that exhibits an overshoot dynamic as media are changed. The translocation dynamics, in particular, remain the same regardless of the duration of the stimulus demonstrating that the adaptation mechanism is a feature of the biological system under study.

In summary, a prolonged starvation treatment of at least three hours highlighted the presence of a novel TFEB translocation dynamic: the transcription factor reaches equilibrium with an overshoot dynamic that reveals a previously unreported adaptive mechanism. A similar phenomenon was recently observed in [108]. The authors suggested that the rapid rheostatic response, mediated by mTOR, allows the cell to quickly adapt to metabolic changes, while the long-term, mTOR-independent homeostatic response controls the magnitude and duration of TFEB activation, and presumably limits excessive autophagy. However, no mechanism was put forward to explain the origin of this dynamic behaviour.

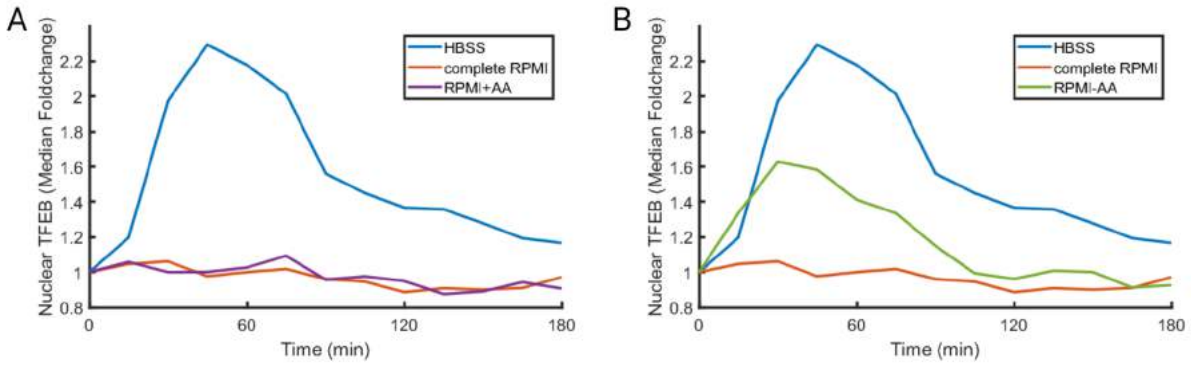

Figure 3.3: **Experimental measurements of TFEB translocation in the nucleus following amino acids (AA) starvation.** TFEB translocation following a pulse of growth medium supplemented (A) and depleted (B) with amino acids. The two treatments are both compared with the two controls: i) pulse of complete growth medium (complete RPMI), ii) pulse of starvation medium (HBSS). The figures show the median foldchange of the single-cell traces of nuclear TFEB fluorescence.

3.1.2 TFEB translocation dynamics following Amino Acids starvation

Since HBSS is a saline solution devoid of any nutrients, cells in HBSS medium undergo full starvation. However, it has been documented in the literature that amino acids (AA) are important for TFEB localisation. Indeed, it has been observed that TFEB translocates to the nucleus under amino acids deprivation [31, 62, 91]. As a result, I was also curious to know how amino acids affected overshoot dynamics and adaptability mechanisms.

Consequently, I decided to perform some tests in VersaLive [68]. Here, I used the platform in multi input mode, testing different amino acids concentrations. In each test, cells were treated with complete growth medium overnight, then the treatment was supplied and cells were imaged for three hours. More information is available in Appendix B.

In a preliminary experiment, I treated cells with RPMI that was either completely deprived of amino acids (Figure 3.3 B) or completely supplemented with amino acids (Figure 3.3 A), using HBSS and complete RPMI as controls. The median foldchange of the data, where cells were normalized with respect to the initial time point, is shown in Figure 3.3.

While cells treated with amino acid deprivation exhibit the overshoot dynamic, cells treated with supplemented RPMI behave similarly to those treated with complete RPMI. Additionally, the overshoot peak is far smaller than the one attained by the HBSS treatment,

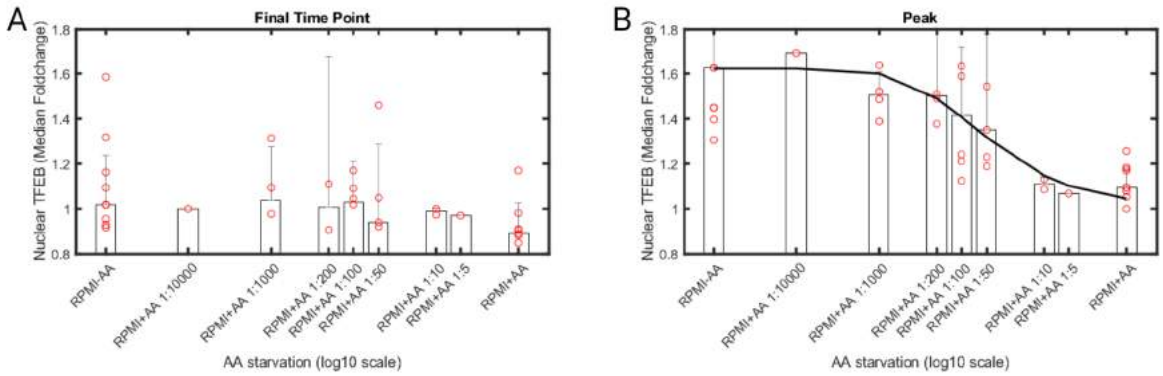

Figure 3.4: **Bar Graphs of TFEB translocation in the nucleus following the amino acid (AA) starvation dose test.** Bar Graphs of TFEB translocation at the end of each treatment (A) and at the maximum of the overshoot peak following each treatment (B). The black line represents the sigmoidal curve used to fit the nonlinear trend upon amino acids starvation dose test. The figures show the median foldchange of the single-cell traces of nuclear TFEB fluorescence. The amino acids starvation conditions are reported on a log10 scale. Each bar represents the median of the replicates for each condition and is reported with their standard deviation. In addition, the values of the replicates for each condition are reported as red circles on each bar.

and when compared to HBSS starvation, the response of cells to amino acid starvation was more heterogeneous (data not showed).

These findings show that amino acids starvation is sufficient to activate the adaptation process. It is noteworthy that less TFEB translocates into the nucleus following amino acid deprivation than it does under total starvation. This implies a lower overshoot peak. This observation suggests that, as a result of the rising TFEB nuclear concentration, the overshoot dynamic is dependent on the level of starvation.

To investigate this latter aspect, I supplemented incomplete RPMI with various dosages of amino acids (from 1:5 to 1:10000). I treated cells for three hours in a total of six dilution tests, taking images every fifteen minutes. Then, for each condition, I calculated the median foldchange and gathered the maximum peak value (Figure 3.4 B) and the value at the end of three hours (Figure 3.4 A) in bar charts. After three hours of treatment, it is clear from the bar charts of the final time point (Figure 3.4 A) that the signal is nearly constant, indicating the same level of TFEB in the nucleus for each condition.

Instead, by examining the bar chart of the peak (Figure 3.4 B), it is possible to appreciate a nonlinear sigmoidal trend of the overshoot peak. There is a linear trend between 1:10 and 1:200 amino acid doses, followed by a saturation for higher or lower starvation values,

showing that the maximum of the overshoot depends on the levels of amino acid starvation.

I fitted the median of the peak of each condition with a sigmoidal function to verify that the trend was indeed sigmoidal. The sigmoidal function used is here reported:

$$S(x) = 1 + \frac{\alpha k_{50}^h}{k_{50}^h + x^h}$$

where: x refers to the amino acids starvation levels (in log10 scale) and α, k_{50} and h are the function's parameters. I fitted the function's parameters by using the Matlab function "*nlinfit*". The parameters resulted from the fitting were: $\alpha = 0.625$, $k_{50} = 3.32$ and $h = 6.30$. According to this equation, the k_{50} of the sigmoidal function corresponds to the "1:50" amino acid dilution.

In conclusion, the experimental analysis and computational fitting both support the finding that the treatments at various levels of amino acid starvation showed a sigmoidal trend of the peak of TFEB overshoot dynamic, indicating that the overshoot is proportional to starvation.

3.2 Microfluidics experiments following small molecule inhibition of biological processes

The discovery of a novel adaptation mechanism was as surprising as unexpected. This finding opened the door to several questions regarding its origin and its role. In this context, to comprehend this mechanism better, I decided to conduct new experiments to examine the function of each reaction that takes place along TFEB shuttling. Indeed, there are several participants in TFEB translocation, as discussed in Chapter 1.

Consequently, I decided to repeat the experiments by inhibiting the key pathways involved in TFEB translocation in order to observe how TFEB shuttling dynamics change. More specifically, by using small molecules, I primarily focused the analysis on the inhibition of: TFEB phosphorylation via mTOR, autophagy, TFEB export via XPO1, TFEB degradation via the proteasome, translation and transcription. In the Subsections that follow, I will show how blocking each of these routes separately affected the dynamics of TFEB shuttling and then the results will be discussed. Refer to Appendix B for details on

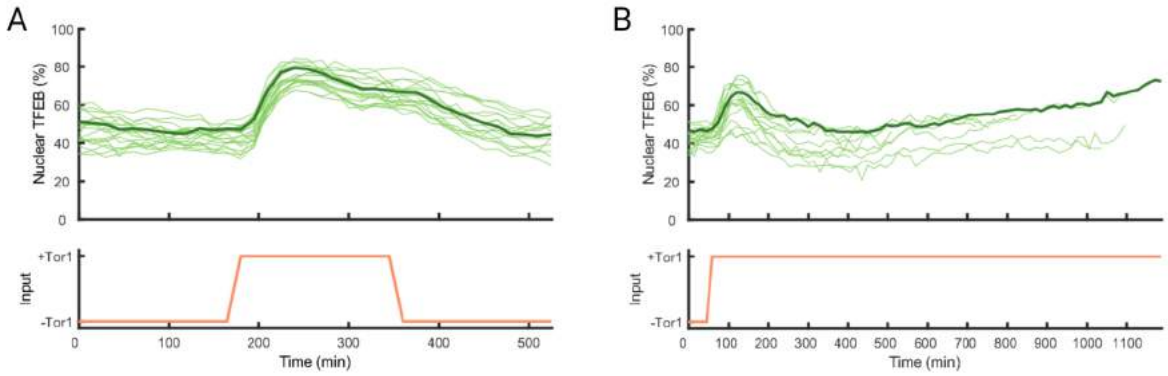

Figure 3.5: **Experimental measurements of TFEB translocation in the nucleus following mTOR inhibition.** TFEB translocation following a pulse (A) and a step (B) of mTOR inhibitor Torin 1 (Tor1) (300 nM). The figures show the single-cell traces of nuclear TFEB fluorescence. The average of the single-cell traces is highlighted with a solid line.

the small molecules used.

3.2.1 mTOR inhibition

The major complex responsible for TFEB phosphorylation and retention in the cytoplasm, thus keeping it inactive, is the mTORC1 complex, as explained in Chapter 1. The literature describes how TFEB is dephosphorylated and translocates into the nucleus following mTOR inhibition after amino acids depletion or full fasting, or by means of small molecules [47, 62, 76, 101]. I was curious to learn more about mTOR's function in the adaptation process as it is one of the key actors in TFEB shuttling. As a result, I ran two tests in which I used the chemical inhibitor Torin 1 to block mTOR kinase activity. Torin 1 is a potent and selective ATP-competitive inhibitor of mTOR [87].

Complete RPMI with or without Torin 1 was supplied to cells in two experiments, a pulse (Figure 3.5 A) and a step response (Figure 3.5 B).

As predicted from literature, the experimental results shown in Figure 3.5 demonstrate that TFEB translocates into the nucleus following Torin 1 administration. The most intriguing finding is that the overshoot dynamic still dominates TFEB nuclear shuttling even when mTOR is pharmacologically inhibited. As it was previously mentioned, both fasting and Torin 1 treatment induce TFEB nuclear import by blocking mTOR. Therefore, all of the experiments that have been discussed up to this point imply that, in general, the adaptation mechanism is activated after mTOR inhibition.

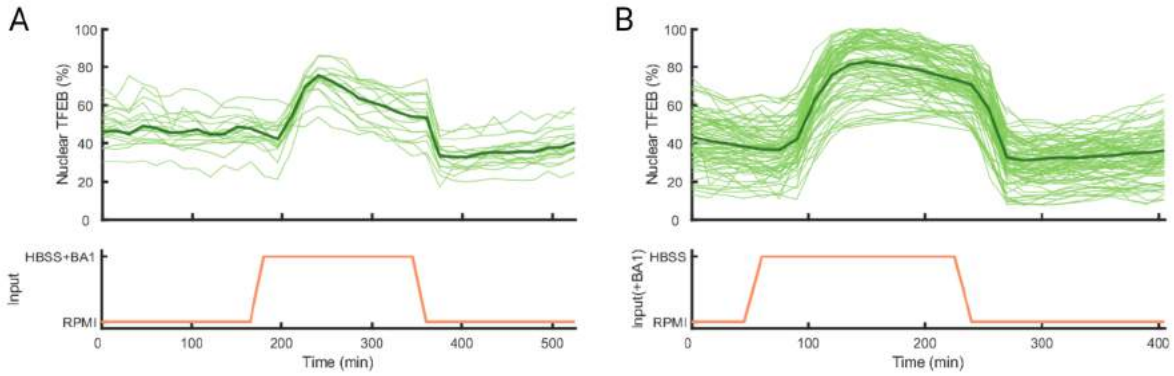

Figure 3.6: **Experimental measurements of TFEB translocation to the nucleus following starvation during autophagy inhibition.** TFEB translocation following a pulse of starvation medium (HBSS) supplied with the autophagy inhibitor Bafilomycin A1 (BA1) (100 nM) without (A) and with (B) pretreatment. The figures show the single-cell traces of nuclear TFEB fluorescence. The average of the single-cell traces is highlighted with a solid line.

In addition, these findings refute a prior hypothesis I formulated about the origin of the TFEB adaptation mechanism based on a partial reactivation of mTOR following starvation [80], as detailed in Chapter 4.

3.2.2 Autophagy inhibition

Autophagy is a fundamental catabolic process that relies on the cooperation of autophagosome and lysosomes. TFEB is a master regulator of starvation-induced autophagy and lysosomal biogenesis. By binding to CLEAR target sites in the promoters of lysosomal genes, TFEB positively regulates their expression [89]. I performed two experiments with Bafilomycin A1 to inhibit autophagy during starvation in an effort to determine if autophagy may affect TFEB nuclear location. Bafilomycin A1 disrupts autophagic flux by inhibiting both V-ATPase-dependent acidification and Ca-P60A/SERCA-dependent autophagosome-lysosome fusion [55].

The experiments were carried out by treating cells for three hours with a pulse of HBSS as starvation medium supplemented with Bafilomycin A1 without pretreatemnt (Figure 3.6 A) or with a pretreatment of one hour (Figure 3.6 B). The input was dynamically changed as described in Subsection 3.1.1.

The experimental results show that TFEB translocates to the nucleus after starvation under autophagy suppression, exhibiting the overshoot dynamic even in the presence of

Bafilomycin A1. This finding implies that autophagy activation does not affect TFEB nuclear shuttling kinetics.

3.2.3 Exportin 1 inhibition

Undoubtedly, one of the most significant pathways influencing TFEB localisation is its export, which is one of the most likely hypotheses that might account for the adaptation process. Exportin 1 (XPO1), of which TFEB has been identified as a strong binding partner, is the primary chaperone driving TFEB export [37, 62].

XPO1 is a nuclear export receptor involved in the transport a plethora of proteins and RNA species. XPO1 functions together with RAN GTPase, which supplies the energy for transportation and guarantees the directionality of nuclear export. In the nucleus, XPO1 binds to RAN in its active GTP-bound form (RAN-GTP) as well as the nuclear export signal (NES) on the proteins it is targeting. After docking to Nuclear Pore Complex (NPC), the complex enters the cytoplasm by crossing the nuclear membrane. The complex disassembles and cargoes are released into the cytoplasm as a result of the hydrolysis of RAN-GTP to RAN-GDP. The gradient in RAN-GTP concentration, which is primarily restricted to the nucleus, determines the directionality of XPO1-mediated export [6].

According to a recent study, silencing of XPO1 resulted in significantly reduced nuclear export of TFEB in HeLa cells after nutrient refeeding [62]. These findings suggested the hypothesis that the XPO1-dependent export is responsible for the overshoot kinetics of TFEB shuttling. I thus conducted a set of experiments by blocking Exportin 1 using the inhibitor Leptomycin B to explore its effect on the adaption process.

Leptomycin B is a metabolite of the *Streptomyces* bacteria that has anti-fungal, anti-tumor, and cytotoxic properties. It also inhibits nuclear export. Leptomycin B is the first known selective inhibitor of XPO1: it binds covalently to cysteine 528 in the region of XPO1 that binds nuclear export signals, preventing protein nuclear export. By binding to XPO1, Leptomycin B prevents its nuclear import, which causes XPO1 to be redistributed to the cytoplasm [42, 43].

As a first preliminary experiment, I treated cells with complete RPMI for three hours and then I switched cells to complete RPMI this time supplied with Leptomycin B for

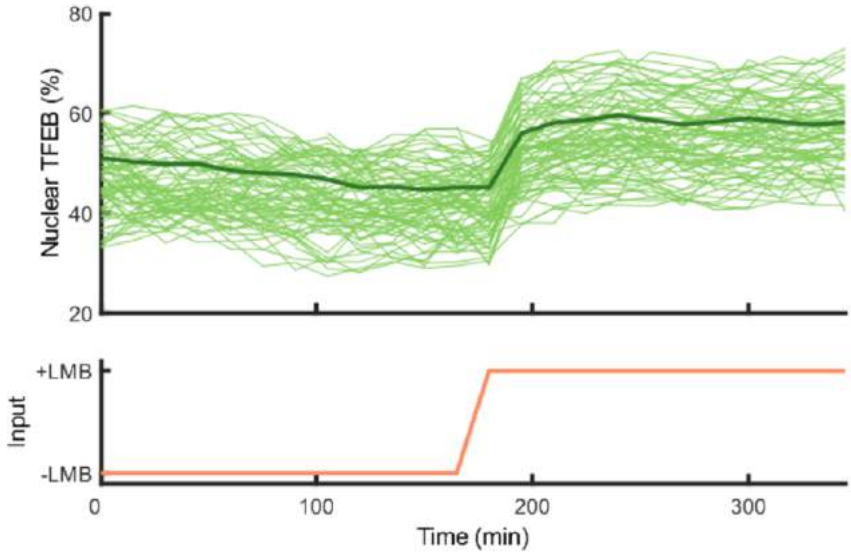

Figure 3.7: **Experimental measurements of TFEB translocation in the nucleus following Exportin 1 (XPO1) inhibition in growth medium (complete RPMI).** TFEB translocation following a pulse of Exportin 1 (XPO1) inhibitor Leptomycin B (LMB) (500 nM). The figure shows the single-cell traces of nuclear TFEB fluorescence. The average of the single-cell traces is highlighted with a solid line.

three hours (Figure 3.7). Here, it is possible to observe that TFEB nuclear concentration increases as the drug is administered, and then it reaches an equilibrium concentration after about half an hour without showing adaptation. These findings are in line with earlier research, which suggested that Leptomycin B treatment in fed cells, where TFEB is mostly localised in the cytoplasm, was sufficient to cause increasing accumulation of TFEB in the nuclear compartment [47, 62].

Consequently, I performed two further experiments by treating cells with a pulse of HBSS (Figure 3.8 A) or a pulse of Torin 1 (Figure 3.8 B) both supplemented with Leptomycin B. In both cases the overshoot in TFEB nuclear translocation dynamics is still present thus excluding XPO1 as a mechanism.

As shown in Figure 3.8 A, it is noteworthy to notice the differences with the starvation experiment performed in Figure 3.1 A. The import and export rates in each experiment were examined and compared: the export rate is twice as rapid as the import rate in the starvation experiment (Figure 3.1 A), whereas in the presence of Leptomycin B the export rate is slowed down to half of the import rate (Figure 3.8 A).

The nuclear concentration of TFEB also changes: its equilibrium nuclear concentration

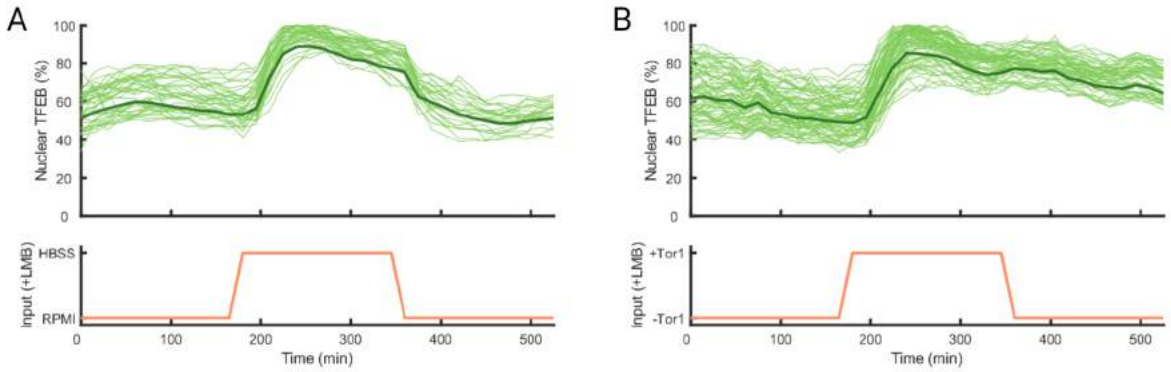

Figure 3.8: **Experimental measurements of TFEB translocation in the nucleus following starvation or mTOR inhibition during Exportin 1 (XPO1) inhibition.** (A) TFEB translocation following a pulse of starvation medium (HBSS) supplied with the Exportin 1 (XPO1) inhibitor Leptomycin B (LMB) (500 nM). (B) TFEB translocation following a pulse of mTOR inhibitor Torin 1 (Tor1) (1 μM) supplied with the Exportin 1 (XPO1) inhibitor Leptomycin B (LMB) (500 nM). The figures show the single-cell traces of nuclear TFEB fluorescence. The average of the single-cell traces is highlighted with a solid line.

is equal to about 30 percent during growth and 60 percent during starvation in the control experiment (Figure 3.1 A); instead when blocking Exportin 1 with Leptomycin B, the equilibrium nuclear concentration rises to about 50 percent during growth and 80 percent during starvation (Figure 3.8 A).

Similar conclusions may be drawn by comparing the outcomes of experiments where cells were given a pulse of Torin 1 that was either depleted (Figure 3.5 A) or supplemented (Figure 3.8 B) with Leptomycin B.

In summary, the experimental findings support the function of Exportin 1 in TFEB nuclear export by demonstrating how it affects equilibrium nuclear concentration and TFEB export dynamics. Nevertheless, these data imply that this is not a factor influencing the overshoot dynamics.

3.2.4 Proteasome inhibition

Cellular protein steady state levels are determined by protein-specific rate of synthesis and degradation. [29]. Accordingly, the dynamics of TFEB's synthesis and degradation might have an impact on its nuclear concentration in time.

The proteasome is primarily responsible for TFEB degradation [92]. In mammalian cells, the ubiquitin-proteasome system is the main mechanism for the degradation of unneeded

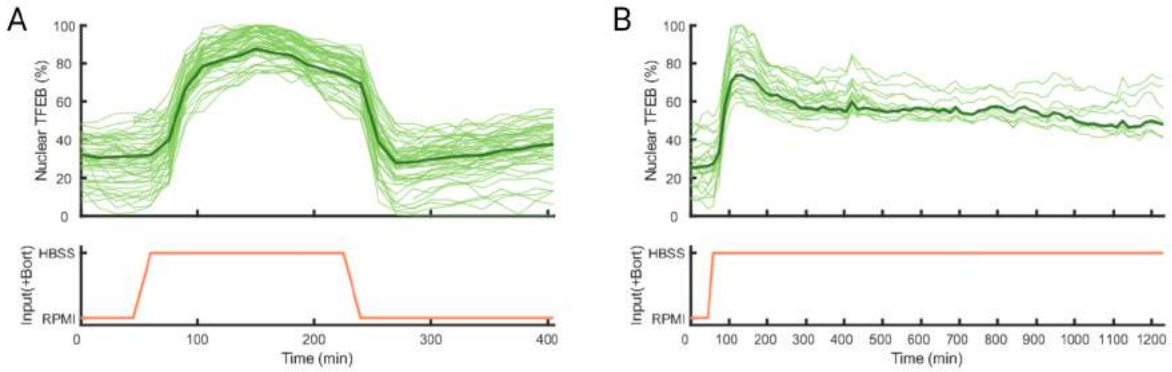

Figure 3.9: **Experimental measurements of TFEB translocation in the nucleus following starvation during proteasome inhibition.** TFEB translocation following a pulse (A) and a step (B) of starvation medium (HBSS) supplied with the proteasome inhibitor Bortezomib (Bort) (100 nM). The figures show the single-cell traces of nuclear TFEB fluorescence. The average of the single-cell traces is highlighted with a solid line.

or improperly folded proteins [29, 46]. The ATP-dependent ubiquitin-activating enzyme E1, ubiquitin-conjugating enzyme E2, and ubiquitin-protein ligase E3 successively catalyze the ubiquitination of target proteins gaining access to proteasomes. Proteasome consists of a 20S central catalytic complex and two 19S regulatory complexes. The target proteins are deubiquitinate and unfolded by the 19S complexes, allowing the proteins to reach the 20S proteasome and be quickly broken down by different proteases. Both the cytoplasm and the nucleus include proteasomes, which aid in the breakdown of nuclear and cytoplasmic proteins [46].

Recently, it has been reported that proteasome impairment not only promotes TFEB accumulation but also facilitates its dephosphorylation and nuclear translocation [46]. Accordingly, I performed two new experiments by inhibiting the proteasome by means of either one of the two small molecules MG132 (data not showed) and Bortezomib. Specifically, Bortezomib is a modified dipeptidyl boronic acid analogue that binds selectively and reversibly to the 20S proteasome. Inhibition of the proteasome prevents the degradation of key proteins and affects multiple signalling cascades within the cell, ultimately leading to cell death [16].

Cells were treated with HBSS as starvation medium supplemented with Bortezomib, with a pretreatment of one hour following a pulse (Figure 3.9 A) and a step response (Figure 3.9 B).

The purpose of these experiments was to assess the effects of TFEB degradation

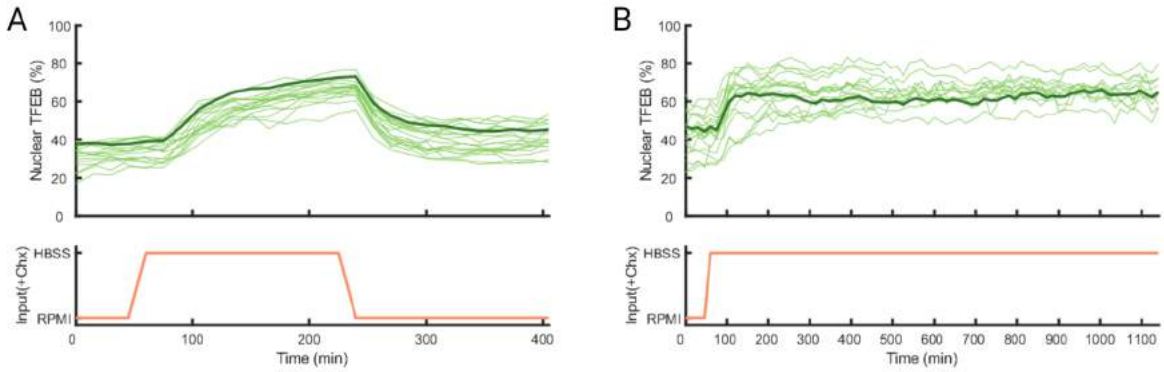

Figure 3.10: **Experimental measurements of TFEB translocation in the nucleus following starvation during translation inhibition.** TFEB translocation following a pulse (A) and a step (B) of starvation medium (HBSS) supplied with the translation inhibitor Cycloheximide (Chx) (50 μg/ml). The figures show the single-cell traces of nuclear TFEB fluorescence. The average of the single-cell traces is highlighted with a solid line.

impairment following mTOR inhibition. The experimental findings demonstrate that, irrespective of Bortezomib treatment, TFEB still translocates into the nucleus with an overshoot dynamic, thus excluding a role of TFEB degradation in this mechanism.

3.2.5 Translation and transcription inhibition

Here, I will examine the influence of TFEB synthesis to conclude the analysis that was begun in the previous Subsection.

The "central dogma" of life and molecular biology is mainly based on protein synthesis as primary process. The information required for protein synthesis, which entails the two processes of transcription and translation, is encoded by the nucleic acid sequences known as genes. An enzyme known as RNA polymerase copies the gene into an mRNA molecule during transcription. The information contained in the mRNA is converted by ribosomes during translation into a sequence of amino acids, which results in the production of a protein [3].

I performed experiments either by limiting general protein translation or gene transcription to see how this would affect TFEB nuclear localisation dynamics. Specifically, the small molecule Cycloheximide was used to block translation. Cycloheximide is a protein synthesis inhibitor in eukaryotes and an anti-fungal antibiotic. Although its exact mode of action is still unknown, it has been demonstrated to prevent translation elongation by attaching to the 60S ribosomal unit's E-site and interfering with deacetylated tRNA [88].

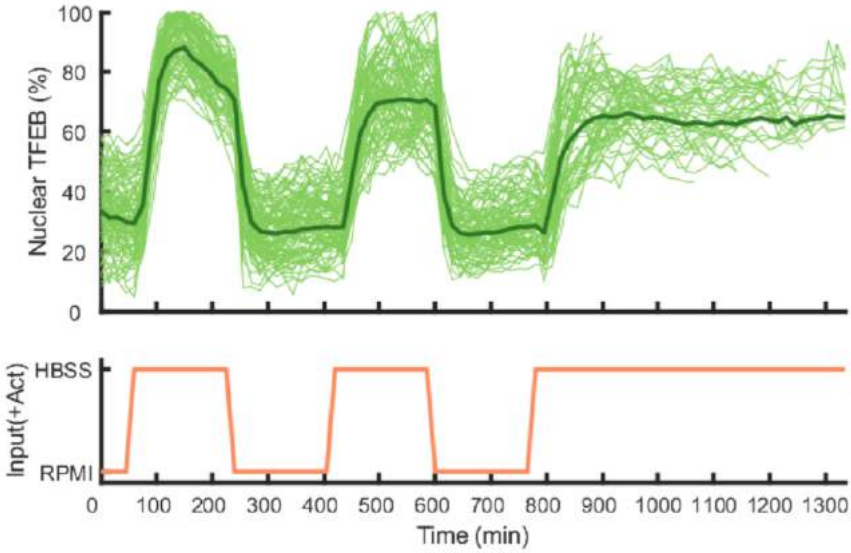

Figure 3.11: **Experimental measurements of TFEB translocation in the nucleus following starvation during transcription inhibition.** TFEB translocation following a starvation medium (HBSS) pulse train supplied with the transcription inhibitor Actinomycin D (Act) (50 ng/ml). The figure shows the single-cell traces of nuclear TFEB fluorescence. The average of the single-cell traces is highlighted with a solid line.

Actinomycin D was instead used to block transcription. By attaching to DNA at the transcription initiation complex and blocking RNA polymerase from extending the RNA chain, Actinomycin D suppresses transcription [9].

Two experiments were conducted treating cells with HBSS supplemented with Cycloheximide following a pulse (Figure 3.10 A) and a step response (Figure 3.9 B), both pretreated for one hour.

When starving medium is administered to the cells, TFEB translocates to the nucleus but the overshoot fully vanishes, while the rise dynamics of nuclear TFEB translocation are slowed down. These data are consistent with the hypothesis that protein synthesis is involved in the dynamics of shuttling since the overshoot disappears following its inhibition.

In a third experiment, I treated cells with a starvation pulse train supplied with Actinomycin D (Figure 3.11) for a total of twenty-one hours to further demonstrate the significance of protein synthesis. Here, cells underwent an hour-long pretreatment. The two media, RPMI and HBSS, which were both provided with Actinomycin D, were switched with a period of six hours and a duty cycle of fifty percent for twelve hours. Finally, the cells were starved until the conclusion of the experiment.

When starvation medium is administered in the first pulse, as shown in Figure 3.11, TFEB translocates in the nucleus with an overshoot dynamics. The translocation dynamics then shifts in the next two pulses in a manner similar to that seen following treatment with Cycloheximide. This behavior suggests that Actinomycin D requires more than one hour of pretreatment to be active since part of the mRNA to be degraded is probably still present at the beginning of the experiment.

These results imply that protein synthesis may play a part in the adaptive process that TFEB exhibits after mTOR inhibition. Nevertheless, it is vital to keep in mind that transcription, translation, and proteasome degradation are such crucial mechanisms that when they are blocked, they may have unanticipated consequences on myriads of pathways, which might affect the outcomes. As a result, it is difficult to interpret these data and they cannot serve as proof of their involvement in such a mechanism.

Chapter 4

Quantitative Modelling of TFEB nuclear shuttling

Having ascertained the complexity and singularity of the biological system under investigation, I propose in this Chapter a computational approach based on quantitative modelling of TFEB nuclear shuttling dynamics.

At first, I describe a preliminary analysis based on models, that I named "classics", which enable to draw attention to some preliminary results. The classic models serve as the basis for a second, more rigorous analysis, in order to select the optimal model, that is the model capable of accurately reproduce all the experimental data discussed in Chapter 3.

The findings made at the end of this computational characterisation will provide a specific hypothesis that is most likely to explain the overshoot dynamics observed in TFEB nuclear shuttling.

4.1 Static and Dynamic Experimental Features

The experimental data detailed in Chapter 3 show that the biological system under study exhibits dynamics that are far more complicated than what would be predicted based solely on the existing literature. TFEB nuclear accumulation changes in response to a variety of stimuli, appearing coherent in the majority of experiments but acting unexpectedly in some relevant cases, such as when Leptomycin B is administered (Figure 3.8).

In this Chapter, I describe a computational approach based on mathematical modelling to reveal the key players driving TFEB nuclear shuttling dynamics. The main goal is to develop a mathematical model that is consistent with the evidences in the TFEB literature and the chemical reactions that governs its activity in order to reproduce the dynamics of the system *in silico*. In the paragraphs that follow, I will propose different models based on assumptions that are supported by the literature. I will next evaluate the performances of each model in order to choose the one that can most accurately reproduce the experiments that I discussed in Chapter 3.

In particular, it is possible to extrapolate significant features able to help and improve the rigor of the analysis. Figure 4.1 reports the experimental data that will be used to assess the models.

Generally, it is possible to distinguish between two types of features: "Static" and "Dynamic". Static features account for how the dynamics of a biological system behave at equilibrium, when the system stabilizes following an initial transient behavior. The studies shown in Figure 4.1 demonstrate that two distinct static properties can be distinguished:

S1 For all the treatments shown in Figure 4.1, the TFEB nuclear concentration is never 100 percent nuclear nor 100 percent cytoplasmic.

S2 Leptomycin B treatment increases the nuclear concentration of TFEB both during growth or following Torin 1 treatment (or starvation) (Figures 4.1 A-D).

Dynamic features account for how a biological system behaves during its initial transient dynamic before achieving equilibrium. According to the experiments shown in Figure 4.1, three distinct dynamic features can be identified:

D1 The TFEB nuclear concentration exhibits an overshoot dynamic during the initial transient dynamic (Figures 4.1 A-D).

D2 The TFEB nuclear concentration exhibits a first order dynamic with no overshoot following Leptomycin B treatment in growth medium (Figure 4.1 E).

D3 TFEB nuclear level during refeeding in the presence of Leptomycin B (Figures 4.1 B

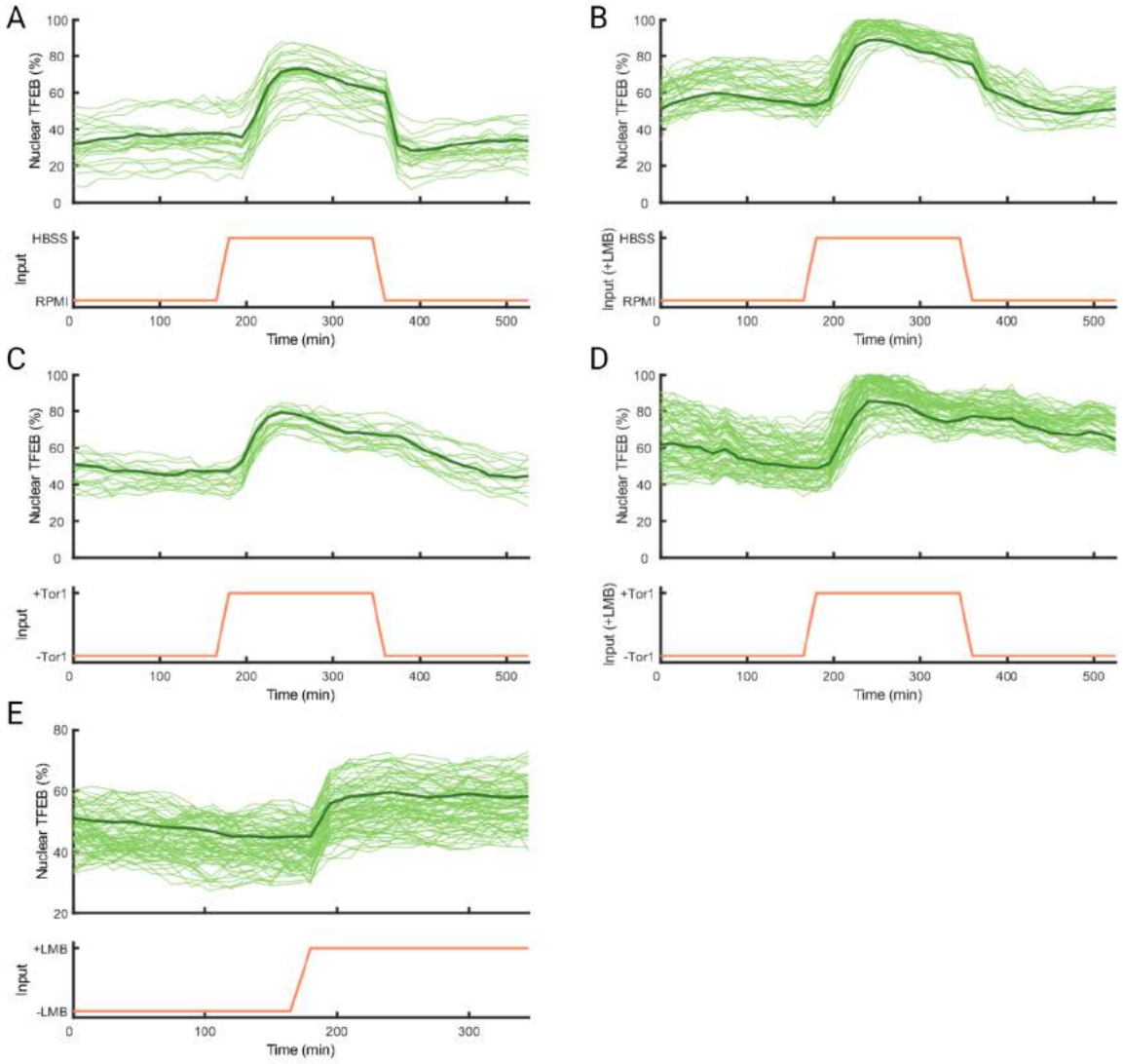

Figure 4.1: **Experimental measurements of TFEB translocation in the nucleus.** (A) TFEB translocation following a starvation medium (HBSS) pulse. (B) TFEB translocation following a starvation medium (HBSS) pulse supplied with the Exportin 1 (XPO1) inhibitor Leptomycin B (LMB). (C) TFEB translocation following a pulse of mTOR inhibitor Torin 1 (Tor1). (D) TFEB translocation following a pulse of mTOR inhibitor Torin 1 (Tor1) supplied with the Exportin 1 (XPO1) inhibitor Leptomycin B (LMB). (E) TFEB translocation following a pulse of Exportin 1 (XPO1) inhibitor Leptomycin B (LMB). The figures show the single-cell traces of nuclear TFEB fluorescence. The average of the single-cell traces is highlighted with a solid line.

and D) decreases at a slower rate than when Leptomycin B is absent (Figures 4.1 A and C).

As expected, the models must also contemplate the following in order to be consistent with the data from the literature:

- TFEB is inhibited through a phosphorylation in the cytoplasm by its kinase mTOR

in an input-dependent fashion [91]: under growth conditions the mTOR complex is active and phosphorylates TFEB; under starvation, or Torin 1 treatment, the mTOR complex is inhibited and TFEB is not phosphorylated anymore.

- The phosphatase Calcineurin dephosphorylates TFEB in the cytoplasm, activating it [56].
- The importin IPO7 or IPO8 imports TFEB into the nucleus [72, 106].
- Different kinases, including mTOR, ERK2, and GSK3β, phosphorylate TFEB in the nucleus [47, 62].
- TFEB is exported from the nucleus through the exportin XPO1 [37, 62].

The features and guidelines mentioned above will serve as benchmarks for creating the most reliable model.

4.2 Classic Model of TFEB nuclear translocation

I previously developed a preliminary model to describe the nuclear shuttling dynamics of TFEB, as reported in Figure 4.2 [80, 81]. In this Section, I will describe the model, which I will refer to as "Classic Model".

4.2.1 Introduction to the Classic Model

The model considers the presence of two compartments ([5]), the nucleus and the cytoplasm, through which TFEB shuttles ([62]). Within each compartment, de/phosphorylation reactions occur, in addition to two transport reactions to model TFEB transport. Remarkably, even though there is no evidence in the literature, the nuclear dephosphorylation is also taken into account in this model for symmetry. The possibility to reduce the model to only two states, as will be discussed in the next Subsection, justifies this decision. Then, I distinguished TFEB in four different species: (i) nuclear dephosphorylated ($TFEB_{nuc}$), (ii) nuclear phosphorylated ($TFEB^*_{nuc}$), (iii) cytoplasmic dephosphorylated ($TFEB_{cyt}$), (iv) cytoplasmic phosphorylated ($TFEB^*_{cyt}$). I assumed first order kinetics

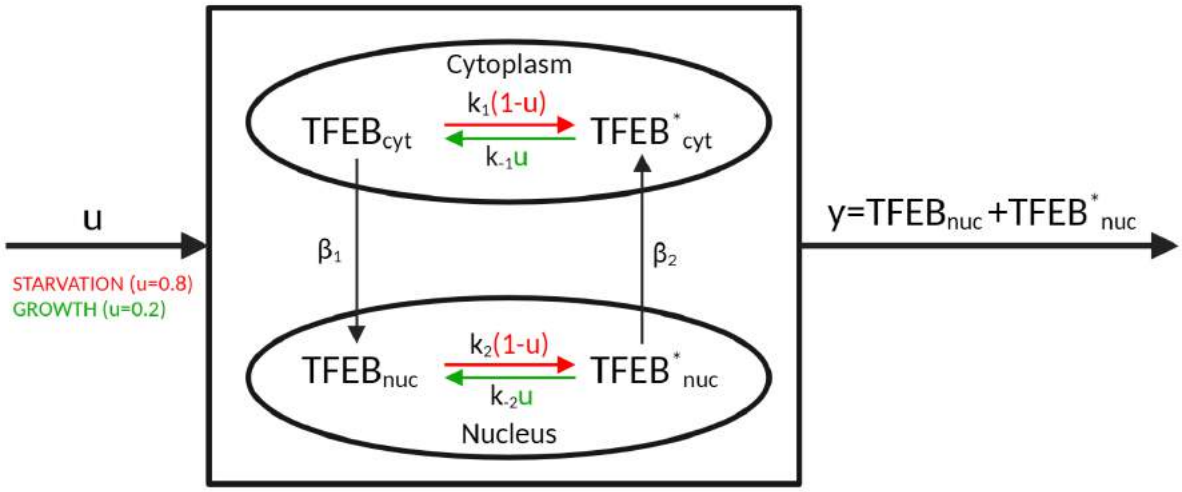

Figure 4.2: **Block scheme of the Classic Model.** $TFEB_{cyt}$ represents cytoplasmic TFEB; $TFEB_{nuc}$ the nuclear one; $TFEB^*_{cyt}$ and $TFEB^*_{nuc}$ are the respective phosphorylated species; k_i are the phosphorylation rates; k_{-i} the dephosphorylation ones; β_i the transport rates. The input u to the system represents the level of starvation and affects the de/phosphorylation rates. The input represents the growth condition for $u = 0.2$, and the starvation condition for $u = 0.8$. The output of the system y represents the nuclear concentration of TFEB, given by the sum of the two nuclear species $TFEB_{nuc}$ and $TFEB^*_{nuc}$.

for the de/phosphorylation and transport reactions ([83]). Furthermore, I considered the dependence of de/phosphorylation on the nutrients (amino acids) concentration by assuming a linear dependence of the reaction rates on the input u. Let $u \in [0, 1]$ be the external input to the system, where $u = 1$ corresponds to total starvation and $u = 0$ to total growth. More details about the values assumed by the input will be discussed in the Subsection 4.2.1. Let also x_C and x_N be respectively cytoplasmic and nuclear TFEB concentrations and x^*_C and x^*_N their phosphorylated counterparts. I further assumed that the total amount of TFEB protein is constant adding a conservation rule: $x_C + x_N + x^*_C + x^*_N = 1$. Moreover, I considered symmetric both the transport rates and the reaction rates, thus reducing the system parameters to two: (i) k that is the de/phosphorylation rate and (ii) β that is the transport rate. The two parameters were inferred from literature: $k = \frac{1}{70} = 1.5 \cdot 10^{-2}$,

$\beta = \frac{1}{216} = 5 \cdot 10^{-3}$ ([62]). The equations of the model are:

$$\dot{x}_C^* = k(1-u)(1-x_C^*-x_N-x_N^*) - kux_C^* + \beta x_N^*$$
$$\dot{x}_N = kux_N^* - k(1-u)x_N + \beta(1-x_C^*-x_N-x_N^*)$$
$$\dot{x}_N^* = k(1-u)x_N - kux_N^* - \beta x_N^*$$

In order to perform the system analysis, it is convenient to rewrite the system in matrix format [80]. Let $x = \begin{bmatrix} x_C^* & x_N & x_N^* \end{bmatrix}^T$ be the state vector.

$$\dot{x} = \begin{bmatrix} -k & k(u-1) & \beta + k(u-1) \\ -\beta & k(u-1) - \beta & ku - \beta \\ 0 & -k(u-1) & -ku - \beta \end{bmatrix} x + \begin{bmatrix} k(1-u) \\ \beta \\ 0 \end{bmatrix}$$

The equilibrium point of the system for a constant input u is:

$$\bar{x} = \begin{bmatrix} 1 - u - \frac{k}{\beta+k}u(1-u) \\ u - \frac{k}{\beta+k}u(1-u) \\ \frac{k}{\beta+k}u(1-u) \end{bmatrix}$$

Using Matlab *Symbolic Toolbox*, I computed also the *Jacobian* matrix and its eigenvalues (depending on a generic constant u that can assume as values only 0 and 1):

$$\lambda = \begin{bmatrix} -k \\ -\beta \\ -k-\beta \end{bmatrix}.$$

In this case, the eigenvalues are strictly negative and independent on input u, meaning that the equilibrium points are always stable nodes.

4.2.2 Classic Two-States Model

The ability to convert the Classic Model to a straightforward two-state model is one of its advantages. I will list every step and variable modification needed to get from a

three-state model to a two-state model in this Subsection.

Taking into account all the assumptions I mentioned before, but without taking the conservation rule into account, consider again the equations for the Classic Model:

$$\dot{x}_C = kux_C^* - k(1-u)x_C - \beta x_C$$
$$\dot{x}_C^* = k(1-u)x_C - kux_C^* + \beta x_N^*$$
$$\dot{x}_N = kux_N^* - k(1-u)x_N + \beta x_C$$
$$\dot{x}_N^* = k(1-u)x_N - kux_N^* - \beta x_N^*$$

Then, let introduce the change of variables:

$$\begin{bmatrix} t_{cyt} & t_{nuc} & t & t^* \end{bmatrix}^T = \begin{bmatrix} x_C + x_C^* & x_N + x_N^* & x_C + x_N & x_C^* + x_N^* \end{bmatrix}^T$$

This change of variables implies that:

$$\dot{t}_{cyt} = \dot{x}_C + \dot{x}_C^*$$
$$\dot{t}_{nuc} = \dot{x}_N + \dot{x}_N^*$$
$$\dot{t} = \dot{x}_C + \dot{x}_N$$
$$\dot{t}^* = \dot{x}_C^* + \dot{x}_N^*$$

Consequently, by replacing the expressions of $\dot{x}_C$, $\dot{x}_N$, $\dot{x}_C^*$, $\dot{x}_N^*$ and by simplifying:

$$\dot{t}_{cyt} = \beta(x_N^* - x_C)$$
$$\dot{t}_{nuc} = \beta(x_C - x_N^*)$$
$$\dot{t} = ku(x_C^* + x_N^*) - k(1-u)(x_C + x_N)$$
$$\dot{t}^* = k(1-u)(x_C + x_N) - ku(x_C^* + x_N^*)$$

Finally, by replacing the expressions of t_{cyt}, t_{nuc}, t and t^*:

$$\dot{t}_{cyt} = \beta(t^* - t_{cyt})$$
$$\dot{t}_{nuc} = \beta(t_{cyt} - t^*)$$
$$\dot{t} = kut^* - k(1-u)t$$
$$\dot{t}^* = k(1-u)t - kut^*$$

Let assume the two conservation rules: $t + t^* = c$ and $t_{cyt} + t_{nuc} = c$ where c is a generic constant value. These two conservation rules derives directly from the previous one: $x_C + x_N + x_C^* + x_N^* = 1$. Accordingly, the final model become:

$$\dot{t}_{nuc} = \beta(t - t_{nuc})$$
$$\dot{t} = k(uc - t)$$

Finally, the equilibrium point of the model is:

$$\begin{bmatrix} \bar{t}_{nuc} & \bar{t} \end{bmatrix}^T = \begin{bmatrix} uc & uc \end{bmatrix}^T$$

where $k, \beta \neq 0$.

The possibility to reduce the Classic Model to a two-state model is strictly related to the symmetry of its structure in terms of de/phosphorylation and transport rates. The two-state model allows to simplify the study of the biological system and represents one advantage of the Classic Model.

4.2.3 Numerical Simulations of Classic Model

In this Subsection, I performed numerical simulations, reported in Figure 4.3, to check whether the model could recapitulate the experimental data reported in Figure 4.1 and whether it is able to respect the static and dynamic features introduced in Section 4.1. I applied the same inputs to the model in any simulation. Each input has been simulated as a pulses train: it lasts a total of twenty hours, where the growth and the starvation

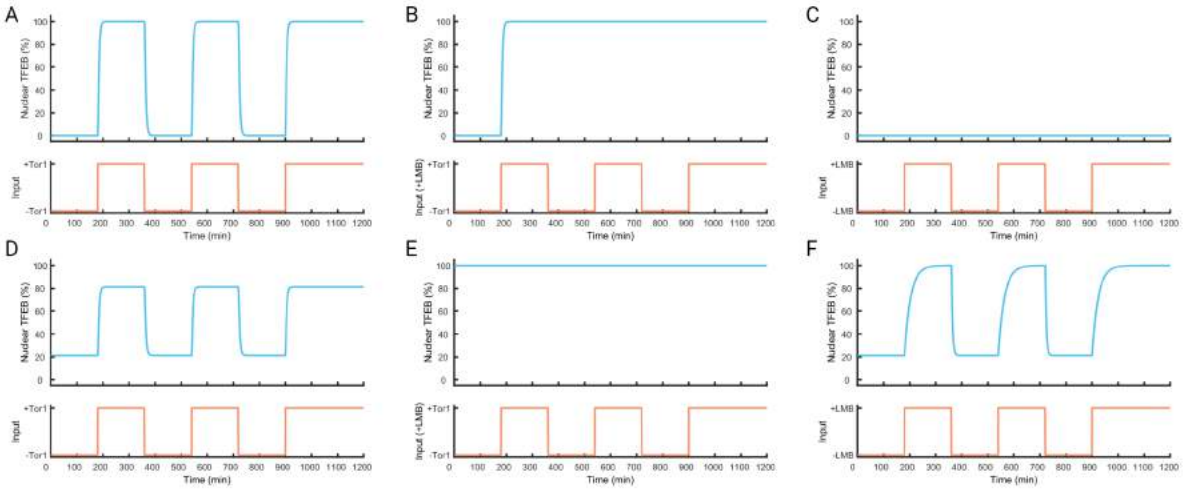

Figure 4.3: **Numerical Simulations of TFEB translocation for the Classic Model.** Simulations of TFEB translocation following a pulse train of Torin 1 (A,D), Torin 1 supplied with Leptomycin B (B,E), Leptomycin B (C,F). The input u used for panels (A,B,C) is $u = 0$ for the growth condition, and $u = 1$ for the starvation condition. The input u used for panels (D,E,F) is $u = 0.2$ for the growth condition, and $u = 0.8$ for the starvation condition.

(or other treatments) are switched with a period of six hours and a duty cycle of the fifty percent for twelve hours. Finally, the input is set to the treatment until the conclusion of the experiment.

Firstly, to recapitulate the Torin 1 (or starvation) pulse experiment (Figures 4.1 A and C), I switched the value of the input u between 0 and 1 to distinguish between growth and Torin 1 (or starvation) treatments. Here, it is possible to comment the first drawback of the model. Let evaluate the equilibrium points $\bar{x} = \begin{bmatrix} \bar{x}_C^* & \bar{x}_N & \bar{x}_N^* \end{bmatrix}^T$ in the two cases of $u = 0$ and $u = 1$. During Torin 1 (or starvation) ($u = 1$), TFEB is completely nuclear and dephosphorylated: $\bar{x} = \begin{bmatrix} 0 & 1 & 0 \end{bmatrix}^T$. Instead, during re-feeding, TFEB is completely cytoplasmatic and phosphorylated: $\bar{x} = \begin{bmatrix} 1 & 0 & 0 \end{bmatrix}^T$. By rewriting these results in therms of total cytoplasmic and nuclear concentrations at equilibrium $\bar{x}_{tot} = \begin{bmatrix} \bar{x}_{C,tot} & \bar{x}_{N,tot} \end{bmatrix}^T = \begin{bmatrix} \bar{x}_C + \bar{x}_C^* & \bar{x}_N + \bar{x}_N^* \end{bmatrix}^T$, I obtained that these values are: $\bar{x}_{tot} = \begin{bmatrix} 1 & 0 \end{bmatrix}^T$ when $u = 0$ and $\bar{x}_{tot} \begin{bmatrix} 0 & 1 \end{bmatrix}^T$ when $u = 1$. According to these results, the Classic Model is not able to satisfy the static feature ***S1*** for the pulse of Torin 1 (or starvation) experiments.

Figure 4.3 A reports the numerical simulation. The simulation confirms that TFEB is entirely nuclear during Torin 1 (or starvation) treatment, while is entirely cytoplasmic during

growth treatment. In addition, it is possible to appreciate that the model can reproduce the fast dynamics observed in the experiments during medium switches. Conversely, it is unable to reproduce the slower overshoot dynamic. Consequently, the Classic Model is not compatible with the dynamic feature ***D1*** for the Torin 1 (or starvation) experiment.

As a result, the Classic Model presents some limitations in its ability to reproduce the experimental results, at least for the selected input values. The model simulations of the experiments with Torin 1 (or starvation) with Leptomycin B or Leptomycin B alone (Figures 4.3 B and C) provide further evidences of the model limitations. Here, I simulated the Leptomycin B treatment by setting the parameter β_2 equal to zero, since it promotes the inhibition of the nuclear export. Let evaluate again the equilibrium points in the two cases of $u = 0$ and $u = 1$ when $\beta_2 = 0$. Here, $\bar{x} = \begin{bmatrix} 1 & 0 & 0 \end{bmatrix}^T$ ($\bar{x}_{tot} = \begin{bmatrix} 1 & 0 \end{bmatrix}^T$) when $u = 0$ and $\bar{x} = \begin{bmatrix} 0 & 1 & 0 \end{bmatrix}^T$ ($\bar{x}_{tot} = \begin{bmatrix} 0 & 1 \end{bmatrix}^T$) when $u = 1$. As depicted in Figures 4.3 B and C, the model completely fails to recapitulate the experimental data following Leptomycin B treatment.

In summary, The Classic Model is unable to reproduce the experimental data and is unable to recapitulate static and dynamic features, at least for the chosen input values.

Consequently, I decided to change the input values to enhance the model's performance. In particular, I switched the value of the input u between 0.2 and 0.8 to distinguish between growth and Torin 1 (or starvation) treatments; then, I repeated the model simulations, as reported in Figures 4.3 D-E. Referring to the model simulation of the Torin 1 (or starvation) pulse experiment reported in Figure 4.3 D, the model now is able to satisfy the static feature ***S1***. Conversely, the model fails to satisfy the dynamic feature ***D1*** again. This finding implies that the Classic Model is not capable of recapitulating the overshoot dynamic in general and places the emphasis on the structure of the model rather than the selection of parameter values.

Finally, in reference to the model simulations of Leptomycin B treatments reported in Figures 4.3 E and F, the model fails completely to recapitulate the experimental data. In particular, as β_2 is switched to zero to simulate the Leptomycin B treatment, TFEB accumulates completely in the nucleus regardless of the value of the input u. This result suggests that the model fails to recapitulate the experimental evidence since it predicts

total accumulation of TFEB in the nucleus when assuming a complete inhibition of nuclear export under Leptomycin B treatment.

In Conclusion, the Classic Model presents several limitations in recapitulating the experimental data and fails to satisfy static and dynamic features. The primary issues are outlined below:

- The structure of the model is not suitable for an input value that switches between 0 and 1; consequently I forced the input to switch between 0.2 and 0.8 that corresponds to two intermediate conditions of growth and starvation.

- The structure of the model is inadequate to simulate the overshoot dynamics. This finding shows that the model itself is not sufficient to fully capture the dynamics that were observed empirically.

- Numerical simulations do not support the hypothesis that Leptomycin B treatment entirely suppresses the TFEB nuclear export. Indeed, regardless of the value of the input u, TFEB accumulates entirely in the nucleus as β_2 is set to zero to simulate the Leptomycin B treatment. This finding raises the possibility of an export independent of XPO1 and, hence, independent of Leptomycin B. As a matter of fact, its existence would explain why TFEB partially accumulates in the nucleus when XPO1 is inhibited.

The structure of the model and the consequent dependency of the de/phosphorylation rates on the input itself significantly restrict the range of values that the input can adopt. Therefore, this obstacle can only be removed by changing the structure of the model and the dependence of the rates on the input. This point will be addressed in Section 4.3.

4.2.4 Classic NFL and IFFL Models

Subsection 4.2.3 focuses the attention on the Classic Model limitations. In this Subsection, I will present hypotheses based on the theory and on the literature with the purpose to improve the performances of the model and its reliability.

The starting point relates to understanding how to ensure that the model can recapitulate the overshoot dynamics. From Figures 4.1 A and C, it is possible to observe that the

overshoot dynamic is much slower than the initial TFEB response to starvation (or Torin 1). In particular, TFEB enters the nucleus in about half hour, while the overshoot takes more than two hours to occur. Consequently, I hypothesized that another slower biological mechanism could be responsible for this behavior.

The negative feedback loops (NFLs) and incoherent feed-forward loops (IFFLs) are the only two gene network motifs that can give rise to adaptation ([77]). This observation led me to conjecture the presence of an unknown species that could regulate the nuclear amount of TFEB through either a NFL or an IFFL network motif. Considering the biological process represented in Figure 2.10 and the block scheme proposed in Figure 4.2, I reasoned that if present, such a species could influence either the phosphorylation state of TFEB, or alternatively its nuclear transport.

I first investigated the hypothesis that the overshoot is caused by a negative feedback acting on TFEB phosphorylation as a result of a partial reactivation of the mTOR kinase, as inferred from the recent findings in the literature ([47,52,62]). Under starvation TFEB is dephosphorylated and enters the nucleus activating autophagic genes. Autophagy promotes the generation of a pool of amino acids used by the cell to survive in this situation of stress. The hypothesis is that the cellular nutrient sensing machinery detects the presence of these extra-nutrients and partially reactivates mTOR, which in turn phosphorylates TFEB causing its partial nuclear export.

I experimentally tested *in vitro* the reliability of this mTOR reactivation hypothesis. To this end, I performed an experiment treating cells with a step response of starvation medium (HBSS) supplied with the mTOR inhibitor Torin 1. As shown in Figure 4.4 A, the overshoot dynamic is still present despite mTOR being fully inhibited, and it is comparable with the dynamics already observed in Figure 4.1 A. In addition, the adaptation mechanism is also activated with the sole administration of Torin 1 in the growth medium, as depicted in Figure 4.1 C. These observations suggest that this hypothesis is not supported by experimental evidence.

I thus hypothesized that the unknown species may affect TFEB nuclear export rates through either a negative feedback loop, or an incoherent feedforward loop [81], as schematically depicted in Figures 4.4 B and C. In order to test the new hypotheses, I

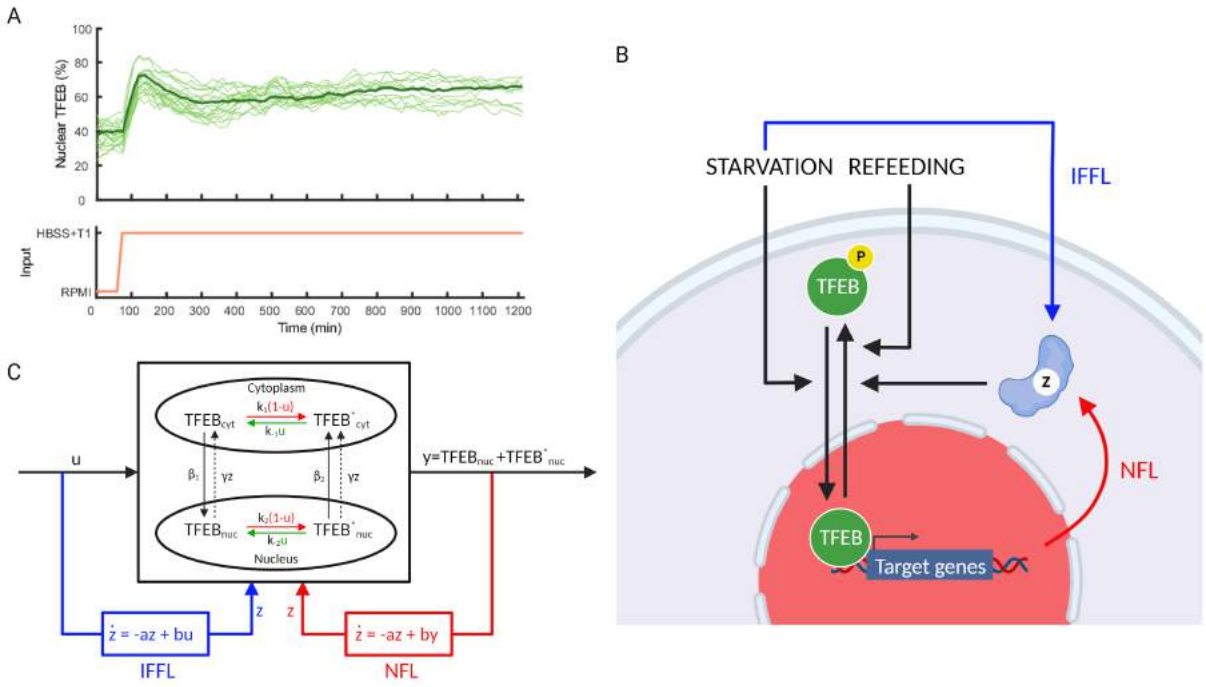

Figure 4.4: **Two alternative models of TFEB dynamics.** (A) Experimental measurements of TFEB translocation following a step response of starvation medium (HBSS) supplied with the mTOR inhibitor Torin 1 (T1) (1 μM). The figure shows the single-cell traces of nuclear TFEB fluorescence. The average of the single-cell traces is highlighted with a solid line. (B) Biological hypothesis: an unknown species z is produced or activated following the nuclear translocation of TFEB (NFL, in red) or following starvation (IFFL, in blue), influencing TFEB cellular localisation through a negative feedback or a feedforward action. (C) Block scheme of the negative feedback regulation hypothesised for the overshoot dynamics is represented in red. The production of the new species z depends on the total amount of nuclear TFEB y. Block scheme of the incoherent feedforward regulation hypothesised for the overshoot dynamics is represented in blue. The production of the new species z depends on the input u. In both cases, the z species acts as a transporter able to export nuclear TFEB.

developed two alternative models by adding a species z, able to increase TFEB export from the nucleus to the cytoplasm with a rate γ, independently of its phosphorylation state. The NFL model can be formalised as follows:

$$\begin{aligned}
\dot{x}_C^* &= k(1-u)(1-x_C^*-x_N-x_N^*) - kux_C^* + \beta x_N^* + \gamma z x_N^* \\
\dot{x}_N &= kux_N^* - k(1-u)x_N + \beta(1-x_C^*-x_N-x_N^*) - \gamma z x_N \\
\dot{x}_N^* &= k(1-u)x_N - kux_N^* - \beta x_N^* - \gamma z x_N^* \\
\dot{z} &= -az + b(x_N + x_N^*)
\end{aligned}$$

Here, a and b are respectively the degradation and the production rates of z. Parameter

a was set according to the experimental slow overshoot dynamics (in the order of three hours). Parameter b was set according to the experimental equilibrium reached by the system (60 percent of nuclear TFEB, as shown in Figure 3.1 B). Therefore, the parameters were set equal to: $a = 1.5 \cdot 10^{-4}$, $b = 8.8 \cdot 10^{-5}$. The transport rate γ was assumed to be slower than the preferential XPO1-dependent export and was set equal to $\frac{\beta}{5}$.

As previously discussed, the NFL architecture is not the only plausible architecture able to biologically explain this phenomenon. Consequently, I hypothesized an alternative model acting via an incoherent feedforward loop (IFFL) model, as shown in Figures 4.4 B and C (in blue). In the IFFL model, the production of the z species directly depends on the input and not on the nuclear concentration of TFEB as in the NFL. The IFFL model equations are:

$$\begin{aligned}
\dot{x}_C^* &= k(1-u)(1-x_C^*-x_N-x_N^*) - kux_C^* + \beta x_N^* + \gamma z x_N^* \\
\dot{x}_N &= kux_N^* - k(1-u)x_N + \beta(1-x_C^*-x_N-x_N^*) - \gamma z x_N \\
\dot{x}_N^* &= k(1-u)x_N - kux_N^* - \beta x_N^* - \gamma z x_N^* \\
\dot{z} &= -az + bu
\end{aligned}$$

In order to test how well these models recapitulated the experimental results, I characterized them *in silico* by performing new simulations, as described in the next Subsection.

4.2.5 Numerical Simulations of Classic NFL and IFFL Models

In this Subsection, I performed numerical simulations, reported in Figure 4.5, to check whether the two new models are able to improve the performances of the Classic Model. The conditions used to perform the computational analysis are the same as in Subsection 4.2.3.

According to the observations discussed in the Subsection 4.2.3, I repeated the simulations considering that the input u is equal to 0.2 under growth treatment and to 0.8 under Torin 1 (or starvation) treatment. In addition, I simulated the Leptomycin B treatment by setting the parameter β_2 equal to zero. Indeed, the novel species z functions as an extra nuclear exporter independently from XPO1 and therefore insensitive to Leptomycin

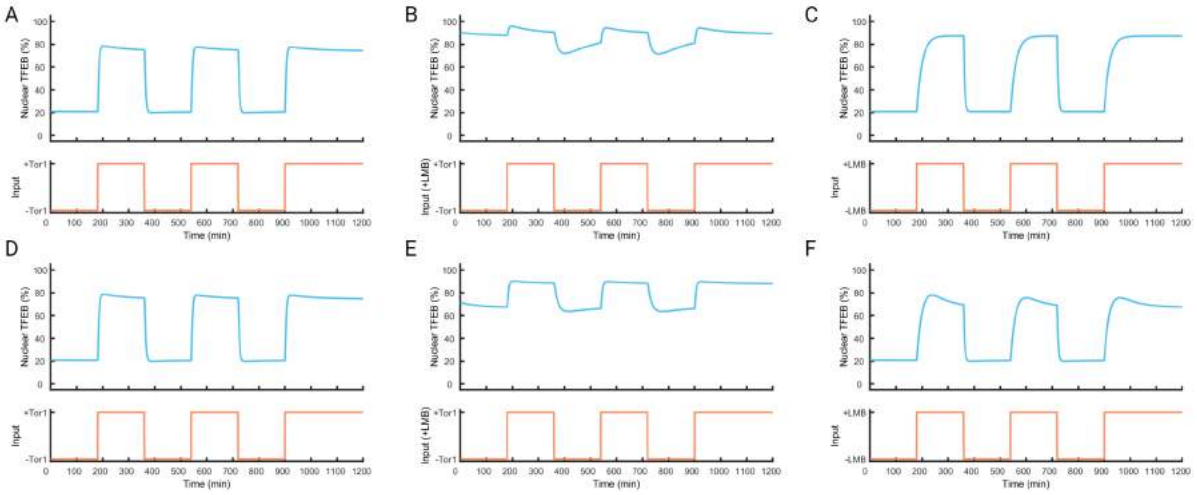

Figure 4.5: **Numerical Simulations of TFEB translocation for the Classic IFFL and NFL Models.** Panels (A,B,C) report IFFL model numerical simulations; panels (D,E,F) report NFL model numerical simulations. Simulations of TFEB translocation following a Torin 1 pulse train (A,D), a Torin 1 pulse train supplied with Leptomycin B (B,E) and a Leptomycin B pulse train (C,F). The input u used is $u = 0.2$ for the growth condition, and $u = 0.8$ for the starvation condition.

B treatment. The numerical simulations of the Torin 1 pulse experiment of the IFFL and NFL Models are reported in Figures 4.5 A and D, respectively. Here, it is possible to observe that the models are able to qualitatively recapitulate the experimentally observed overshoot dynamics. Both the simulations clearly show the fast rise, the overshoot, the new equilibrium, and the fast decrease. The equilibrium values under growth and Torin 1 (or starvation) treatment are above 0 percent and below 100 percent respectively, indicating that both models satisfy the static feature ***S1***. In addition, the models recapitulate the overshoot dynamics, indicating that both models satisfy the dynamic feature ***D1***.

The numerical simulations of Torin 1 (or starvation) pulse supplied with Leptomycin B experiment of the IFFL and NFL models are reported in Figures 4.5 B and E, respectively. Again, the models are able to recapitualte qualitatively the entire dynamics observed experimentally. Here, the equilibrium values under growth and Torin 1 (or starvation) treatment supplied with Leptomycin B are above 0 percent and below 100 percent respectively, indicating that both models satisfy the static feature ***S1***. In addition, the nuclear concentration of TFEB at equilibrium is also higher than the one in the simulation of the Torin 1 (or starvation) pulse experiment, indicating that both models satisfy the static feature ***S2***. Moreover, the overshoot dynamics are well recapitulated, indicating that the

models satisfy the dynamic feature ***D1***. Finally, the Fall rates in both simulations slowed down as compared to those of the Torin 1 pulse experiment, indicating that the models satisfy the dynamic feature ***D3***. In summary, both the models are able to qualitatively replicate all of the experimental observed dynamics and are able to satisfy the relative static and dynamic experimental features.

The numerical simulations of the Leptomycin B pulse experiment of the IFFL and NFL models are reported in Figures 4.5 C and F, respectively. These numerical simulations represent the best *in silico* test to distinguish between the two models [81]. Indeed, the main difference between the two models lies in the adaptation mechanism. In the IFFL model, the adaptation is directly driven by starvation, while in the NFL model, the adaptation is caused by TFEB accumulating in the nucleus (Figures 4.4 B and C). Experimental discrimination between the two models is not trivial because of the correlation between the nutrients concentration in the cellular environment and the TFEB amount in the nucleus. Nevertheless, the inhibition of nuclear export in cells grown in nutrient-rich medium can be used to decouple TFEB nuclear accumulation from starvation, and thus distinguish between the two models. Indeed, by impairing the balance between the nuclear input flux and nuclear export flux, there should be an increase of the nuclear TFEB concentration. This increase of TFEB nuclear concentration will result in a different outcome according to the model considered: in the IFFL, the overshoot should not be present, since the nutrients concentration remains unaltered; on the other hand, in the NFL model, TFEB nuclear accumulation will lead to the activation of the new transporter and consequently to the appearance of the overshoot. As expected, the simulations reported in Figures 4.5 C and F show that the NFL shows adaptation while IFFL does not, indicating that only the IFFL model is able to satisfy the dynamic feature ***D2***. In addition, both models satisfy the static feature ***S1*** since the equilibrium values under growth and Leptomycin B treatments are above 0 percent and below 100 percent, respectively.

In conclusion, I demonstrated *in silico* that both the NFL and IFFL Models improve the performances of the Classic Model. The IFFL model was able to recapitulate all the experimental data and to satisfy all the static and dynamic experimental features. Conversely, the NFL model failed to recapitulate the Leptomycin B pulse experiment and

does not satisfy the dynamic feature ***D2***. This limit is intrinsic in the model structure and allowed to distinguish the nature of NFL and IFFL as two different network motifs. According to these results, the IFFL mechanism better recapitulates the observed dynamics, suggesting that this topology is more reliable than the NFL to describe the biological system.

4.3 Optimal Model

The modelling approach proposed in the previous Section highlighted important features and suggested a plausible hypothesis to explain the biological mechanism behind the complex TFEB dynamics. Specifically an IFFL network motif may explain the observed TFEB nuclear shuttling dynamics assuming an extra species that drive an XPO1 independent nuclear export. Despite the relevance of this preliminary analysis, a limitation of the model is that I had to assume that the input u had to be greater than 0 and less than 1 in order to prevent TFEB to become 100 percent nuclear following Torin 1 (or starvation) treatment and 100 percent cytoplasmic in nutrient rich condition. From a biological point of view this modelling assumption is equivalent to state that Torin 1 (or starvation) treatment do not fully block mTOR kinase activity, which is not supported by the literature and by the scientific consensus.

In this Section I propose a study based on a rigorous analysis to overcome this limitation and to select the best model, namely the optimal minimal model.

4.3.1 Introduction to the Alternative Models

In this Subsection, I will describe how I derived the Alternative Models where the input u is forced to strictly switch between $u = 1$ (full mTOR inhibition in starvation) and $u = 0$ (full mTOR activation in growth). Overall, I generated twelve different models, as reported in Figure 4.6.

The general structure of the Alternative Model follows the usual two-compartments (nucleus and cytoplasm) model. Within each compartment, de/phosphorylation reactions occur, and any possible transport reaction was assumed to model TFEB transport. I as-

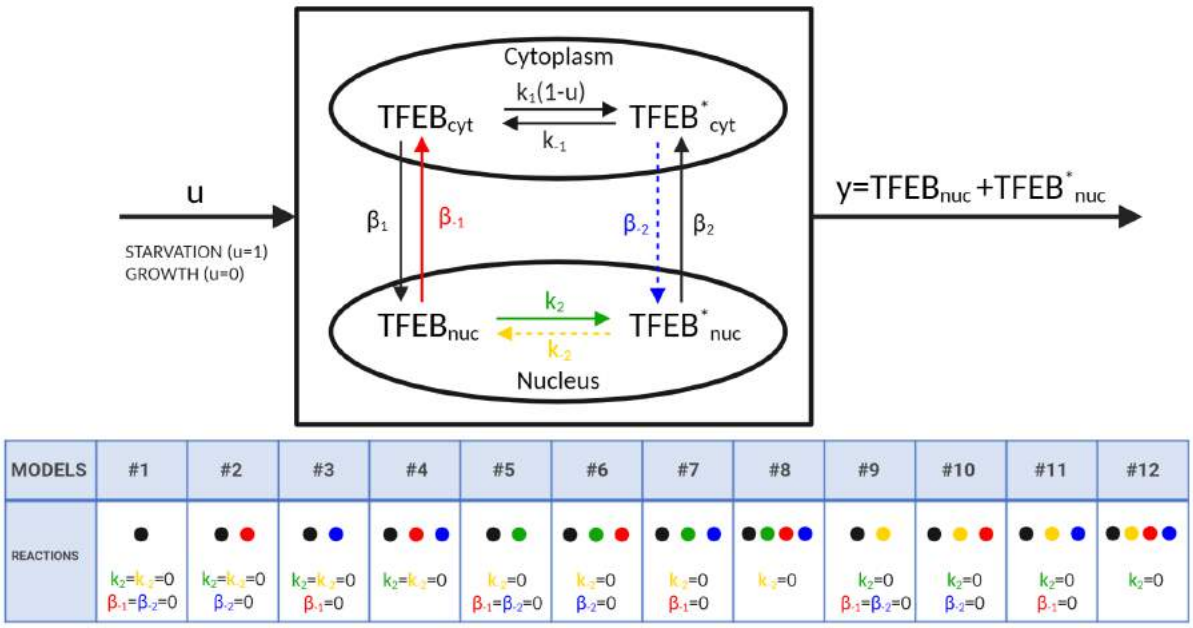

Figure 4.6: **General Block scheme of the Alternative Models proposed.** In the scheme $TFEB_{cyt}$ represents cytoplasmic TFEB; $TFEB_{nuc}$ the nuclear one; $TFEB^*_{cyt}$ and $TFEB^*_{nuc}$ are the respective phosphorylated species; k_i are the phosphorylation rates; k_{-i} the dephosphorylation ones; β_i the transport rates. The input u to the system represents the level of starvation and affects the cytoplasmic phosphorylation rate. The input represents the growth condition for $u = 0$, and the starvation condition for $u = 1$. The output of the system y represents the nuclear concentration of TFEB, given by the sum of the two nuclear species $TFEB_{nuc}$ and $TFEB^*_{nuc}$. The arrows represented with a solid line describe the chemical reactions reported in literature. The arrows represented with a dashed line describe the chemical reactions not reported in literature: their existence is not confirmed. The legend on the bottom describes the choice of the parameters for each model. In particular: the colored circles indicate the reactions belonging to each model; then, it is also reported which parameter is set to zero.

sumed first order kinetics for all the reactions. Again, I distinguished TFEB in four different species: (i) nuclear dephosphorylated ($TFEB_{nuc}$), (ii) nuclear phosphorylated ($TFEB^*_{nuc}$), (iii) cytoplasmic dephosphorylated ($TFEB_{cyt}$), (iv) cytoplasmic phosphorylated ($TFEB^*_{cyt}$). In this case, I only considered the cytoplasmic phosphorylation as dependent on the nutrients (amino acids) concentration by assuming a linear dependence on the input u. Let x_C and x_N be respectively cytoplasmic and nuclear TFEB concentrations and x^*_C and x^*_N their phosphorylated counterparts. Considering the conservation rule: $x_C + x_N + x^*_C + x^*_N = 1$,

the equations of the general Alternative Model are:

$$\dot{x}_C^* = k_1(1-u)(1-x_C^*-x_N-x_N^*) - k_{-1}x_C^* + \beta_2 x_N^* - \beta_{-2}x_C^*$$
$$\dot{x}_N = k_{-2}x_N^* - k_2 x_N + \beta_1(1-x_C^*-x_N-x_N^*) - \beta_{-1}x_N$$
$$\dot{x}_N^* = k_2 x_N - k_{-2}x_N^* + \beta_{-2}x_C^* - \beta_2 x_N^*$$

All of the de/phosphorylation and transport rates are considered in the general model equations. Clearly, the twelve different models are characterized by different combinations of the reactions, as described in the legend in Figure 4.6. The main features of the Alternative Models structures are as follows:

- Models from 1 to 4 are all characterized by the absence of nuclear de/phosphorylation reactions.
- Models from 5 to 8 are all characterized by the presence of the nuclear phosphorylation reaction.
- Models from 9 to 12 are all characterized by the presence of the nuclear dephosphorylation reaction.

Within each set of models, there are different combinations of transport rates between compartments. The aim is to understand which model is able to reproduce the experimental dynamics.

Of note, some of the models include also the nuclear dephosphorylation of TFEB (yellow arrow in Figure 4.6) and the cytoplasmic phosphorylated TFEB import (blue arrow in Figure 4.6) all of which have never been reported in literature. This study will make it possible to question their usefulness and the possibility of their existence.

In order to test the models according their ability to satisfy the static and the dynamic features described in Section 4.1, the models will be specifically tested by dividing the analysis into two parts: firstly, the static properties of any model will be evaluated; then, the dynamics of the models that satisfy all the static features will be studied.

4.3.2 Static Analysis of the models

In the following Subsection, I will evaluate whether the models are able to satisfy the static features ***S1*** and ***S2***. For this purpose, the equilibrium point of each model will be evaluated in the main cases of interest. Generally, the static and dynamic features were defined with respect to the experimental data reported in Figure 4.1. Accordingly, the equilibrium points must be evaluated in the specific cases when growth and Torin 1 (or starvation) treatments are administered in the presence or absence of Leptomycin B. As previously commented, the growth condition is simulated by setting the input u to 0, while the Torin 1 (or starvation) condition by setting u to 1. Finally, I simulated the Leptomycin B treatment by setting the parameter β_2 equal to zero, since it promotes the inhibition of the nuclear export as previously discussed. The study will be conducted by evaluating the equilibrium points in the form $\begin{bmatrix} \bar{x}_C^* & \bar{x}_N & \bar{x}_N^* \end{bmatrix}^T$ (the Appendix A reports the pertinent tables) and the cytoplasmic and nuclear concentrations at equilibrium in the form $\begin{bmatrix} \bar{x}_C + \bar{x}_C^* & \bar{x}_N + \bar{x}_N^* \end{bmatrix}^T$ for the values of the input $u = 0$ and $u = 1$ when $\beta_2 \neq 0$ or $\beta_2 = 0$. In order to be considered dependable, models must:

- Satisfy the static feature ***S1*** for all conditions: $u = 0$ and $u = 1$ when $\beta_2 \neq 0$ or $\beta_2 = 0$. Namely, $\bar{x}_C + \bar{x}_C^* > 0$ and $\bar{x}_N + \bar{x}_N^* < 1$.

- Satisfy the static feature ***S2***. Namely: $(\bar{x}_N + \bar{x}_N^*)_{u=0,1;\beta_2=0} > (\bar{x}_N + \bar{x}_N^*)_{u=0,1;\beta_2\neq 0}$.

In order to preserve the generality of the analysis, no specific hypotheses will be made on the values of the parameters. In this way the results will be solely dependent on the structure of the models and unaffected by the specific values assumed by the parameters (such as symmetry effects derived by setting the reaction rates to the same value).

The first results are reported in the Tables A.1 and 4.1. Here, I evaluated the equilibrium values and the cytoplasmic and nuclear concentrations at equilibrium for the cases when $u = 0$ and $u = 1$ when $\beta_2 \neq 0$. This case corresponds to the general case of growth and Torin 1 (or starvation) treatments in the absence of Leptomycin B administration. In the tables it is possible to observe that Models 1, 3, 9 and 11 (represented in red in Tables A.1 and 4.1) are not able to satisfy the static feature ***S1***, according to the condition I defined above. Consequently, these models were excluded from the analysis. In addition, I also

Models	$u = 1$	$u = 0$
Classic model	$[0 \quad 1]^T$	$[1 \quad 0]^T$
Model 1	$[0 \quad 1]^T$	$[0 \quad 1]^T$
Model 2	$\left[\frac{\beta_{-1}}{\beta_1+\beta_{-1}} \quad \frac{\beta_1}{\beta_1+\beta_{-1}}\right]^T$	$\left[\frac{\beta_{-2}k_1+\beta_{-1}k_{-1}}{A} \quad \frac{\beta_1 k_{-1}}{A}\right]^T$
Model 3	$[0 \quad 1]^T$	$[0 \quad 1]^T$
Model 4	$\left[\frac{\beta_{-1}}{\beta_1+\beta_{-1}} \quad \frac{\beta_1}{\beta_1+\beta_{-1}}\right]^T$	$\left[\frac{\beta_2\beta_{-1}k_1+\beta_2\beta_{-1}k_{-1}}{B} \quad \frac{\beta_1\beta_2k_{-1}+\beta_{-1}\beta_{-2}k_1}{B}\right]^T$
Model 5	$\left[\frac{\beta_1\beta_2k_2+\beta_2k_2k_{-1}}{C} \quad \frac{\beta_1\beta_2k_{-1}+\beta_1k_2k_{-1}}{C}\right]^T$	$\left[\frac{\beta_1\beta_2k_2+\beta_2k_1k_2+\beta_2k_2k_{-1}}{D} \quad \frac{\beta_1\beta_2k_{-1}+\beta_1k_2k_{-1}}{D}\right]^T$
Model 6	$\left[\frac{\beta_1\beta_2k_2+\beta_2\beta_{-1}k_{-1}+\beta_2k_2k_{-1}}{E} \quad \frac{\beta_1\beta_2k_{-1}+\beta_1k_2k_{-1}}{E}\right]^T$	$\left[\frac{\beta_1\beta_2k_2+\beta_2\beta_{-1}k_1+\beta_2\beta_{-1}k_{-1}+\beta_2k_2k_2+\beta_2k_2k_{-1}}{F} \quad \frac{\beta_1\beta_2k_{-1}+\beta_1k_2k_{-1}}{F}\right]^T$
Model 7	$\left[\frac{\beta_1\beta_2k_2+\beta_2k_2k_{-1}}{G} \quad \frac{\beta_1\beta_2k_{-1}+\beta_1\beta_{-2}k_2+\beta_1k_2k_{-1}}{G}\right]^T$	$\left[\frac{\beta_1\beta_2k_2+\beta_2k_1k_2+\beta_2k_2k_{-1}}{H} \quad \frac{\beta_1\beta_2k_{-1}+\beta_1\beta_{-2}k_2+\beta_{-2}k_1k_2+\beta_1k_2k_{-1}}{H}\right]^T$
Model 8	$\left[\frac{\beta_1\beta_2k_2+\beta_2\beta_{-1}k_{-1}+\beta_2k_2k_{-1}}{I} \quad \frac{\beta_2\beta_2k_{-1}+\beta_1\beta_{-2}k_2+\beta_1k_2k_{-1}}{I}\right]^T$	$\left[\frac{\beta_1\beta_2k_2+\beta_2\beta_{-1}k_1+\beta_2\beta_{-1}k_{-1}+\beta_2k_1k_2+\beta_2k_2k_{-1}}{L} \quad \frac{\beta_1\beta_2k_{-1}+\beta_1\beta_{-2}k_2+\beta_{-1}\beta_{-2}k_1+\beta_{-2}k_1k_2+\beta_1k_2k_{-1}}{L}\right]^T$
Model 9	$[0 \quad 1]^T$	$[0 \quad 1]^T$
Model 10	$\left[\frac{\beta_{-1}}{\beta_1+\beta_{-1}} \quad \frac{\beta_1}{\beta_1+\beta_{-1}}\right]^T$	$\left[\frac{\beta_{-2}k_1+\beta_{-1}k_{-1}}{A} \quad \frac{\beta_1 k_{-1}}{A}\right]^T$
Model 11	$[0 \quad 1]^T$	$[0 \quad 1]^T$
Model 12	$\left[\frac{\beta_{-1}}{\beta_1+\beta_{-1}} \quad \frac{\beta_1}{\beta_1+\beta_{-1}}\right]^T$	$\left[\frac{\beta_2\beta_{-1}k_1+\beta_2\beta_{-1}k_{-1}+\beta_{-1}\beta_{-2}k_{-2}+\beta_{-1}k_1k_{-2}+\beta_{-1}k_{-1}k_{-2}}{M} \quad \frac{\beta_1\beta_2k_{-1}+\beta_1\beta_{-2}k_{-2}+\beta_{-2}k_1k_{-2}+\beta_1k_{-1}k_{-2}+\beta_{-1}\beta_{-2}k_1}{M}\right]^T$

Table 4.1: **Cytoplasmic and Nuclear concentrations at Equilibrium.** The cytoplasmic and nuclear concentrations at equilibrium $\left[\bar{x}_C + \bar{x}_C^* \quad \bar{x}_N + \bar{x}_N^*\right]^T$ for each model have been evaluated for $u = 0$ and $u = 1$. The parameters are independent of each other.

reported the analysis of the Classic Model as proof of concept confirming that is not able to meet the static feature when u is set to 0 or 1.

Then, I evaluated the equilibrium values and the cytoplasmic and nuclear concentrations at equilibrium for the cases when $u = 0$ and $u = 1$ when $\beta_2 = 0$. The results are reported in the Tables A.2 and 4.2. This case corresponds to the growth and Torin 1 (or starvation) treatments under Leptomycin B administration. In the tables it is possible to observe that Models 5, 6, 7 and 8 are not able to satisfy the static feature ***S1***; while the models 2, 4, 10 and 12 satisfy the feature ***S1***, but they are not able to satisfy the static feature ***S2***.

These results confirm once more that the hypothesis that the Leptomycin B treatment completely inhibits the nuclear export of TFEB is not supported by numerical simulations. Indeed, none of the twelve models can meet the static features under this assumption.

At this point, I took advantage of the experimental evidence presented in [62]. Here, they assessed the nuclear export kinetics of TFEB in response to nutrient availability, observing the presence of two different nuclear pools of TFEB that are exported from the nucleus at different rates. In particular, the rates did not change during starvation and refeeding conditions, and they suggest that the two different TFEB pools being exported at different rates may correspond to the phosphorylated and dephosphorylated forms.

Models	$u = 1, \beta_2 = 0$	$u = 0, \beta_2 = 0$
Model 2	$\left[\frac{\beta_{-1}}{\beta_1 + \beta_{-1}} \quad \frac{\beta_1}{\beta_1 + \beta_{-1}}\right]^T$	$\left[\frac{\beta_{-1}k_1 + \beta_{-1}k_{-1}}{A} \quad \frac{\beta_1 k_{-1}}{A}\right]^T$
Model 4	$\left[\frac{\beta_{-1}}{\beta_1 + \beta_{-1}} \quad \frac{\beta_1}{\beta_1 + \beta_{-1}}\right]^T$	$[0 \quad 1]^T$
Model 5	$[0 \quad 1]^T$	$[0 \quad 1]^T$
Model 6	$[0 \quad 1]^T$	$[0 \quad 1]^T$
Model 7	$[0 \quad 1]^T$	$[0 \quad 1]^T$
Model 8	$[0 \quad 1]^T$	$[0 \quad 1]^T$
Model 10	$\left[\frac{\beta_{-1}}{\beta_1 + \beta_{-1}} \quad \frac{\beta_1}{\beta_1 + \beta_{-1}}\right]^T$	$\left[\frac{\beta_{-1}k_1 + \beta_{-1}k_{-1}}{A} \quad \frac{\beta_1 k_{-1}}{A}\right]^T$
Model 12	$\left[\frac{\beta_{-1}}{\beta_1 + \beta_{-1}} \quad \frac{\beta_1}{\beta_1 + \beta_{-1}}\right]^T$	$\left[\frac{\beta_{-1}\beta_{-2}k_{-2} + \beta_{-1}k_1k_{-2} + \beta_{-1}k_{-1}k_{-2}}{N} \quad \frac{\beta_1\beta_{-2}k_{-2} + \beta_{-2}k_1k_{-2} + \beta_1k_{-1}k_{-2} + \beta_{-1}\beta_{-2}k_1}{N}\right]^T$

Table 4.2: **Cytoplasmic and Nuclear concentrations at Equilibrium evaluated in the General Case when $\beta_2 = 0$.** The cytoplasmic and nuclear concentrations at equilibrium $\left[\bar{x}_C + \bar{x}^*_C \quad \bar{x}_N + \bar{x}^*_N\right]^T$ for each model have been evaluated for $u = 0$ and $u = 1$ when $\beta_2 = 0$. The parameters are independent of each other.

Accordingly, I modified the models by considering two additional export rates: one for dephosphorylated nuclear TFEB ($TFEB_{nuc}$), and the other for phosphorylated nuclear TFEB ($TFEB^*_{nuc}$). The two extra reactions can be considered as "passive" in the sense that they always occur during both growth and starvation treatments, and are independent on XPO1, and thus on Leptomycin B administration. In particular, the export rate β_{-1} is already present in the general model and it can be considered as a "passive" export. Indeed, models 2, 4, 6 and 8 are characterized by the presence of β_{-1}. On the other hand, β_2 does not present these features. Consequently, I introduced a new "passive" export $\beta_{2,p}$ that is present in all of the models and that is different from 0 even when Leptomycin B is administered. The new block scheme of the Alternative Models under analysis is proposed in Figure 4.7.

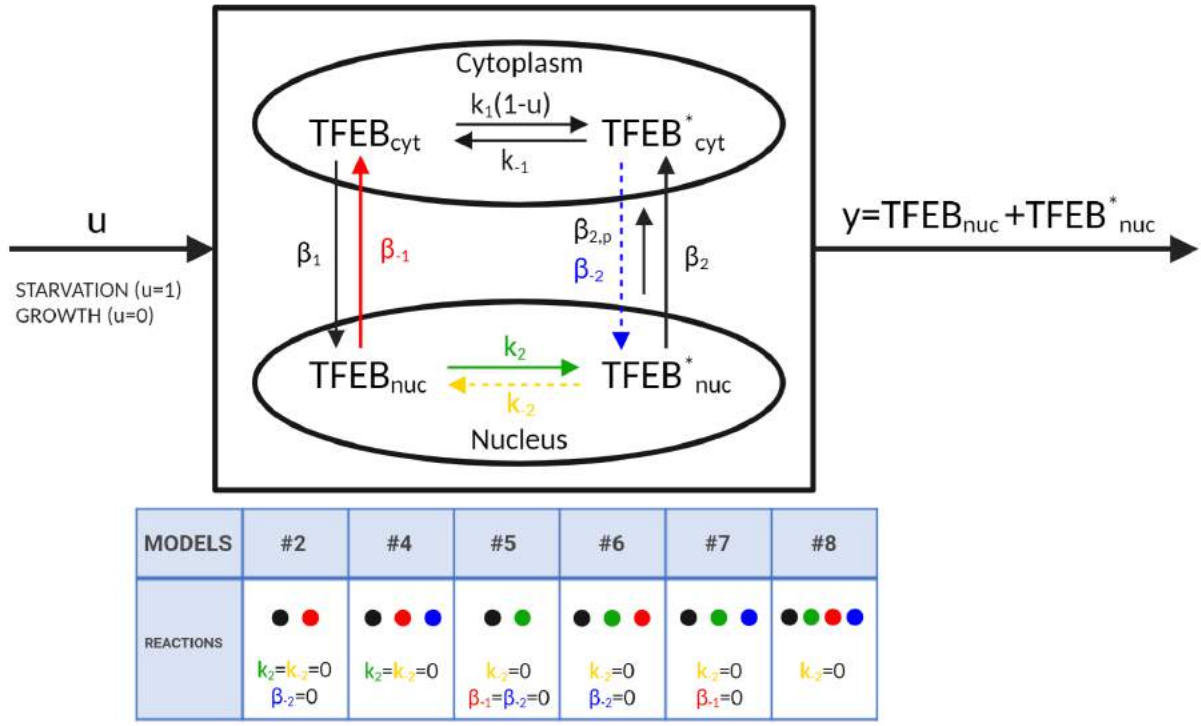

Figure 4.7: **General Block scheme of the Alternative Models proposed to explain the experimental Static Features.** The presence of an export independent of XPO1 is considered to explain the experimental Static Features. Here, the new reaction rate is introduced as the "passive" transport rate $\beta_{2,p}$. The legend on the bottom describes the choice of the parameters for each model. In particular: the colored circles indicate the reactions of each model; then, it is also reported which parameter is set to zero. Other details about the block scheme are reported in Figure 4.6.

Consequentially, the general model equations became:

$$\dot{x}_C^* = k_1(1-u)(1-x_C^*-x_N-x_N^*) - k_{-1}x_C^* + (\beta_2+\beta_{2,p})x_N^* - \beta_{-2}x_C^*$$

$$\dot{x}_N = k_{-2}x_N^* - k_2 x_N + \beta_1(1-x_C^*-x_N-x_N^*) - \beta_{-1}x_N$$

$$\dot{x}_N^* = k_2 x_N - k_{-2}x_N^* + \beta_{-2}x_C^* - (\beta_2+\beta_{2,p})x_N^*$$

Subsequently, I decided to repeat the evaluation of the equilibrium points and the cytoplasmic and nuclear concentrations at equilibrium for the cases when $u = 0$ and $u = 1$ when $\beta_2 = 0$. The results are reported in the Tables A.3 and 4.3. In this case, I decided to exclude from the analysis the models 10 and 12 (represented in red in Tables A.2 and 4.2). Indeed, as previously commented, they are mainly characterized by a nuclear dephosphorylation. This type of reaction was never observed experimentally nor reported in literature. In addition, all models characterized by nuclear dephosphorylation (models 9 to 12) showed

Models	$u = 1, \beta_2 = 0$	$u = 0, \beta_2 = 0$
Model 2	$\left[\frac{\beta_{-1}}{\beta_1+\beta_{-1}} \quad \frac{\beta_1}{\beta_1+\beta_{-1}}\right]^T$	$\left[\frac{\beta_{-1}k_1+\beta_{-1}k_{-1}}{A} \quad \frac{\beta_1 k_{-1}}{A}\right]^T$
Model 4	$\left[\frac{\beta_{-1}}{\beta_1+\beta_{-1}} \quad \frac{\beta_1}{\beta_1+\beta_{-1}}\right]^T$	$\left[\frac{\beta_{2,p}\beta_{-1}k_1+\beta_{2,p}\beta_{-1}k_{-1}}{B^*} \quad \frac{\beta_1\beta_{2,p}k_{-1}+\beta_{-1}\beta_{-2}k_1}{B^*}\right]^T$
Model 5	$\left[\frac{\beta_1\beta_{2,p}k_2+\beta_{2,p}k_2k_{-1}}{C^*} \quad \frac{\beta_1\beta_{2,p}k_{-1}+\beta_1k_2k_{-1}}{C^*}\right]^T$	$\left[\frac{\beta_1\beta_{2,p}k_2+\beta_{2,p}k_1k_2+\beta_{2,p}k_2k_{-1}}{D^*} \quad \frac{\beta_1\beta_{2,p}k_{-1}+\beta_1k_2k_{-1}}{D^*}\right]^T$
Model 6	$\left[\frac{\beta_1\beta_{2,p}k_2+\beta_{2,p}\beta_{-1}k_{-1}+\beta_2k_2k_{-1}}{E^*} \quad \frac{\beta_1\beta_{2,p}k_{-1}+\beta_1k_2k_{-1}}{E^*}\right]^T$	$\left[\frac{\beta_1\beta_{2,p}k_2+\beta_{2,p}\beta_{-1}k_1+\beta_{2,p}\beta_{-1}k_{-1}+\beta_{2,p}k_1k_2+\beta_{2,p}k_2k_{-1}}{F^*} \quad \frac{\beta_1\beta_2k_{-1}+\beta_1k_2k_{-1}}{F^*}\right]^T$
Model 7	$\left[\frac{\beta_1\beta_{2,p}k_2+\beta_{2,p}k_2k_{-1}}{G^*} \quad \frac{\beta_1\beta_{2,p}k_{-1}+\beta_1\beta_{-2}k_2+\beta_1k_2k_{-1}}{G^*}\right]^T$	$\left[\frac{\beta_1\beta_{2,p}k_2+\beta_{2,p}k_1k_2+\beta_{2,p}k_2k_{-1}}{H^*} \quad \frac{\beta_1\beta_{2,p}k_{-1}+\beta_1\beta_{-2}k_2+\beta_{-2}k_1k_2+\beta_1k_2k_{-1}}{H^*}\right]^T$
Model 8	$\left[\frac{\beta_1\beta_{2,p}k_2+\beta_{2,p}\beta_{-1}k_{-1}+\beta_{2,p}k_2k_{-1}}{I^*} \quad \frac{\beta_1\beta_{2,p}k_{-1}+\beta_1\beta_{-2}k_2+\beta_1k_2k_{-1}}{I^*}\right]^T$	$\left[\frac{\beta_1\beta_{2,p}k_2+\beta_{2,p}\beta_{-1}k_1+\beta_{2,p}\beta_{-1}k_{-1}+\beta_{2,p}k_1k_2+\beta_{2,p}k_2k_{-1}}{L^*} \quad \frac{\beta_1\beta_{2,p}k_{-1}+\beta_1\beta_{-2}k_2+\beta_{-1}\beta_{-2}k_1+\beta_{-2}k_1k_2+\beta_1k_2k_{-1}}{L^*}\right]^T$

Table 4.3: **Cytoplasmic and Nuclear concentrations at Equilibrium evaluated in the General Case, when $\beta_2 = 0$ in the presence of $\beta_{2,p}$.** The cytoplasmic and nuclear concentrations at equilibrium $\begin{bmatrix}\bar{x}_C + \bar{x}_C^* & \bar{x}_N + \bar{x}_N^*\end{bmatrix}^T$ for each model have been evaluated for $u = 0$ and $u = 1$ when $\beta_2 = 0$ in the presence of $\beta_{2,p}$. The parameters are independent of each other.

limits in the proposed equilibrium analysis, suggesting that the potential existence of such a reaction in the biological network under study is not relevant. Therefore, the following analysis will investigate the impact of nuclear phosphorylation on the properties of the models at the equilibrium.

Looking at the results reported in the Tables A.3 and 4.3, it is possible to observe that, again, models 2 and 4 satisfy the feature ***S1***; conversely, they are not able to satisfy the static feature ***S2*** (they are represented in red in Tables A.3 and 4.3). Indeed, the equilibrium points of these models for $u = 0$ and $u = 1$ are the same for $\beta_2 \neq 0$ and $\beta_2 = 0$, i.e. they are insensitive to Leptomycin B treatment suggesting an intrinsic limitation of the models structure. Consequently, the two models were excluded from the subsequent analysis. For completeness, it is necessary to know that models 10 and 12 behave as the modes 2 and 4 (not showed), confirming that the action of the nuclear dephosphorylation is not relevant in this analysis.

Models 5, 6, 7 and 8 now satisfy the static feature ***S1*** as a consequence of the new export reaction assumption. In addition, they turn out to be able to satisfy also the static feature ***S2***. In order to confirm this numerically, I decided to evaluate the equilibrium points of these models for specific values of the parameters, that will be also useful for the following analysis in dynamic, described in the next Subsection.

I assumed the de/phosphorylation rates all equal to the parameter k. The transport

Models	$u = 1$	$u = 0$
Model 5	$\left[\frac{1}{2} \quad \frac{1}{2}\right]^T$	$\left[\frac{\beta + 2k}{2\beta + 3k} \quad \frac{\beta + k}{2\beta + 3k}\right]^T$
Model 6	$\left[\frac{11\beta + 10k}{21\beta + 20k} \quad \frac{10\beta + 10k}{21\beta + 20k}\right]^T$	$\left[\frac{6\beta + 10k}{11\beta + 15k} \quad \frac{5\beta + 5k}{11\beta + 15k}\right]^T$
Model 7	$\left[\frac{10\beta + 10k}{21\beta + 20k} \quad \frac{11\beta + 10k}{21\beta + 20k}\right]^T$	$\left[\frac{10\beta + 20k}{21\beta + 31k} \quad \frac{11\beta + 11k}{21\beta + 31k}\right]^T$
Model 8	$\left[\frac{5\beta}{11\beta + 10k} \quad \frac{6\beta + 10k}{11\beta + 10k}\right]^T$	$\left[\frac{120\beta + 200k}{231\beta + 310k} \quad \frac{111\beta + 110k}{231\beta + 310k}\right]^T$

Table 4.4: **Cytoplasmic and Nuclear concentrations at Equilibrium evaluated in the Case of dependence on k and β in the presence of $\beta_{2,p}$.** The cytoplasmic and nuclear concentrations at equilibrium $\left[\bar{x}_C + \bar{x}_C^* \quad \bar{x}_N + \bar{x}_N^*\right]^T$ for each model have been evaluated for $u = 0$ and $u = 1$. The parameters are all dependent on k or β.

rates β_1 and β_2 were set equal to β and $\frac{9\beta}{10}$, respectively. The two "passive" exports β_{-1} and $\beta_{2,p}$ and the transport rate β_{-2} were set equal to $\frac{\beta}{10}$, since they were considered slower as compared to the two "preferential" transports, β_1 and β_2. In particular, the two rates β_2 and $\beta_{2,p}$ were chosen so that the total export of nuclear phosphorylated TFEB is $\beta_{2,tot} = \beta_2 + \beta_{2,p} = \beta$. Overall, the system parameters were reduced to two. The value of two parameters is: $k = \frac{1}{70} = 1.5 \cdot 10^{-2}$, $\beta = \frac{1}{216} = 5 \cdot 10^{-3}$, as described in Subsection 4.2.1. Clearly, the models are distinguished by various structural features, and the legend in Figure 4.7 specifies the parameters set to zero for each.

Once a value has been assigned to each parameter, I repeated the calculation for the models from 5 to 8 in this specific case. In particular, I evaluated the equilibrium values and the cytoplasmic and nuclear concentrations at equilibrium for the cases when $u = 0$ and $u = 1$ when $\beta_2 \neq 0$. The results are reported in Tables A.5 and 4.4. Here, I confirmed that all the models satisfy the static feature ***S1*** for this specific choice of the parameters.

Then, I evaluated the equilibrium values and the cytoplasmic and nuclear concentrations at equilibrium for the cases when $u = 0$ and $u = 1$ when $\beta_2, \beta_{2,p} = 0$ as a proof of concept. The results are reported in Tables A.6 and 4.5. As expected, I confirmed that the models

Models	$u = 1, \beta_2 = 0$	$u = 0, \beta_2 = 0$
Model 5	$[0 \quad 1]^T$	$[0 \quad 1]^T$
Model 6	$[0 \quad 1]^T$	$[0 \quad 1]^T$
Model 7	$[0 \quad 1]^T$	$[0 \quad 1]^T$
Model 8	$[0 \quad 1]^T$	$[0 \quad 1]^T$

Table 4.5: **Cytoplasmic and Nuclear concentrations at Equilibrium evaluated in the Case of dependence on k and β when $\beta_2, \beta_{2,p} = 0$.** The cytoplasmic and nuclear concentrations at equilibrium $\left[\bar{x}_C + \bar{x}_C^* \quad \bar{x}_N + \bar{x}_N^*\right]^T$ for each model have been evaluated for $u = 0$ and $u = 1$ when $\beta_2, \beta_{2,p} = 0$. The parameters are all dependent on k or β.

are not able to satisfy the static feature ***S1*** when the "passive" export on the nuclear phosphorylated TFEB is set to zero.

Consequently, I evaluated the equilibrium values and the cytoplasmic and nuclear concentrations at equilibrium for the cases when $u = 0$ and $u = 1$ when $\beta_2 = 0$ and $\beta_{2,p} = \frac{\beta}{10}$, as assigned above. The results are reported in Tables A.7 and 4.6. They confirm that by introducing the "passive" export $\beta_{2,p}$, the models satisfy the static feature ***S1***.

At this point, to verify if the models were also able to satisfy the static feature ***S2***, I applied the criterion defined at the start of the Subsection: $(\bar{x}_N + \bar{x}_N^*)_{u=0,1;\beta_2=0} > (\bar{x}_N + \bar{x}_N^*)_{u=0,1;\beta_2\neq 0}$. As results, I obtained two inequalities for each model to satisfy, as reported in Table 4.7 on the top. The results of the inequalities are reported on the bottom of the same Table. The outcomes confirm that all the models are able to satisfy ***S2***.

In summary, models from 5 to 8 are able to satisfy the experimental static features previously introduced, under the assumption of the existence of "passive" transports [62]. Notably, the presence of the nuclear phosphorylation reaction characterizes all models able to satisfy the analysis at equilibrium. The findings of this analysis therefore imply that nuclear phosphorylation is a relevant reaction and that it is essential in explaining the experimental data.

Models	$u = 1, \beta_2 = 0$	$u = 0, \beta_2 = 0$
Model 5	$\left[\frac{\beta + k}{2\beta + 11k} \quad \frac{\beta + 10k}{2\beta + 11k}\right]^T$	$\left[\frac{\beta + 7k}{2(\beta + 6k)} \quad \frac{\beta + 5k}{2(\beta + 6k)}\right]^T$
Model 6	$\left[\frac{11\beta + 10k}{21\beta + 110k} \quad \frac{10\beta + 100k}{21\beta + 110k}\right]^T$	$\left[\frac{6\beta + 10k}{11\beta + 60k} \quad \frac{5\beta + 50k}{11\beta + 60k}\right]^T$
Model 7	$\left[\frac{\beta + k}{3\beta + 11k} \quad \frac{2\beta + 10k}{3\beta + 11k}\right]^T$	$\left[\frac{\beta + 2k}{3\beta + 13k} \quad \frac{2\beta + 11k}{3\beta + 13k}\right]^T$
Model 8	$\left[\frac{11\beta + 10k}{31\beta + 110k} \quad \frac{20\beta + 100k}{31\beta + 110k}\right]^T$	$\left[\frac{12\beta + 20k}{33\beta + 130k} \quad \frac{21\beta + 110k}{33\beta + 130k}\right]^T$

Table 4.6: **Cytoplasmic and Nuclear concentrations at Equilibrium evaluated in the Case of dependence on k and β, when $\beta_2 = 0$ in the presence of $\beta_{2,p}$.** The cytoplasmic and nuclear concentrations at equilibrium $\left[\bar{x}_C + \bar{x}_C^* \quad \bar{x}_N + \bar{x}_N^*\right]^T$ for each model have been evaluated for $u = 0$ and $u = 1$ when $\beta_2 = 0$ in the presence of $\beta_{2,p}$. The parameters are all dependent on k or β.

In the following, the models able to satisfy the static features will be further analysed to probe their dynamics. In particular, I will focus on the model 6, which can be considered the best minimal model since it is also consistent with all the literature. Indeed, differently from the other models (5, 7 and 8), it only considers the presence of both "passive" transports β_{-1} and $\beta_{2,p}$, without considering the existence of the import reaction β_{-2}, which has never been reported in literature. In addition, it is able to satisfy ***S2*** for any value of k and β.

4.3.3 Analysis of Dynamic Features

A block scheme of model 6 is reported in Figure 4.8. In this Subsection, the dynamics of the model will be analysed to test its compliance with respect to the experimental data.

The model will be examined by assessing numerical simulations of the cases of interest, namely by simulating experimental stimuli shown in Figure 4.1. To maintain consistency with the analyses in the previous Subsection, the growth condition is simulated by setting the input $u = 0$; the Torin 1 (or starvation) condition by setting $u = 1$; the Leptomycin B treatment by setting the parameter $\beta_2 = 0$. Each input will be simulated as a pulse train of twenty hours, with a period of six hours and a duty cycle of the fifty percent as shown in Figure 4.9.

In addition, in order to verify that the model satisfies all the dynamics features, two

Models	$u = 1$	$u = 0$
Model 5	$\frac{1}{2} < \frac{\beta + 10k}{2\beta + 11k}$	$\frac{\beta + k}{2\beta + 3k} < \frac{\beta + 5k}{2(\beta + 6k)}$
Model 6	$\frac{10\beta + 10k}{21\beta + 20k} < \frac{10\beta + 100k}{21\beta + 110k}$	$\frac{5\beta + 5k}{11\beta + 15k} < \frac{5\beta + 50k}{11\beta + 60k}$
Model 7	$\frac{11\beta + 10k}{21\beta + 20k} < \frac{2\beta + 10k}{3\beta + 11k}$	$\frac{11\beta + 11k}{21\beta + 31k} < \frac{2\beta + 11k}{3\beta + 13k}$
Model 8	$\frac{6\beta + 10k}{11\beta + 10k} < \frac{20\beta + 100k}{31\beta + 110k}$	$\frac{111\beta + 110k}{231\beta + 310k} < \frac{21\beta + 110k}{33\beta + 130k}$

Models	$u = 1$	$u = 0$
Model 5	$\forall\, k > 0, \beta > 0$	$\beta < 3k, k > 0, \beta > 0$
Model 6	$\forall\, k > 0, \beta > 0$	$\forall\, k > 0, \beta > 0$
Model 7	$\forall\, k > 0, \beta > 0$	$\forall\, k > 0, \beta > 0$
Model 8	$\beta > \frac{5k}{17}, k > 0, \beta > 0$	$\forall\, k > 0, \beta > 0$

Table 4.7: **Conditions to satisfy the *S2* Feature.** Above are the conditions to satisfy the *S2* feature. Below, their results.

features of interest will be evaluated for each simulation:

- the Overshoot%: $100\frac{max(signal) - end_{pulse}(signal)}{max(signal)}$, which is the percentage evaluated as the difference between the signal peak $max(signal)$ and the signal value at the end of treatment $end_{pulse}(signal)$ before switching to growth, and then normalized on the peak itself.

- the ratio (in absolute value) between the Fall and the Rise rates of TFEB nuclear signal upon switching treatment during the pulse: $|\frac{Fall_{rate}}{Rise_{rate}}|$.

The values of these two quantities will be evaluated on the second pulse of each simulation in a wide range of conditions, where changing the two parameters k and β between -90% and $+90\%$ around their nominal values $k = \frac{1}{70}$ and $\beta = \frac{1}{216}$.

The results of the simulations of the Model 6 reported in Figures 4.9 A, B and C confirm that the model satisfies the two static features ***S1*** and ***S2***. Figure 4.9 C also shows that the Model 6 satisfies the dynamic feature ***D2***. In addition, Figures 4.9 G and H prove that

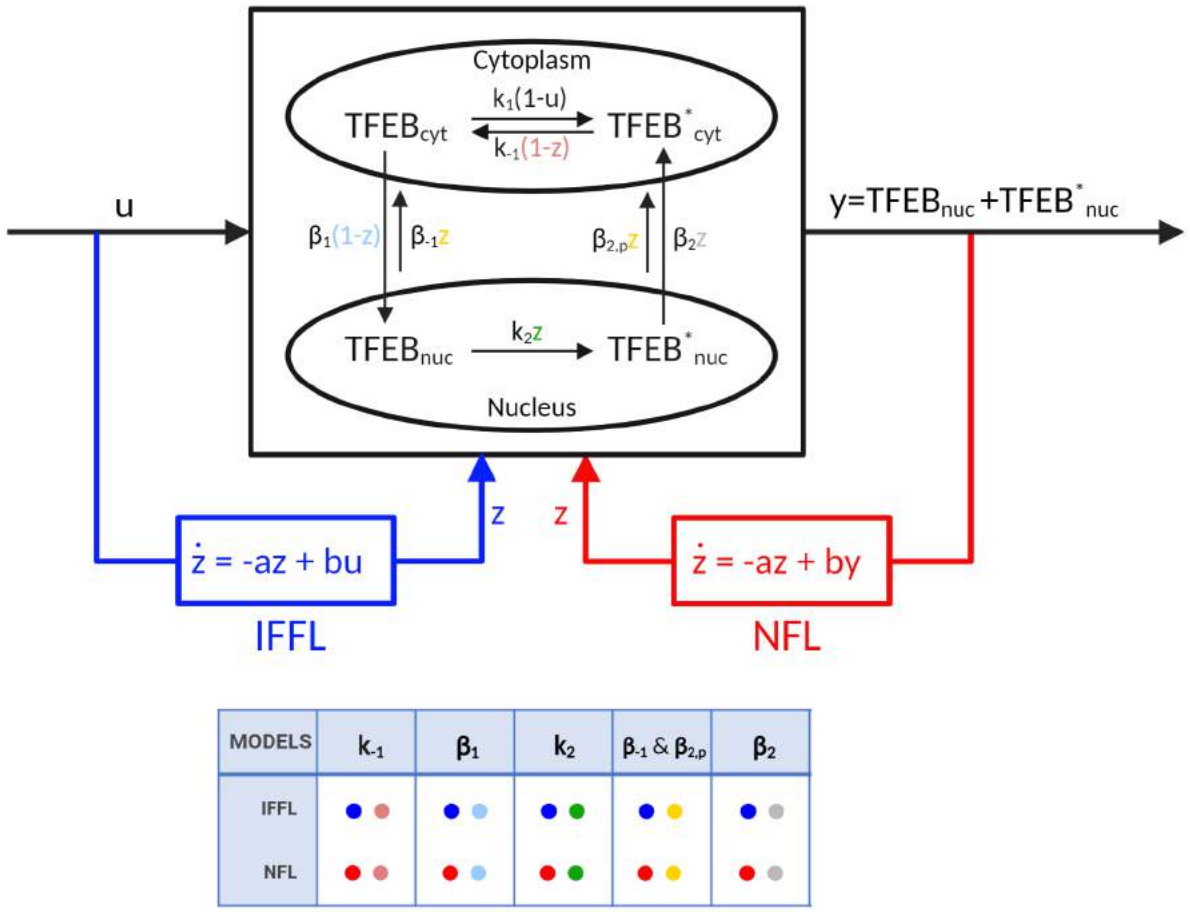

Figure 4.8: **General Block scheme of the Alternative IFFL and NFL Models proposed.** The block scheme of Model 6 is reported in black. The block scheme of the negative feedback regulation hypothesised for the overshoot dynamics is represented in red. The production of the new species z depends on the total amount of nuclear TFEB y. Block scheme of the incoherent feedforward regulation hypothesised for the overshoot dynamics is represented in blue. The production of the new species z depends on the input u. The legend on the bottom describes the choice of the parameters for each model. In particular, the colored circles indicate the reactions rates of each model.

the model is also able to satisfy the dynamic feature ***D3***. Conversely, it is clearly evident from panels A, B, D and E that the model is not able to satisfy the dynamic feature ***D1***. Indeed, despite the model can replicate the fast dynamics observed in the experiments during medium switches, it is not able to recapitulate the overshoot.

According to the results discussed in the Section 4.2, this result was expected. So, I now propose a similar hypothesis to enhance model performance and to explain the biological outcomes.

In particular, just as it was done for the Classic Model, it is also plausible to infer for Model 6 the existence of an unidentified species that may regulate TFEB nuclear amount

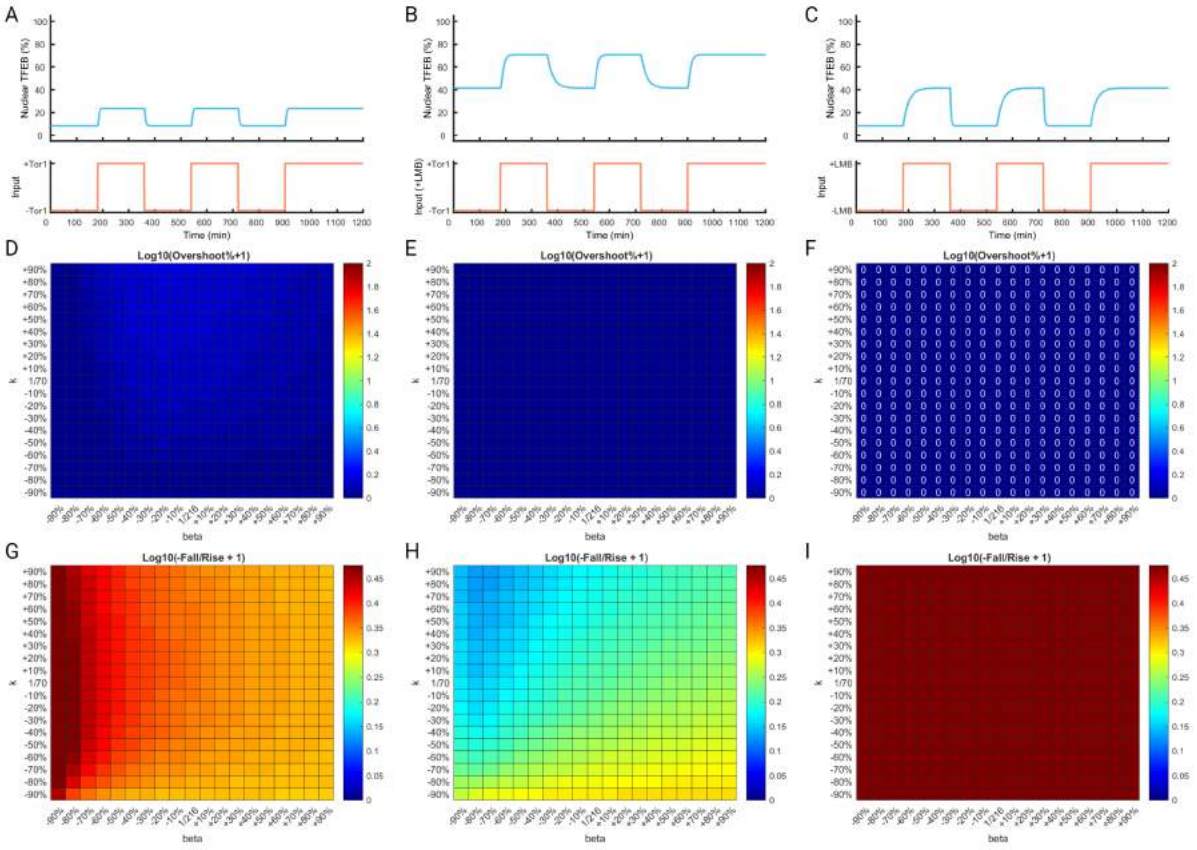

Figure 4.9: **Numerical Simulations of TFEB translocation for the Model 6.** Simulations of TFEB translocation following a pulse train of Torin 1 (A), Torin 1 supplied with Leptomycin B (B), Leptomycin B (C). Heatmaps of Overshoot% in log10 scale following a pulse train of Torin 1 (D), Torin 1 supplied with Leptomycin B (E), Leptomycin B (F). Heatmaps of Fall over Rise rates ratio in log10 scale following a pulse train of Torin 1 (G), Torin 1 supplied with Leptomycin B (H), Leptomycin B (I). The input is $u = 0$ for the growth condition, and $u = 1$ for the starvation condition. In each heatmap, the de/phosphorylation rate k and the transport rate β are varied between -90% and $+90\%$ of their nominal values $k = \frac{1}{70}$ and $\beta = \frac{1}{216}$.

by either an IFFL or an NFL regulatory motif. Model 6 equations can thus be modified in accordance with the preceding example. Specifically, the first three model equations are the same as the ones reported in the Subsection 4.3.2, where $k_{-2}, \beta_{-2} = 0$ for Model 6. In addition, there is a fourth equation which describes the dynamics of the new species z. For the NFL model, the equation is:

$$\dot{z} = -az + b(x_N + x_N^*)$$

Instead, for the IFFL model, the equation is:

$$\dot{z} = -az + bu$$

In both cases, a and b are respectively the degradation and the production rates of z. The choice of their value was explained in Subsection 4.2.4. Accordingly, the parameters were set again to: $a = 1.5 \cdot 10^{-4}$, $b = 8.8 \cdot 10^{-5}$.

Of interest, it remains to be understood where the new species acts. In the Subsection 4.2.4, I assumed that the species could influence TFEB nuclear transport. Nevertheless, to maintain the generality and the robustness of the analysis, this time I decided to consider any possible case. This implies that the unknown species z could either act on cytoplasmic dephosphorylation rate k_{-1}, cytoplasmic dephosphorylated TFEB import rate β_1, nuclear phosphorylation k_2 or "passive" exports β_{-1} and $\beta_{2,p}$. It is also clear that z cannot act on the cytoplasmic phosphorylation k_1, given the experimental evidence reported in Figure 4.4 A as already discussed in Subsection 4.2.4. Moreover, z cannot act on the XPO1-dependent nuclear export β_2, since the overshoot dynamic is still present when cells are treated with Torin 1 (or starvation) under XPO1 inhibition via Leptomycin B, as reported in Figures 4.1 B and D. Even so, this last case will be also considered in the study as a negative control.

The influence of z on each rate is assumed to be linear and will be evaluated separately in different models. Overall, considering that z can act either through an NFL or an IFFL mechanism on each rate, I generated ten different models. Their block schemes are reported in Figure 4.8.

The semi-quantitative analysis consisting of time-course simulations and heatmaps performed for the original Model 6 will be repeated for each new model to assess its performance and ability in satisfying the dynamic features. Since all the models derive from Model 6, the static features will be satisfied for each of them, as verified in Figures 4.10, 4.11 and A.1 - A.8.

The IFFL on the cytoplasmic dephosphorylation rate k_{-1} and on the cytoplasmic dephosphorylated TFEB import rate β_1 Models are reported in Figures 4.10 and 4.11. These models behave in a similar way. The models satisfy the dynamic feature ***D1***, as

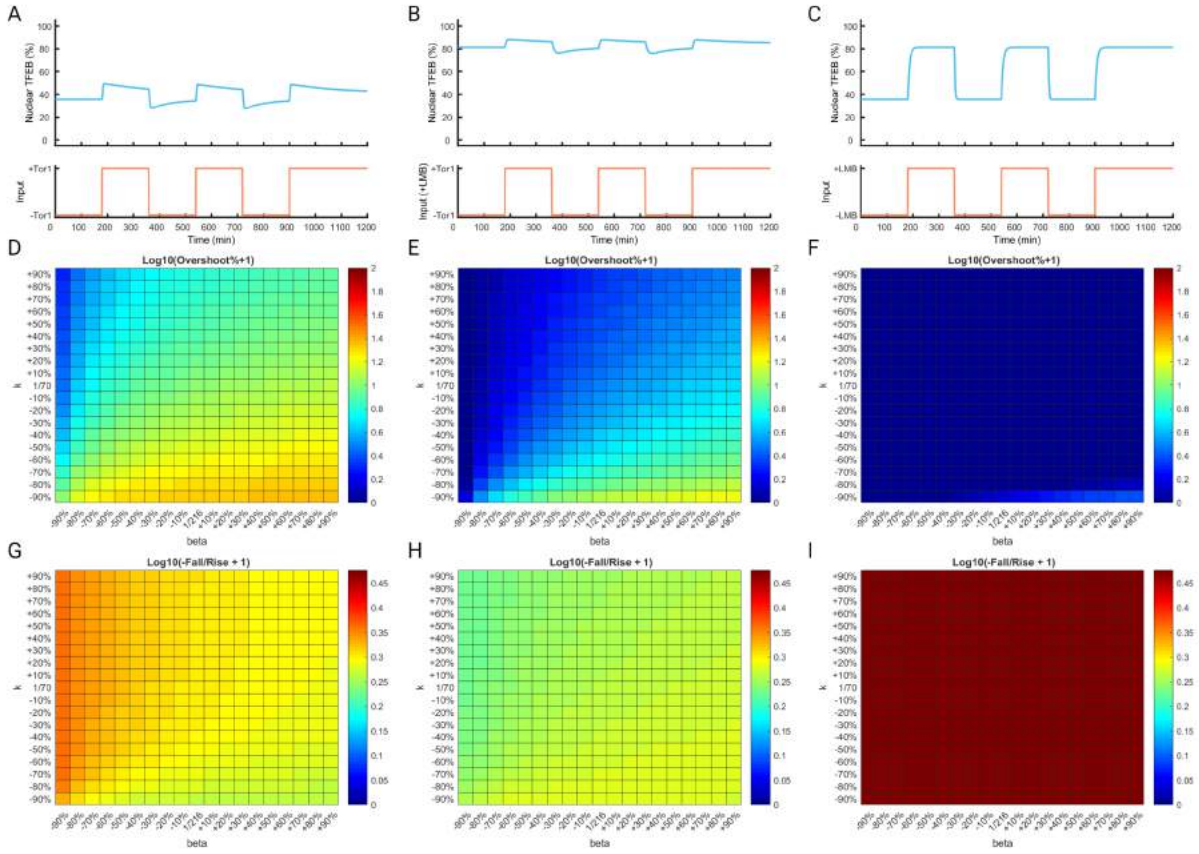

Figure 4.10: **Numerical Simulations of TFEB translocation for the IFFL on k_{-1} Model.** Simulations of TFEB translocation following a pulse train of Torin 1 (A), Torin 1 supplied with Leptomycin B (B), Leptomycin B (C). Heatmaps of Overshoot% in log10 scale following a pulse train of Torin 1 (D), Torin 1 supplied with Leptomycin B (E), Leptomycin B (F). Heatmaps of Fall over Rise rates ratio in log10 scale following a pulse train of Torin 1 (G), Torin 1 supplied with Leptomycin B (H), Leptomycin B (I). The input is $u = 0$ for the growth condition, and $u = 1$ for the starvation condition. In each heatmap, the de/phosphorylation rate k and the transport rate β are varied between -90% and $+90\%$ of their nominal values $k = \frac{1}{70}$ and $\beta = \frac{1}{216}$.

observed in panels A, B, D and E. Even though, the Overshoot% is much lower in the Torin 1 pulse supplied with Leptomycin B experiment simulation than in the Torin 1 pulse experiment simulation for both. The models also satisfy the dynamic feature ***D2***, as described in panels C and F. In addition, by comparing the results presented in panels G and H, the models are also able to satisfy the dynamic feature ***D3***. However, in the IFFL on β_1 Model, the Fall over Rise rates ratio in panels G and H are almost similar in the two experimental simulations and their difference is minimal. Overall, both the models are able to satisfy all the static and the dynamic features and are two good candidates to explain the biological mechanism underlying the experimental dynamics. Interestingly, these are the only two models able to satisfy all the experimentally derived static and

dynamic features.

The NFL on the cytoplasmic dephosphorylation rate k_{-1}, on the cytoplasmic dephosphorylated TFEB import rate β_1 and on the "passive" exports β_{-1} and $\beta_{2,p}$ Models are reported in Figures A.1, A.2 and A.6, respectively. These models behave in similar way and will be commented together. The models are not able to satisfy the dynamic feature ***D1***, as observed in panels A, B, D and E. Indeed, the Overshoot% is really low for all the cases considered. In addition, the models also fail to satisfy the dynamic feature ***D2***, as described in panels C and F, as the overshoot dynamic is still present. This outcome was expect according to the results of the Classic NFL Model discussed in Subsection 4.2.5. By comparing the results presented in panels G and H of each model, they satisfy the dynamic feature ***D3***.

The IFFL on the nuclear phosphorylation k_2 Model is reported in Figure A.3. The model barely satisfies the dynamic feature ***D1***, as observed in panels A, B, D and E, even though, the Overshoot% is almost zero in the Torin 1 pulse supplied with Leptomycin B experiment simulation (B and E) and is lower than in the Torin 1 pulse experiment simulation (A and D). Another limitation is observed in the Torin 1 pulse experiment simulation evaluated for $k = \frac{1}{70}$ and $\beta = \frac{1}{216}$, in panel A. Here, the equilibrium point in growth condition is higher than the one under Torin 1 (or starvation) treatment. In addition, the model fails to recapitulate the dynamics of the Leptomycin B pulse experiment simulation. Consequently, it is not able to satisfy the dynamic feature ***D2***, as described in panels C and F. By comparing the results presented in panels G and H, the model satisfies the dynamic feature ***D3***.

The NFL on the nuclear phosphorylation k_2 Model is reported in Figure A.4. The model is not barely able to satisfy the dynamic feature ***D1***, as observed in panels A, B, D and E. Indeed, the Overshoot% is really low for the cases considered, especially in the Torin 1 pulse supplied with Leptomycin B experiment simulation (B and E), where it is almost zero. The model satisfies the dynamic feature ***D2***, as described in panels C and F. Here, the overshoot dynamic is not present anymore; however, the translocation dynamic during the growth phase is not first-order, as observed in panel C. By comparing the results presented in panels G and H, the model satisfies the dynamic feature ***D3***.

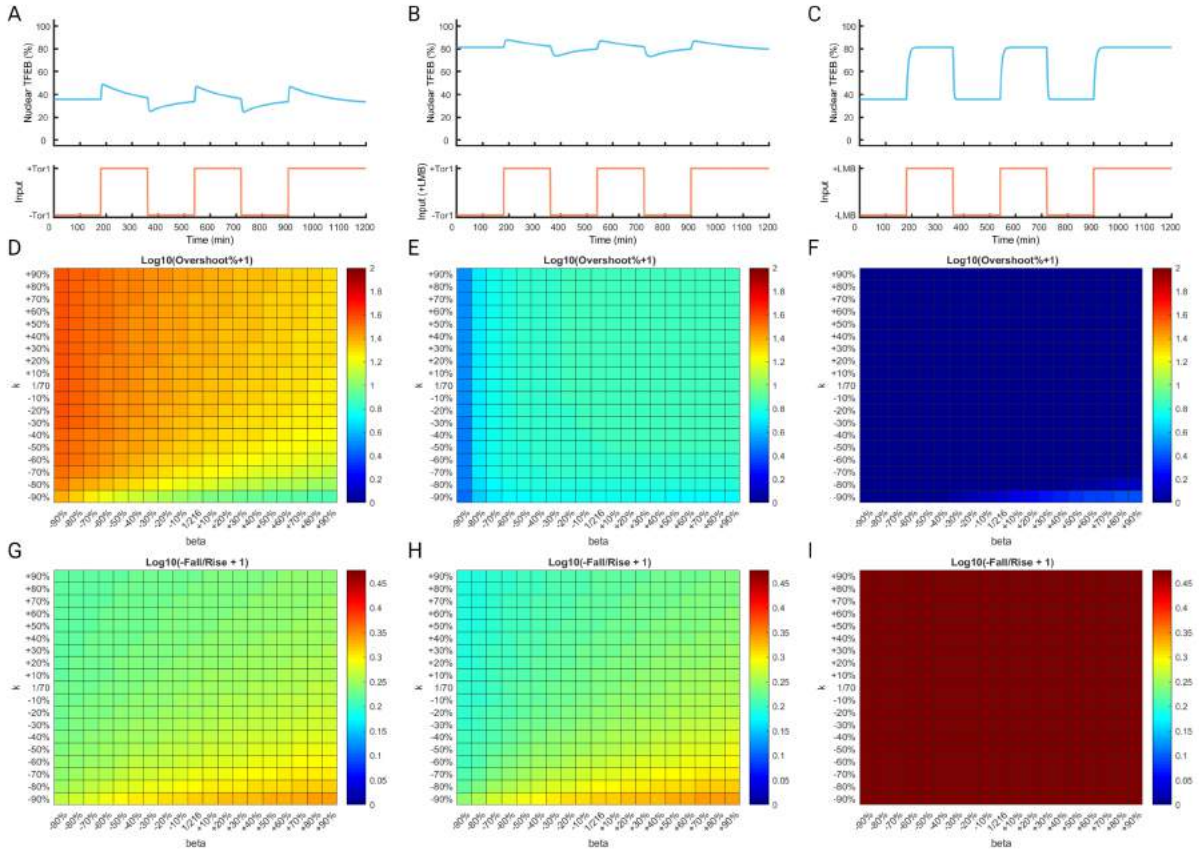

Figure 4.11: **Numerical Simulations of TFEB translocation for the IFFL on β_1 Model.** Simulations of TFEB translocation following a pulse train of Torin 1 (A), Torin 1 supplied with Leptomycin B (B), Leptomycin B (C). Heatmaps of Overshoot% in log10 scale following a pulse train of Torin 1 (D), Torin 1 supplied with Leptomycin B (E), Leptomycin B (F). Heatmaps of Fall over Rise rates ratio in log10 scale following a pulse train of Torin 1 (G), Torin 1 supplied with Leptomycin B (H), Leptomycin B (I). The input is $u = 0$ for the growth condition, and $u = 1$ for the starvation condition. In each heatmap, the de/phosphorylation rate k and the transport rate β are varied between -90% and $+90\%$ of their nominal values $k = \frac{1}{70}$ and $\beta = \frac{1}{216}$.

The IFFL on the "passive" exports β_{-1} and $\beta_{2,p}$ Model is reported in Figure A.5. The model is not barely able to satisfy the dynamic feature ***D1***, as observed in panels A, B, D and E. Indeed, the Overshoot% is really low for the cases considered. Another problem is present in the Torin 1 pulse supplied with Leptomycin B experiment simulation evaluated for $k = \frac{1}{70}$ and $\beta = \frac{1}{216}$, in panel A. Here, the equilibrium point under growth is higher than the one under Torin 1 (or starvation) treatment. The Model satisfies the dynamic feature ***D2***, as described in panels C and F. On the contrary, by comparing the results presented in panels G and H, the model does not satisfy the dynamic feature ***D3***.

The IFFL and the NFL Models on the nuclear export β_2 are reported in Figures A.7 and A.8, respectively. As previously commented, the models are implausible. As expected,

the models fail to satisfy the dynamic feature ***D1*** under the Torin 1 pulse supplied with Leptomycin B experiment simulation, as the overshoot is almost zero (panels B and D of the Figures). In addition, the IFFL Model fails to recapitulate the dynamics in the Leptomycin B pulse experiment simulation. Consequently, it is not able to satisfy the dynamic feature ***D2***, as described in panels C and F in Figure A.7.

In conclusion, in this Chapter, I proposed a computational analysis to explain the dynamics observed experimentally with the purpose of uncovering the underlying biological mechanism. Although the Classic Models yielded important hints to guide the analysis, they were limited in the choice of the input and lacked generality. Consequently, I proposed a rigorous analysis where I selected the best model able to satisfy all the static and dynamic features directly derived from the experimental data. The main conclusions are listed below:

- By hypothesizing the total inhibition of the nuclear export in the Torin 1 (or starvation) in the presence of Leptomycin B, the models failed to recapitulate the experimental results. Only by assuming the existence of "passive" nuclear export reactions, the models were able to qualitatively recover the real dynamics.

- The models able to satisfy all the static features are characterized by the presence of a nuclear phosphorylation reaction, emphasizing its relevance in this study and in the general mechanism under investigation.

- Only by assuming the existence of a species that can regulate TFEB nuclear levels through an IFFL regulatory motif, it is possible to satisfy all the dynamic features. Additionally, the semi-quantitative study presented shows that this unidentified species should either influence TFEB cytoplasmic dephosphorylation rate or the rate of import of cytoplasmic dephosphorylated TFEB.

Chapter 5

Conclusions and Future Work

The possibility of an IFFL acting on TFEB cytoplasmic dephosphorylation or on the import of cytoplasmically dephosphorylated TFEB was supported by the results I described in the previous Chapter.

Hence, I searched the literature for studies supporting these two hypotheses. Because of the limited experimental characterization of TFEB nuclear import, I was unable to discover any references that may support this hypothesis. On the other hand, TFEB cytoplasmic dephosphorylation has been extensively studied *in vitro*, and I was able to uncover several publications that may back up my findings.

As mentioned in Chapter 1, Calcineurin has been identified as the primary phosphatase involved in TFEB cytoplasmic dephosphorylation and its activation during refeeding is mediated by Ca^{2+} release from lysosomes via the Mucolipin 1 channel (MCOLN1) [56, 57]. Indeed, the authors investigated the interaction between TFEB and Calcineurin by means of calcium chelators and ionophores (Thapsigargin, Ionomycin, ML-SA1, SF-51, Bapta AM) during growth, starvation, and Torin 1 treatments. Relevant among the others is the MCOLN1 agonist SF-51 treatment in growth conditions as shown in Figure 5.1, that is able on its own to promote TFEB nuclear translocation. Surprisingly, it is possible to see that following MCOLN1 activation in Hela cells that are overexpressing the fusion protein TFEB-GFP, TFEB translocates into the nucleus with an overshoot dynamics comparable to what I found in my experiments. This experimental characterisation supports the proposed hypothesis and provides the basis for additional research.

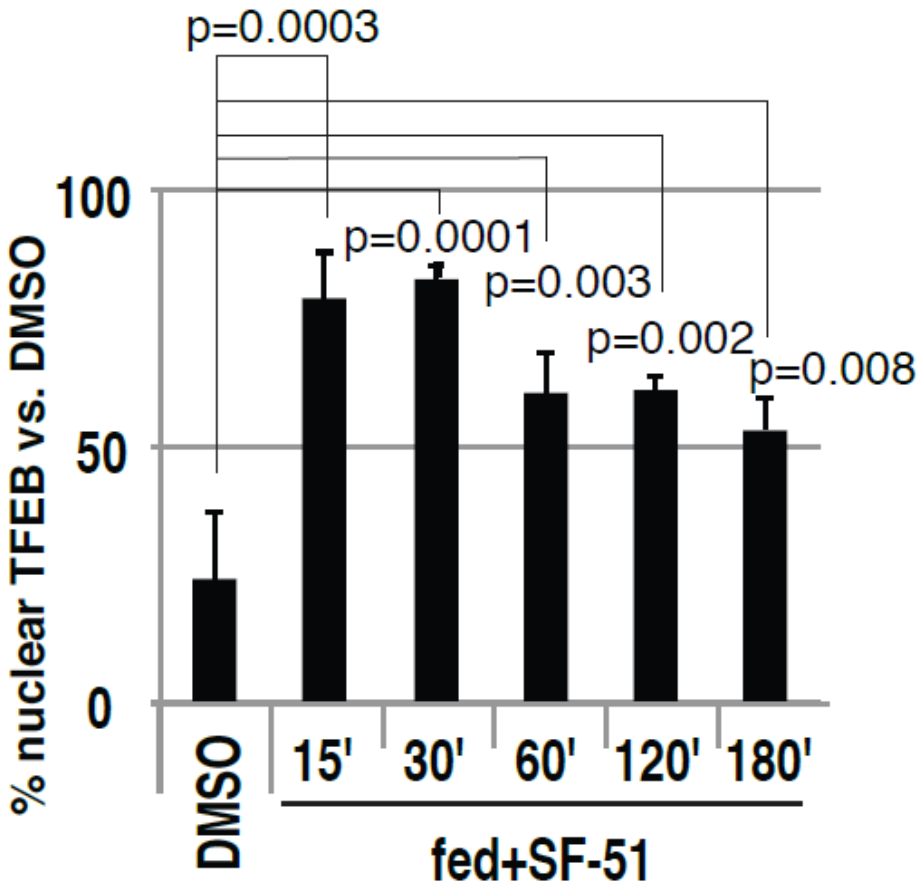

Figure 5.1: **The MCOLN1 agonist SF-51 induces TFEB nuclear translocation.** A high content assay was used to determine, during the time points shown in the figure, how SF-51 administration affected HeLa TFEB-GFP cells. In comparison to DMSO control cells, the graph displays the percentage of treated cells with nuclear TFEB. The graph displays the mean and standard deviation for n=3 separate experiments. Adapted from [56].

Not less crucial, by identifying TFEB as a Calcineurin substrate, the authors in [56] related TFEB with another well characterized substrate, NFAT [32,49]. Indeed, they found that starvation induces Calcineurin-mediated dephosphorylation of both TFEB and NFAT, suggesting a coordinated regulation of the two different transcriptional networks [56].

NFAT transcription factors control gene expression in a number of developmental processes as well as cytokine expression in T cells. The principal NFAT members, NFAT1-4, are phosphorylated and reside in the cytoplasm. They are dephosphorylated by the Calcium-Calmodulin-dependent phosphatase Calcineurin and transported into the nucleus. NFATs are believed to be important antigen signal decoders in T lymphocytes. A careful investigation of the phosphorylation states of NFAT1 revealed that nuclear import and transcriptional activity depend on the dephosphorylation of several serine residues in the

regulatory domain of the inactive protein. Dephosphorylation enhances the exposure of a nuclear localization signal (NLS) and presumably also the masking of a nuclear export signal (NES). Nuclear import through the nuclear pore complex is mediated by the binding of the NLS to the transport machinery, whereas nuclear export is prevented by masking the NES [83].

The surprising similarity between NFAT and TFEB encouraged me to further explore the literature on the former, whose translocation dynamics are well described, in order to provide insights on how to proceed forward with my research. Numerous are the studies that have investigated at the kinetics of NFAT nucleo-cytoplasmic shuttling.

Intriguingly, NFAT1 nuclear translocation dynamics under prolonged antigen stimulation resembled TFEB overshoot dynamics [107]. According to a previous research, antigen stimulation causes a biphasic calcium rise that activates the NFAT pathway [21], supporting the idea that antigen stimulation causes Calcineurin activation to drive NFAT nucleo-cytoplasmic shuttling. An *in silico* study deriving from these findings also confirmed that NFAT was deferentially activated according to duration and amplitude of the Calcium/Calcineurin stimulus (single spike, spike followed by plateau and low-amplitude plateau) [83].

Finally, several other studies investigated the selective activation of NFAT isoforms 1 and 4 by calcium microdomains near CRAC Channels and by nuclear Ca^{2+} [33–35]. Here, authors assessed NFAT calcium-driven translocation by culturing HEK293 cells transfected with NFAT-GFP in a calcium-rich culture medium and treating cells with the SERCA inhibitor Thapsigargin to promote nuclear translocation and subsequently switching to a treatment with the Calcineurin inhibitor Cyclosporin A in a calcium-free medium to promote nuclear export [33–35].

Taken together, these studies highlighted the similarity between the two transcription factors TFEB and NFAT emphasizing the relevance of the calcium-driven Calcineurin signalling in their shuttling dynamics. This research on NFAT translocation dynamics serves as a useful reference for TFEB and provides insightful guidelines for further investigations.

Appendix A

Supplementary Data

Models	$u = 1$	$u = 0$
Classic model	$[0 \quad 1 \quad 0]^T$	$[1 \quad 0 \quad 0]^T$
Model 1	$[0 \quad 1 \quad 0]^T$	$[0 \quad 1 \quad 0]^T$
Model 2	$\left[0 \quad \frac{\beta_1}{\beta_1+\beta_{-1}} \quad 0\right]^T$	$\left[\frac{\beta_{-1}k_1}{A} \quad \frac{\beta_1 k_{-1}}{A} \quad 0\right]^T$
Model 3	$[0 \quad 1 \quad 0]^T$	$[0 \quad 1 \quad 0]^T$
Model 4	$\left[0 \quad \frac{\beta_1}{\beta_1+\beta_{-1}} \quad 0\right]^T$	$\left[\frac{\beta_2\beta_{-1}k_1}{B} \quad \frac{\beta_1\beta_2 k_{-1}}{B} \quad \frac{\beta_{-1}\beta_{-2}k_1}{B}\right]^T$
Model 5	$\left[\frac{\beta_1\beta_2 k_2}{C} \quad \frac{\beta_1\beta_2 k_{-1}}{C} \quad \frac{\beta_1 k_2 k_{-1}}{C}\right]^T$	$\left[\frac{\beta_1\beta_2 k_2+\beta_2 k_1 k_2}{D} \quad \frac{\beta_1\beta_2 k_{-1}}{D} \quad \frac{\beta_1 k_2 k_{-1}}{D}\right]^T$
Model 6	$\left[\frac{\beta_1\beta_2 k_2}{E} \quad \frac{\beta_1\beta_2 k_{-1}}{E} \quad \frac{\beta_1 k_2 k_{-1}}{E}\right]^T$	$\left[\frac{\beta_1\beta_2 k_2+\beta_2\beta_{-1}k_1+\beta_2 k_1 k_2}{F} \quad \frac{\beta_1\beta_2 k_{-1}}{F} \quad \frac{\beta_1 k_2 k_{-1}}{F}\right]^T$
Model 7	$\left[\frac{\beta_1\beta_2 k_2}{G} \quad \frac{\beta_1\beta_2 k_{-1}}{G} \quad \frac{\beta_1 k_2\beta_{-2}+\beta_1 k_2 k_{-1}}{G}\right]^T$	$\left[\frac{\beta_1\beta_2 k_2+\beta_2 k_1 k_2}{H} \quad \frac{\beta_1\beta_2 k_{-1}}{H} \quad \frac{\beta_1\beta_{-2}k_2+\beta_{-2}k_1 k_2+\beta_1 k_2 k_{-1}}{H}\right]^T$
Model 8	$\left[\frac{\beta_1\beta_2 k_2}{I} \quad \frac{\beta_1\beta_2 k_{-1}}{I} \quad \frac{\beta_1 k_2\beta_{-2}+\beta_1 k_2 k_{-1}}{I}\right]^T$	$\left[\frac{\beta_1\beta_2 k_2+\beta_2\beta_{-1}k_1+\beta_2 k_1 k_2}{L} \quad \frac{\beta_1\beta_2 k_{-1}}{L} \quad \frac{\beta_1\beta_{-2}k_2+\beta_{-1}\beta_{-2}k_1+\beta_{-2}k_1 k_2+\beta_1 k_2 k_{-1}}{L}\right]^T$
Model 9	$[0 \quad 1 \quad 0]^T$	$[0 \quad 1 \quad 0]^T$
Model 10	$\left[0 \quad \frac{\beta_1}{\beta_1+\beta_{-1}} \quad 0\right]^T$	$\left[\frac{\beta_{-1}k_1}{A} \quad \frac{\beta_1 k_{-1}}{A} \quad 0\right]^T$
Model 11	$[0 \quad 1 \quad 0]^T$	$[0 \quad 1 \quad 0]^T$
Model 12	$\left[0 \quad \frac{\beta_1}{\beta_1+\beta_{-1}} \quad 0\right]^T$	$\left[\frac{\beta_2\beta_{-1}k_1+\beta_{-1}k_1 k_{-2}}{M} \quad \frac{\beta_1\beta_2 k_{-1}+\beta_1\beta_{-2}k_{-2}+\beta_{-2}k_1 k_{-2}+\beta_1 k_{-1}k_{-2}}{M} \quad \frac{\beta_{-1}\beta_{-2}k_1}{M}\right]^T$

Table A.1: **Equilibrium Points evaluated in the General Case.** The equilibrium points $\left[\bar{x}_C^* \quad \bar{x}_N \quad \bar{x}_N^*\right]^T$ for each model have been evaluated for $u = 0$ and $u = 1$. The parameters are independent of each other.

Models	$u = 1, \beta_2 = 0$	$u = 0, \beta_2 = 0$
Model 2	$\left[0 \quad \frac{\beta_1}{\beta_1 + \beta_{-1}} \quad 0\right]^T$	$\left[\frac{\beta_{-1}k_1}{A} \quad \frac{\beta_1 k_{-1}}{A} \quad 0\right]^T$
Model 4	$\left[0 \quad \frac{\beta_1}{\beta_1 + \beta_{-1}} \quad 0\right]^T$	$[0 \quad 0 \quad 1]^T$
Model 5	$[0 \quad 0 \quad 1]^T$	$[0 \quad 0 \quad 1]^T$
Model 6	$[0 \quad 0 \quad 1]^T$	$[0 \quad 0 \quad 1]^T$
Model 7	$[0 \quad 0 \quad 1]^T$	$[0 \quad 0 \quad 1]^T$
Model 8	$[0 \quad 0 \quad 1]^T$	$[0 \quad 0 \quad 1]^T$
Model 10	$\left[0 \quad \frac{\beta_1}{\beta_1 + \beta_{-1}} \quad 0\right]^T$	$\left[\frac{\beta_{-1}k_1}{A} \quad \frac{\beta_1 k_{-1}}{A} \quad 0\right]^T$
Model 12	$\left[0 \quad \frac{\beta_1}{\beta_1 + \beta_{-1}} \quad 0\right]^T$	$\left[\frac{\beta_{-1}k_1k_{-2}}{N} \quad \frac{\beta_1\beta_{-2}k_{-2} + \beta_{-2}k_1k_{-2} + \beta_1k_{-1}k_{-2}}{N} \quad \frac{\beta_{-1}\beta_{-2}k_1}{N}\right]^T$

Table A.2: **Equilibrium Points evaluated in the General Case when $\beta_2 = 0$.** The equilibrium points $\left[\bar{x}_C^* \quad \bar{x}_N \quad \bar{x}_N^*\right]^T$ for each model have been evaluated for $u = 0$ and $u = 1$ when $\beta_2 = 0$. The parameters are independent of each other.

Models	$u = 1, \beta_2 = 0$	$u = 0, \beta_2 = 0$
Model 2	$\left[0 \quad \frac{\beta_1}{\beta_1 + \beta_{-1}} \quad 0\right]^T$	$\left[\frac{\beta_{-1}k_1}{A} \quad \frac{\beta_1 k_{-1}}{A} \quad 0\right]^T$
Model 4	$\left[0 \quad \frac{\beta_1}{\beta_1 + \beta_{-1}} \quad 0\right]^T$	$\left[\frac{\beta_{2,p}\beta_{-1}k_1}{B^*} \quad \frac{\beta_1\beta_{2,p}k_{-1}}{B^*} \quad \frac{\beta_{-1}\beta_{-2}k_1}{B^*}\right]^T$
Model 5	$\left[\frac{\beta_1\beta_{2,p}k_2}{C^*} \quad \frac{\beta_1\beta_{2,p}k_{-1}}{C^*} \quad \frac{\beta_1k_2k_{-1}}{C^*}\right]^T$	$\left[\frac{\beta_1\beta_{2,p}k_2 + \beta_2k_1k_2}{D^*} \quad \frac{\beta_1\beta_{2,p}k_{-1}}{D^*} \quad \frac{\beta_1k_2k_{-1}}{D^*}\right]^T$
Model 6	$\left[\frac{\beta_1\beta_{2,p}k_2}{E^*} \quad \frac{\beta_1\beta_{2,p}k_{-1}}{E^*} \quad \frac{\beta_1k_2k_{-1}}{E^*}\right]^T$	$\left[\frac{\beta_1\beta_{2,p}k_2 + \beta_{2,p}\beta_{-1}k_1 + \beta_{2,p}k_1k_2}{F^*} \quad \frac{\beta_1\beta_{2,p}k_{-1}}{F^*} \quad \frac{\beta_1k_2k_{-1}}{F^*}\right]^T$
Model 7	$\left[\frac{\beta_1\beta_{2,p}k_2}{G^*} \quad \frac{\beta_1\beta_{2,p}k_{-1}}{G^*} \quad \frac{\beta_1k_2\beta_{-2} + \beta_1k_2k_{-1}}{G^*}\right]^T$	$\left[\frac{\beta_1\beta_{2,p}k_2 + \beta_{2,p}k_1k_2}{H^*} \quad \frac{\beta_1\beta_{2,p}k_{-1}}{H^*} \quad \frac{\beta_1\beta_{-2}k_2 + \beta_{-2}k_1k_2 + \beta_1k_2k_{-1}}{H^*}\right]^T$
Model 8	$\left[\frac{\beta_1\beta_{2,p}k_2}{I^*} \quad \frac{\beta_1\beta_{2,p}k_{-1}}{I^*} \quad \frac{\beta_1k_2\beta_{-2} + \beta_1k_2k_{-1}}{I^*}\right]^T$	$\left[\frac{\beta_1\beta_{2,p}k_2 + \beta_{2,p}\beta_{-1}k_1 + \beta_{2,p}k_1k_2}{L^*} \quad \frac{\beta_1\beta_{2,p}k_{-1}}{L^*} \quad \frac{\beta_1\beta_{-2}k_2 + \beta_{-1}\beta_{-2}k_1 + \beta_{-2}k_1k_2 + \beta_1k_2k_{-1}}{L^*}\right]^T$

Table A.3: **Equilibrium Points evaluated in the General Case, when $\beta_2 = 0$ in the presence of $\beta_{2,p}$.** The equilibrium points $\left[\bar{x}_C^* \quad \bar{x}_N \quad \bar{x}_N^*\right]^T$ for each model have been evaluated for $u = 0$ and $u = 1$ when $\beta_2 = 0$ in the presence of $\beta_{2,p}$. The parameters are independent of each other.

A	$\beta_{-1}k_1 + \beta_1 k_{-1} + \beta_{-1}k_{-1}$
B	$\beta_2\beta_{-1}k_1 + \beta_{-1}\beta_{-2}k_1 + \beta_1\beta_2 k_{-1} + \beta_2\beta_{-1}k_{-1}$
C	$\beta_1\beta_2 k_2 + \beta_1\beta_2 k_{-1} + \beta_1 k_2 k_{-1} + \beta_2 k_2 k_{-1}$
D	$\beta_1\beta_2 k_2 + \beta_1\beta_2 k_{-1} + \beta_2 k_1 k_2 + \beta_1 k_2 k_{-1} + \beta_2 k_2 k_{-1}$
E	$\beta_1\beta_2 k_2 + \beta_1\beta_2 k_{-1} + \beta_2\beta_{-1}k_{-1} + \beta_1 k_2 k_{-1} + \beta_2 k_2 k_{-1}$
F	$\beta_1\beta_2 k_2 + \beta_2\beta_{-1}k_1 + \beta_1\beta_2 k_{-1} + \beta_2\beta_{-1}k_{-1} + \beta_2 k_1 k_2 + \beta_1 k_2 k_{-1} + \beta_2 k_2 k_{-1}$
G	$\beta_1\beta_2 k_2 + \beta_1\beta_{-2}k_2 + \beta_1\beta_2 k_{-1} + \beta_1 k_2 k_{-1} + \beta_2 k_2 k_{-1}$
H	$\beta_1\beta_2 k_2 + \beta_1\beta_{-2}k_2 + \beta_1\beta_2 k_{-1} + \beta_2 k_1 k_2 + \beta_{-2}k_1 k_2 + \beta_1 k_2 k_{-1} + \beta_2 k_2 k_{-1}$
I	$\beta_1\beta_2 k_2 + \beta_1\beta_{-2}k_2 + \beta_1\beta_2 k_{-1} + \beta_2\beta_{-1}k_{-1} + \beta_1 k_2 k_{-1} + \beta_2 k_2 k_{-1}$
L	$\beta_1\beta_2 k_2 + \beta_2\beta_{-1}k_1 + \beta_1\beta_{-2}k_2 + \beta_{-1}\beta_{-2}k_1 + \beta_1\beta_2 k_{-1} + \beta_2\beta_{-1}k_{-1} + \beta_2 k_1 k_2 + \beta_{-2}k_1 k_2 + \beta_1 k_2 k_{-1} + \beta_2 k_2 k_{-1}$
M	$\beta_2\beta_{-1}k_1 + \beta_{-1}\beta_{-2}k_1 + \beta_1\beta_2 k_{-1} + \beta_2\beta_{-1}k_{-1} + \beta_1\beta_{-2}k_{-2} + \beta_{-1}\beta_{-2}k_{-2} + \beta_{-1}k_1 k_{-2} + \beta_{-2}k_1 k_{-2} + \beta_1 k_{-1}k_{-2} + \beta_{-1}k_{-1}k_{-2}$
N	$\beta_{-1}\beta_{-2}k_1 + \beta_1\beta_{-2}k_{-2} + \beta_{-1}\beta_{-2}k_{-2} + \beta_{-1}k_1 k_{-2} + \beta_{-2}k_1 k_{-2} + \beta_1 k_{-1}k_{-2} + \beta_{-1}k_{-1}k_{-2}$

B*	$\beta_{2,p}\beta_{-1}k_1 + \beta_{-1}\beta_{-2}k_1 + \beta_1\beta_{2,p}k_{-1} + \beta_{2,p}\beta_{-1}k_{-1}$
C*	$\beta_1\beta_{2,p}k_2 + \beta_1\beta_{2,p}k_{-1} + \beta_1 k_2 k_{-1} + \beta_{2,p}k_2 k_{-1}$
D*	$\beta_1\beta_{2,p}k_2 + \beta_1\beta_{2,p}k_{-1} + \beta_{2,p}k_1 k_2 + \beta_1 k_2 k_{-1} + \beta_{2,p}k_2 k_{-1}$
E*	$\beta_1\beta_{2,p}k_2 + \beta_1\beta_{2,p}k_{-1} + \beta_{2,p}\beta_{-1}k_{-1} + \beta_1 k_2 k_{-1} + \beta_{2,p}k_2 k_{-1}$
F*	$\beta_1\beta_{2,p}k_2 + \beta_{2,p}\beta_{-1}k_1 + \beta_1\beta_{2,p}k_{-1} + \beta_{2,p}\beta_{-1}k_{-1} + \beta_{2,p}k_1 k_2 + \beta_1 k_2 k_{-1} + \beta_{2,p}k_2 k_{-1}$
G*	$\beta_1\beta_{2,p}k_2 + \beta_1\beta_{-2}k_2 + \beta_1\beta_{2,p}k_{-1} + \beta_1 k_2 k_{-1} + \beta_{2,p}k_2 k_{-1}$
H*	$\beta_1\beta_{2,p}k_2 + \beta_1\beta_{-2}k_2 + \beta_1\beta_{2,p}k_{-1} + \beta_{2,p}k_1 k_2 + \beta_{-2}k_1 k_2 + \beta_1 k_2 k_{-1} + \beta_{2,p}k_2 k_{-1}$
I*	$\beta_1\beta_{2,p}k_2 + \beta_1\beta_{-2}k_2 + \beta_1\beta_{2,p}k_{-1} + \beta_{2,p}\beta_{-1}k_{-1} + \beta_1 k_2 k_{-1} + \beta_{2,p}k_2 k_{-1}$
L*	$\beta_1\beta_{2,p}k_2 + \beta_{2,p}\beta_{-1}k_1 + \beta_1\beta_{-2}k_2 + \beta_{-1}\beta_{-2}k_1 + \beta_1\beta_{2,p}k_{-1} + \beta_{2,p}\beta_{-1}k_{-1} + \beta_{2,p}k_1 k_2 + \beta_{-2}k_1 k_2 + \beta_1 k_2 k_{-1} + \beta_{2,p}k_2 k_{-1}$

Table A.4: **Values of the dividing quantities.**

Models	$u = 1$	$u = 0$
Model 5	$\left[\frac{\beta}{2(\beta+k)} \quad \frac{\beta}{2(\beta+k)} \quad \frac{k}{2(\beta+k)}\right]^T$	$\left[\frac{\beta+k}{2\beta+3k} \quad \frac{\beta}{2\beta+3k} \quad \frac{k}{2\beta+3k}\right]^T$
Model 6	$\left[\frac{10\beta}{21\beta+20k} \quad \frac{10\beta}{21\beta+20k} \quad \frac{10k}{21\beta+20k}\right]^T$	$\left[\frac{11\beta+10k}{2(11\beta+15k)} \quad \frac{5\beta}{11\beta+15k} \quad \frac{5k}{11\beta+15k}\right]^T$
Model 7	$\left[\frac{10\beta}{21\beta+20k} \quad \frac{10\beta}{21\beta+20k} \quad \frac{10k+\beta}{21\beta+20k}\right]^T$	$\left[\frac{10k+10\beta}{21\beta+31k} \quad \frac{10\beta}{21\beta+31k} \quad \frac{11k+\beta}{21\beta+31k}\right]^T$
Model 8	$\left[\frac{5\beta}{11\beta+10k} \quad \frac{5\beta}{11\beta+10k} \quad \frac{10k+\beta}{22\beta+20k}\right]^T$	$\left[\frac{10(11\beta+10k)}{231\beta+310k} \quad \frac{100\beta}{231\beta+310k} \quad \frac{110k+11\beta}{231\beta+310k}\right]^T$

Table A.5: **Equilibrium Points evaluated in the Case of dependence on k and β in the presence of $\beta_{2,p}$.** The equilibrium points $\begin{bmatrix}\bar{x}_C^* & \bar{x}_N & \bar{x}_N^*\end{bmatrix}^T$ for each model have been evaluated for $u = 0$ and $u = 1$. The parameters are all dependent on k or β.

Models	$u = 1, \beta_2 = 0$	$u = 0, \beta_2 = 0$
Model 5	$[0 \quad 0 \quad 1]^T$	$[0 \quad 0 \quad 1]^T$
Model 6	$[0 \quad 0 \quad 1]^T$	$[0 \quad 0 \quad 1]^T$
Model 7	$[0 \quad 0 \quad 1]^T$	$[0 \quad 0 \quad 1]^T$
Model 8	$[0 \quad 0 \quad 1]^T$	$[0 \quad 0 \quad 1]^T$

Table A.6: **Equilibrium Points evaluated in the Case of dependence on k and β when $\beta_2, \beta_{2,p} = 0$.** The equilibrium points $\begin{bmatrix}\bar{x}_C^* & \bar{x}_N & \bar{x}_N^*\end{bmatrix}^T$ for each model have been evaluated for $u = 0$ and $u = 1$ when $\beta_2, \beta_{2,p} = 0$. The parameters are all dependent on k or β.

Models	$u = 1, \beta_2 = 0$	$u = 0, \beta_2 = 0$
Model 5	$\left[\frac{\beta}{2\beta + 11k} \quad \frac{\beta}{2\beta + 11k} \quad \frac{10k}{2\beta + 11k}\right]^T$	$\left[\frac{\beta + k}{2(\beta + 6k)} \quad \frac{\beta}{2(\beta + 6k)} \quad \frac{5k}{\beta + 6k}\right]^T$
Model 6	$\left[\frac{10\beta}{21\beta + 110k} \quad \frac{10\beta}{21\beta + 110k} \quad \frac{100k}{21\beta + 110k}\right]^T$	$\left[\frac{11\beta + 10k}{2(11\beta + 60k)} \quad \frac{5\beta}{11\beta + 60k} \quad \frac{50k}{11\beta + 60k}\right]^T$
Model 7	$\left[\frac{\beta}{3\beta + 11k} \quad \frac{\beta}{3\beta + 11k} \quad \frac{\beta + 10k}{3\beta + 11k}\right]^T$	$\left[\frac{\beta + k}{3\beta + 13k} \quad \frac{\beta}{3\beta + 13k} \quad \frac{\beta + 11k}{3\beta + 13k}\right]^T$
Model 8	$\left[\frac{10\beta}{31\beta + 110k} \quad \frac{10\beta}{31\beta + 110k} \quad \frac{100k + 10\beta}{31\beta + 110k}\right]^T$	$\left[\frac{11\beta + 10k}{33\beta + 130k} \quad \frac{10\beta}{33\beta + 130k} \quad \frac{11(\beta + 10k)}{33\beta + 130k}\right]^T$

Table A.7: **Equilibrium Points evaluated in the Case of dependence on k and β, when $\beta_2 = 0$ in the presence of $\beta_{2,p}$.** The equilibrium points $\begin{bmatrix}\bar{x}_C^* & \bar{x}_N & \bar{x}_N^*\end{bmatrix}^T$ for each model have been evaluated for $u = 0$ and $u = 1$ when $\beta_2 = 0$ in the presence of $\beta_{2,p}$. The parameters are all dependent on k or β.

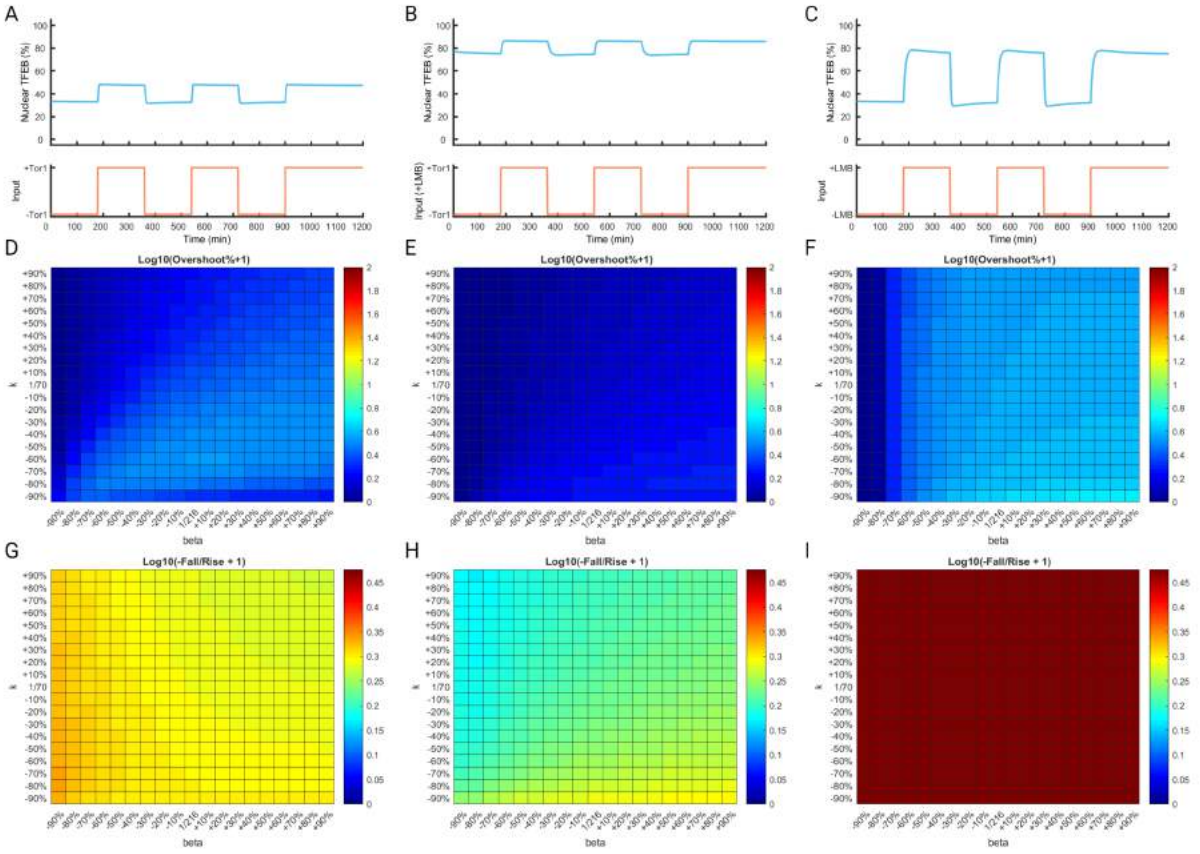

Figure A.1: **Numerical Simulations of TFEB translocation for the NFL on k_{-1} Model.** Simulations of TFEB translocation following a pulse train of Torin 1 (A), Torin 1 supplied with Leptomycin B (B), Leptomycin B (C). Heatmaps of Overshoot% in log10 scale following a pulse train of Torin 1 (D), Torin 1 supplied with Leptomycin B (E), Leptomycin B (F). Heatmaps of Fall over Rise rates ratio in log10 scale following a pulse train of Torin 1 (G), Torin 1 supplied with Leptomycin B (H), Leptomycin B (I). The input is $u = 0$ for the growth condition, and $u = 1$ for the starvation condition. In each heatmap, the de/phosphorylation rate k and the transport rate β are varied between -90% and $+90\%$ of their nominal values $k = \frac{1}{70}$ and $\beta = \frac{1}{216}$.

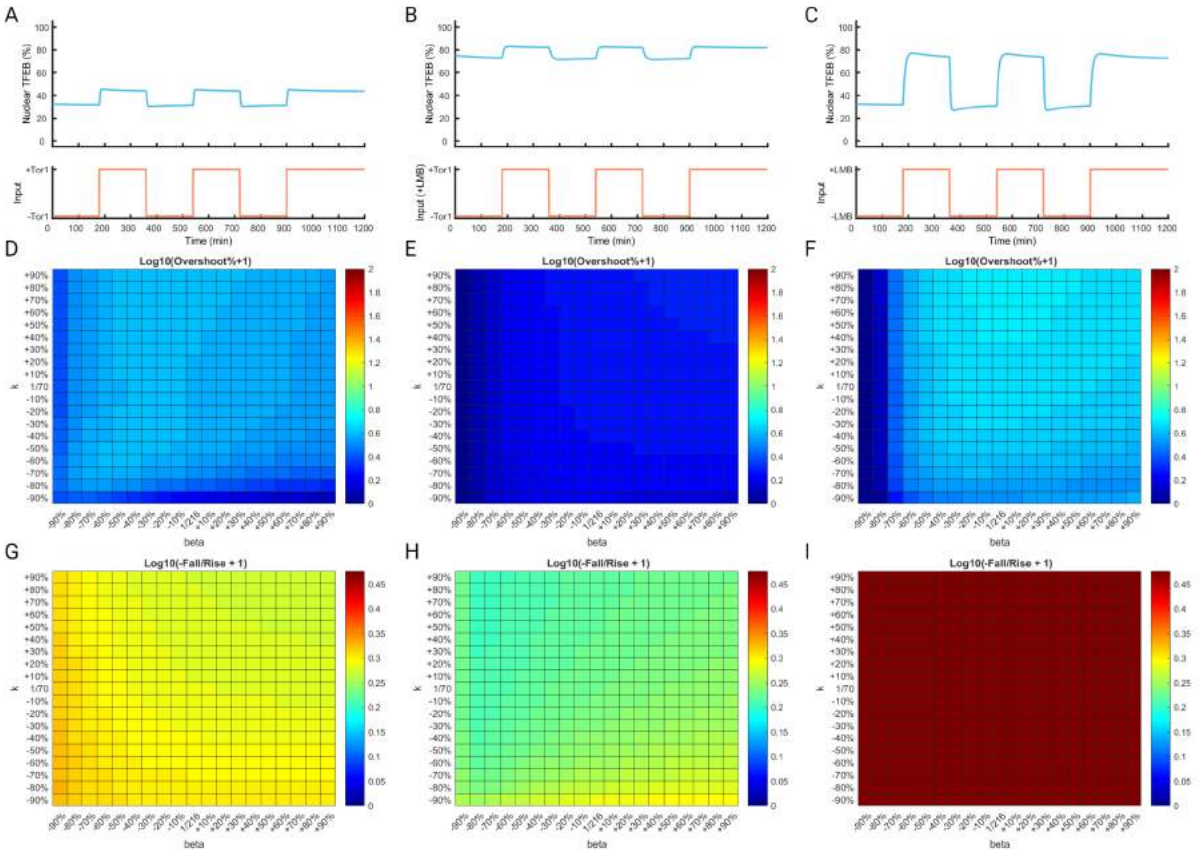

Figure A.2: **Numerical Simulations of TFEB translocation for the NFL on β_1 Model.** Simulations of TFEB translocation following a pulse train of Torin 1 (A), Torin 1 supplied with Leptomycin B (B), Leptomycin B (C). Heatmaps of Overshoot% in log10 scale following a pulse train of Torin 1 (D), Torin 1 supplied with Leptomycin B (E), Leptomycin B (F). Heatmaps of Fall over Rise rates ratio in log10 scale following a pulse train of Torin 1 (G), Torin 1 supplied with Leptomycin B (H), Leptomycin B (I). The input is $u = 0$ for the growth condition, and $u = 1$ for the starvation condition. In each heatmap, the de/phosphorylation rate k and the transport rate β are varied between -90% and $+90\%$ of their nominal values $k = \frac{1}{70}$ and $\beta = \frac{1}{216}$.

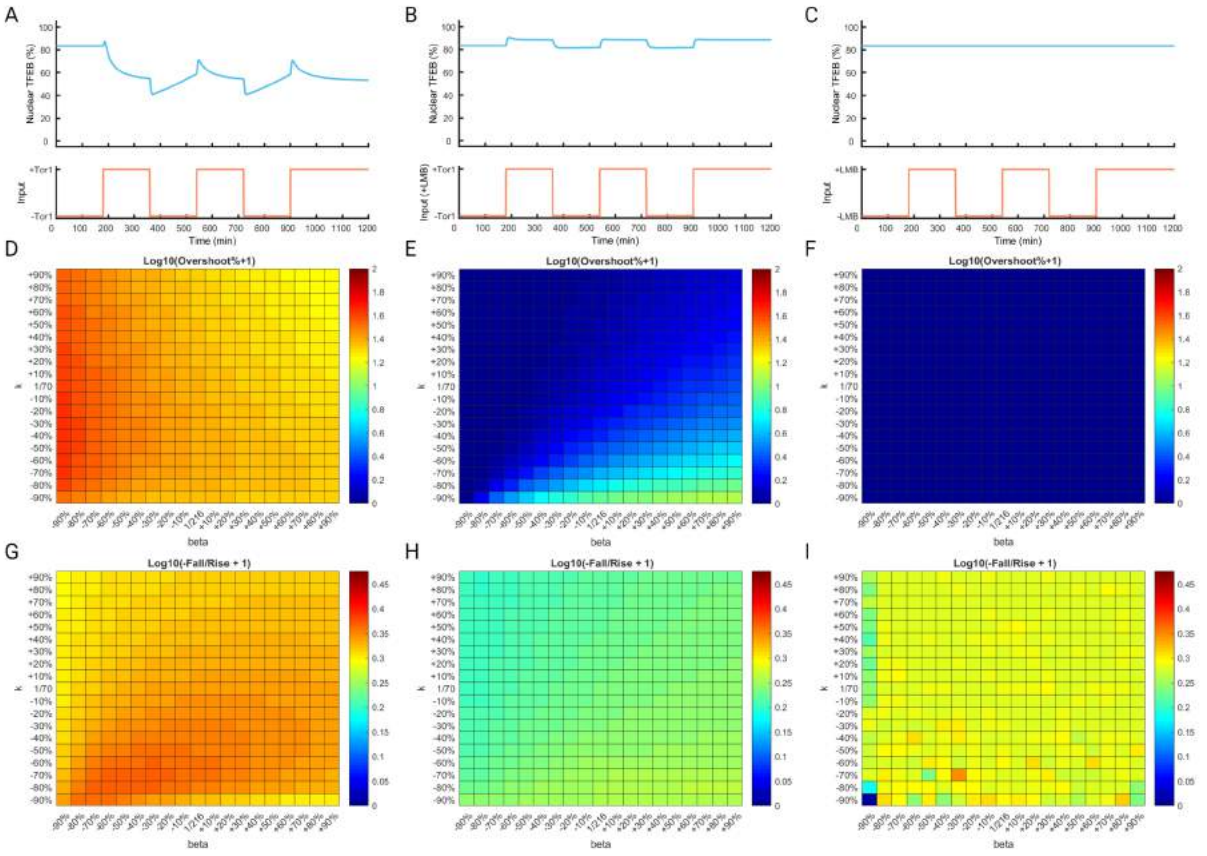

Figure A.3: **Numerical Simulations of TFEB translocation for the IFFL on k_2 Model.** Simulations of TFEB translocation following a pulse train of Torin 1 (A), Torin 1 supplied with Leptomycin B (B), Leptomycin B (C). Heatmaps of Overshoot% in log10 scale following a pulse train of Torin 1 (D), Torin 1 supplied with Leptomycin B (E), Leptomycin B (F). Heatmaps of Fall over Rise rates ratio in log10 scale following a pulse train of Torin 1 (G), Torin 1 supplied with Leptomycin B (H), Leptomycin B (I). The input is $u = 0$ for the growth condition, and $u = 1$ for the starvation condition. In each heatmap, the de/phosphorylation rate k and the transport rate β are varied between -90% and $+90\%$ of their nominal values $k = \frac{1}{70}$ and $\beta = \frac{1}{216}$.

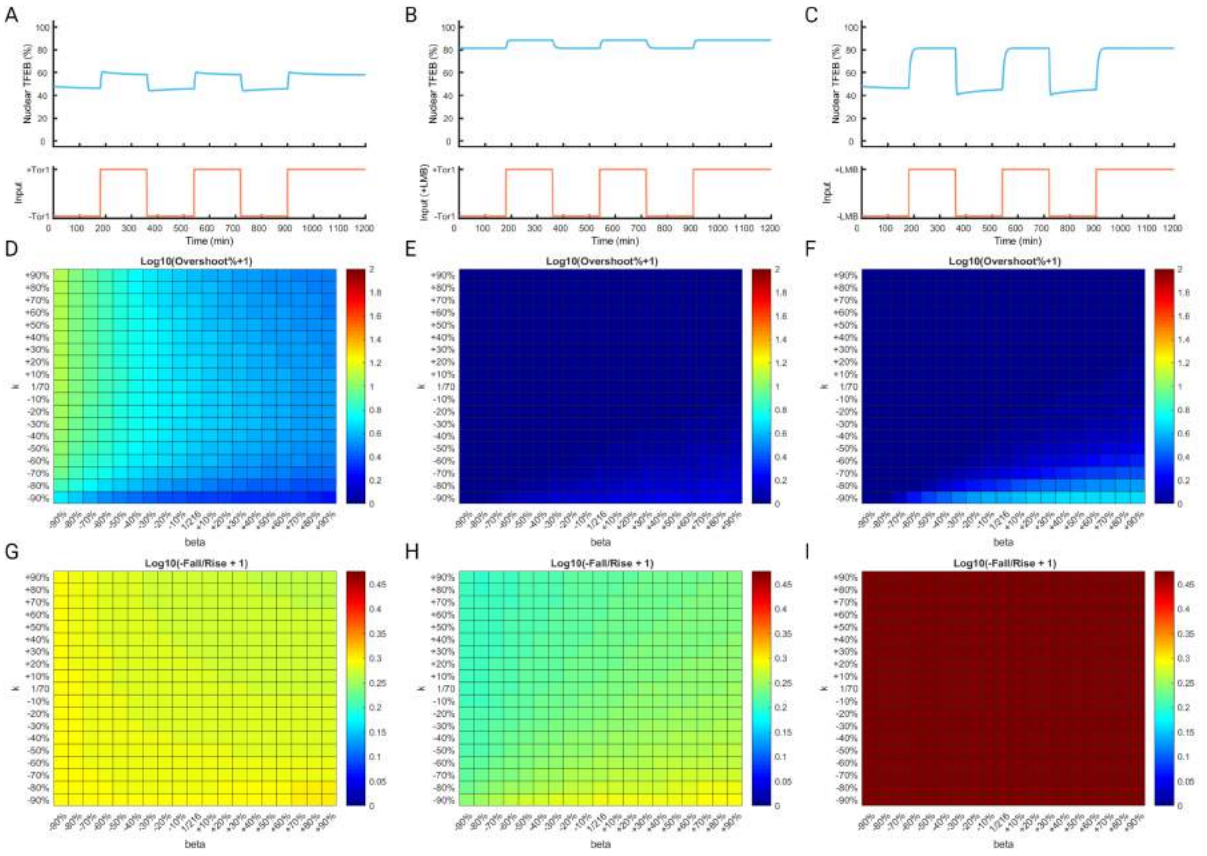

Figure A.4: **Numerical Simulations of TFEB translocation for the NFL on k_2 Model.** Simulations of TFEB translocation following a pulse train of Torin 1 (A), Torin 1 supplied with Leptomycin B (B), Leptomycin B (C). Heatmaps of Overshoot% in log10 scale following a pulse train of Torin 1 (D), Torin 1 supplied with Leptomycin B (E), Leptomycin B (F). Heatmaps of Fall over Rise rates ratio in log10 scale following a pulse train of Torin 1 (G), Torin 1 supplied with Leptomycin B (H), Leptomycin B (I). The input is $u = 0$ for the growth condition, and $u = 1$ for the starvation condition. In each heatmap, the de/phosphorylation rate k and the transport rate β are varied between -90% and $+90\%$ of their nominal values $k = \frac{1}{70}$ and $\beta = \frac{1}{216}$.

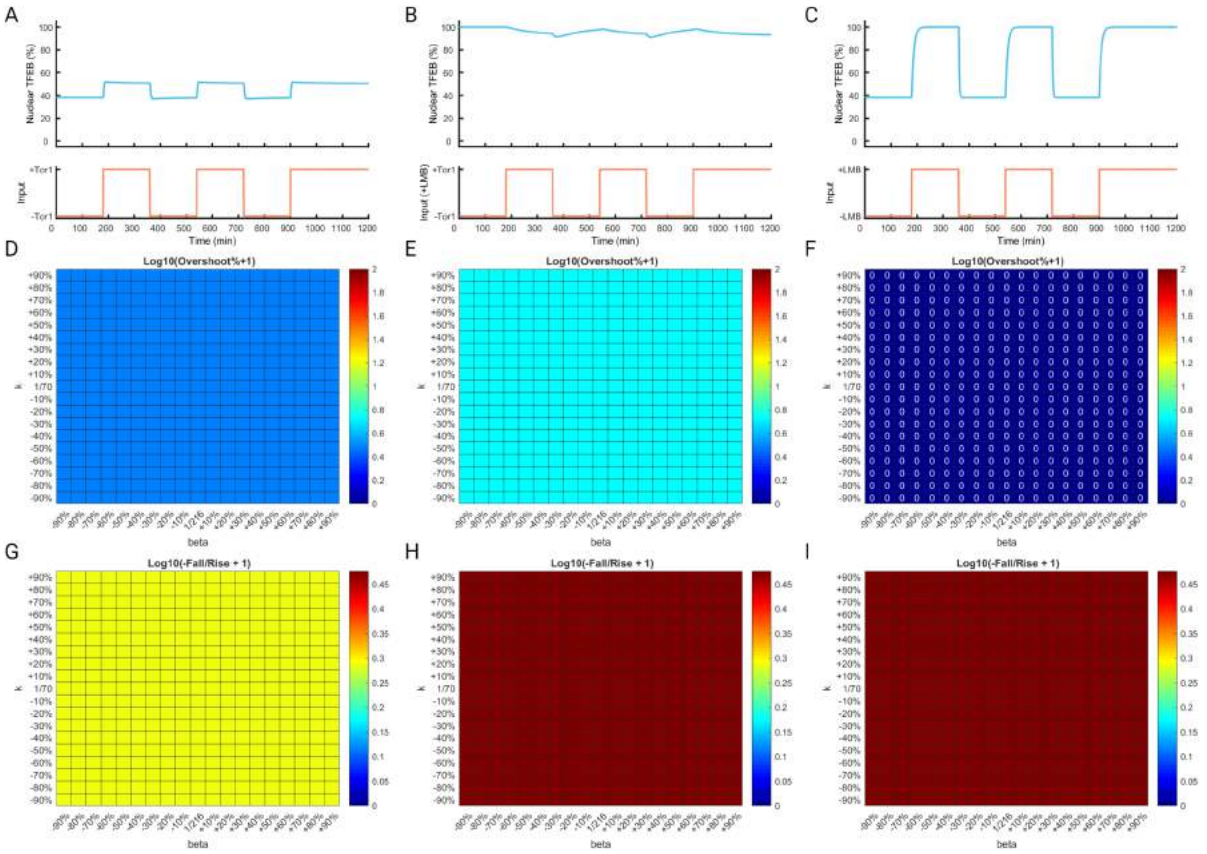

Figure A.5: **Numerical Simulations of TFEB translocation for the IFFL on β_{-1} and $\beta_{2,p}$ Model.** Simulations of TFEB translocation following a pulse train of Torin 1 (A), Torin 1 supplied with Leptomycin B (B), Leptomycin B (C). Heatmaps of Overshoot% in log10 scale following a pulse train of Torin 1 (D), Torin 1 supplied with Leptomycin B (E), Leptomycin B (F). Heatmaps of Fall over Rise rates ratio in log10 scale following a pulse train of Torin 1 (G), Torin 1 supplied with Leptomycin B (H), Leptomycin B (I). The input is $u = 0$ for the growth condition, and $u = 1$ for the starvation condition. In each heatmap, the de/phosphorylation rate k and the transport rate β are varied between -90% and $+90\%$ of their nominal values $k = \frac{1}{70}$ and $\beta = \frac{1}{216}$.

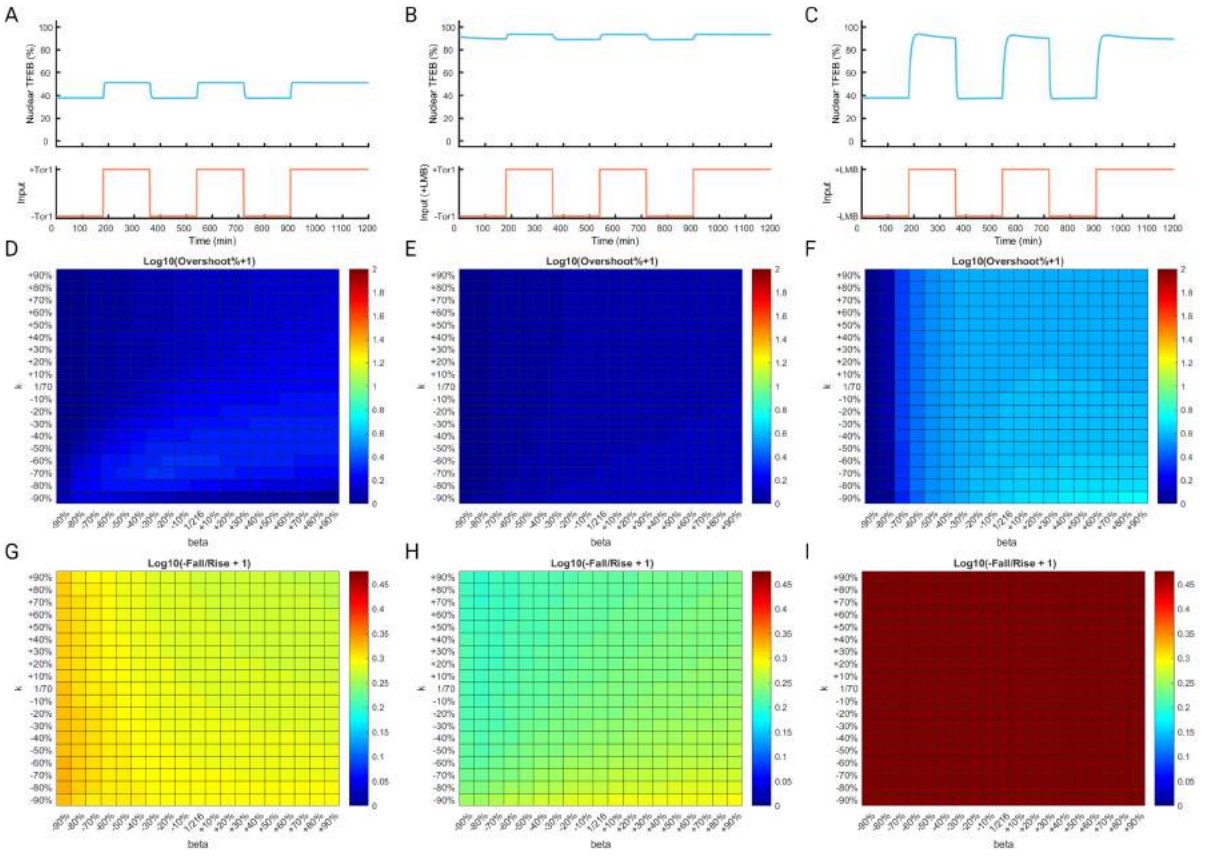

Figure A.6: **Numerical Simulations of TFEB translocation for the NFL on β_{-1} and $\beta_{2,p}$ Model.** Simulations of TFEB translocation following a pulse train of Torin 1 (A), Torin 1 supplied with Leptomycin B (B), Leptomycin B (C). Heatmaps of Overshoot% in log10 scale following a pulse train of Torin 1 (D), Torin 1 supplied with Leptomycin B (E), Leptomycin B (F). Heatmaps of Fall over Rise rates ratio in log10 scale following a pulse train of Torin 1 (G), Torin 1 supplied with Leptomycin B (H), Leptomycin B (I). The input is $u = 0$ for the growth condition, and $u = 1$ for the starvation condition. In each heatmap, the de/phosphorylation rate k and the transport rate β are varied between -90% and $+90\%$ of their nominal values $k = \frac{1}{70}$ and $\beta = \frac{1}{216}$.

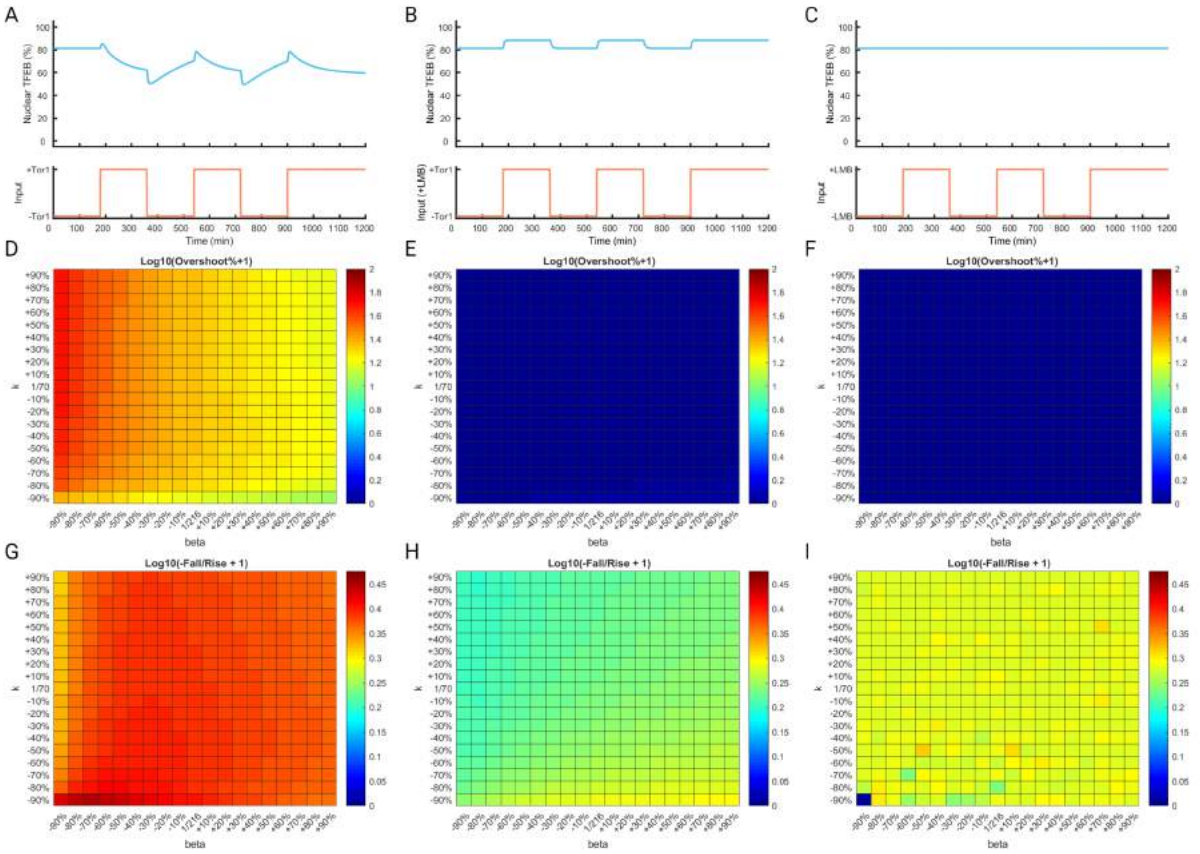

Figure A.7: **Numerical Simulations of TFEB translocation for the IFFL on β_2 Model.** Simulations of TFEB translocation following a pulse train of Torin 1 (A), Torin 1 supplied with Leptomycin B (B), Leptomycin B (C). Heatmaps of Overshoot% in log10 scale following a pulse train of Torin 1 (D), Torin 1 supplied with Leptomycin B (E), Leptomycin B (F). Heatmaps of Fall over Rise rates ratio in log10 scale following a pulse train of Torin 1 (G), Torin 1 supplied with Leptomycin B (H), Leptomycin B (I). The input is $u = 0$ for the growth condition, and $u = 1$ for the starvation condition. In each heatmap, the de/phosphorylation rate k and the transport rate β are varied between -90% and $+90\%$ of their nominal values $k = \frac{1}{70}$ and $\beta = \frac{1}{216}$.

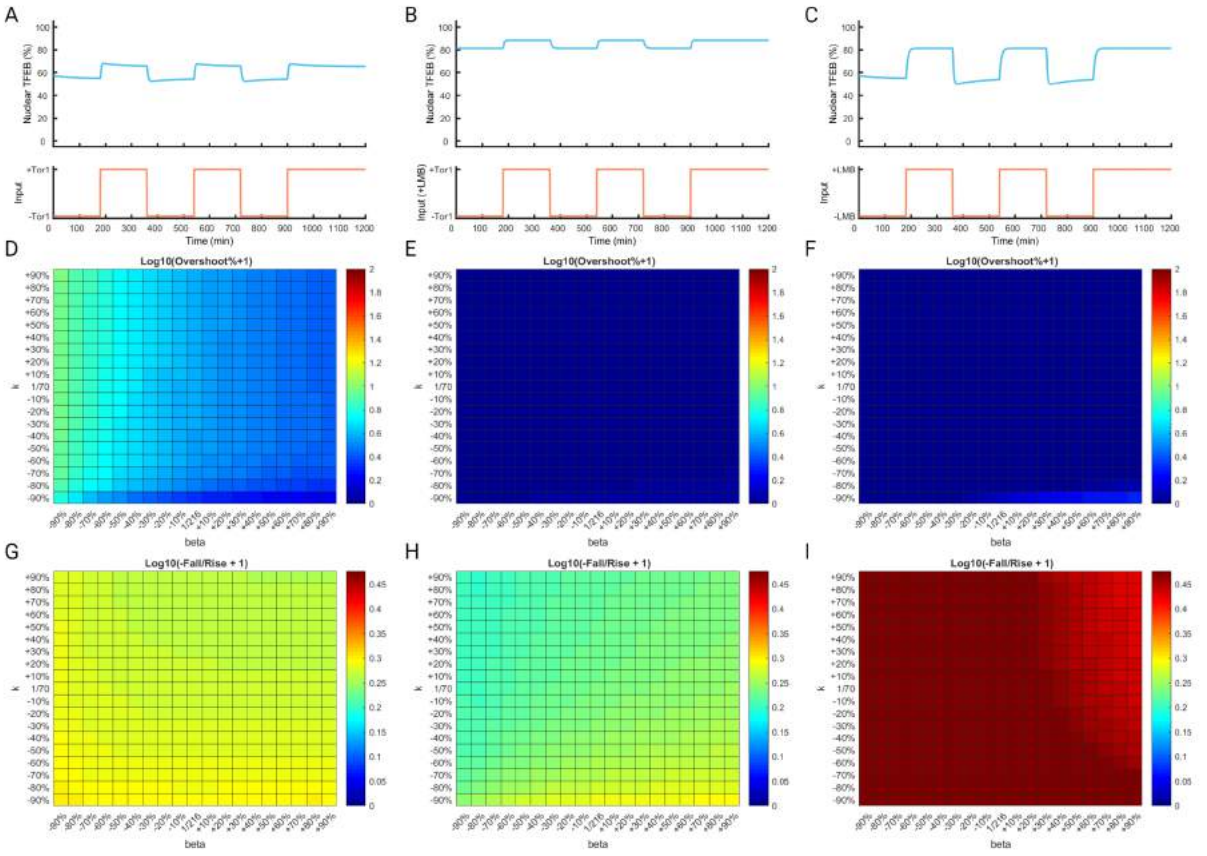

Figure A.8: **Numerical Simulations of TFEB translocation for the NFL on β_2 Model.** Simulations of TFEB translocation following a pulse train of Torin 1 (A), Torin 1 supplied with Leptomycin B (B), Leptomycin B (C). Heatmaps of Overshoot% in log10 scale following a pulse train of Torin 1 (D), Torin 1 supplied with Leptomycin B (E), Leptomycin B (F). Heatmaps of Fall over Rise rates ratio in log10 scale following a pulse train of Torin 1 (G), Torin 1 supplied with Leptomycin B (H), Leptomycin B (I). The input is $u = 0$ for the growth condition, and $u = 1$ for the starvation condition. In each heatmap, the de/phosphorylation rate k and the transport rate β are varied between -90% and $+90\%$ of their nominal values $k = \frac{1}{70}$ and $\beta = \frac{1}{216}$.

Appendix B

Materials and Methods

B.1 Cell Culture

HeLa cells stably expressing TFEB tagged with a GFP (TFEB-GFP) are used in the experiments. HeLa cells are cultured in RPMI 1640 (EuroClone) supplemented with 10% FBS (EuroClone), 1% Penicillin/Streptomycin (EuroClone), 2 mM Glutamine (EuroClone) and $1 mg/ml$ G418 (Sigma-Aldrich Co.) and are kept in a standard tissue culture incubator at $37°C$, 5% CO_2, 98% of humidity. Cells are splitted twice per week using PBS (Gibco) and trypsin (Gibco) and seeded on average at $15000 cells/cm^2$ in a T25 flask. The day before the loading of the microfluidic device cells were splitted 1:3 and placed back into the incubator.

B.2 Microfluidics

All the experiments presented in this work were performed using the microfluidic devices described in Section 2.3. In particular, the amino acid starvation experiments were conducted by using the VersaLive platform; the other experiments were performed by using the device for dynamic stimulation. Here, the fabrication and the loading protocols of the chips will be described.

B.2.1 Device for dynamic input experiments Fabrication Protocol

The fabrication protocol is adapted from [41]. A replica molding technique is used to obtain polydimethylsiloxane (PDMS) replicas of the microfluidic device by using a master mold. The master mold has been produced using a 4" ($10.16cm$) silicon wafer as substrate (Silicon Valley Microelectronics, US) by a way of layer-by-layer photolithography. Negative photoresists (Microchem Corporation) were used to create the master mold. Specifically, SU-8 2015 was spun at 3300 and 1000 rpm to generate the 15 microns DAW and 40 microns main channels, respectively, and SU-8 2005 was spun at 3000 rpm to generate the 5 microns layer of chaotic mixers which serve to ensure uniform mixing of the DAW inputs.

Before the fabrication of the microfluidic devices the master is exposed to chlorotrimethylsilane (Sigma-Aldrich Co.) vapours for 10 minutes in order to create an anti-sticking silane layer for PDMS. PDMS is prepared by mixing Sylgard 184 Elastomer curing agent and base (DOW corning) in a $1:10$ ratio. PDMS is poured onto the master mold, degassed for 30 minutes, cured for 1 hour at 80°, allowed to cool to room temperature and then peeled from the wafer. PDMS was then autoclaved for 30 minutes at 121° to ensure long-term viability of cells in the devices [14]. Holes for the 7 ports were punched using a 24-gauge blunt needle in order to create fluidic ports for the access of cells and liquid substances. The PDMS devices obtained are rinsed in isopropyl alcohol and distilled water to remove debris. For each PDMS piece containing microchannels a thin glass slide (150 microns) is cleaned in methanol and 70% ethyl alcohol. Finally the PDMS layers and glass slides are exposed to air plasma in Plasma Cleaner machine (ZEPTO version B, Diener electronic GmbH) for 30 seconds and brought into contact forms a strong irreversible bond between two surfaces. As last step all devices were checked for faults inside and outside the channels.

B.2.2 Device for dynamic input experiments Cells Loading Protocol

The cells loading protocol is adapted from [41]. For device loading, cells are washed with sterile Phosphate-Buffered Saline (PBS, Gibco), detached from the culture dishes by exposing to 0.25% Trypsin EDTA for 1 minute and centrifuged to form a pellet. Then, in

order to obtain a seeding density of 5 - 7 cells per chamber, the cells pellet is re-suspended in complete media at a density of 0.064 cells per mm^2.

The channel of the device are then completely filled with fluid (except for the culture chambers) by applying complete media first through port 5 and then through port 2 once it is filled with fluid. The cell suspension is loaded into the main channel of the device from port 2 and a vacuum is applied in the channel adjacent to the culture chambers (ports 3 and 4) to evacuate air and replace the chamber volume with fluid containing cells. Remaining untrapped cells in the main channel are washed away at a high flow rate without disturbing cells inside the traps. Fluidic connections from the ports of the device to syringes containing growth medium are then established using 24 gauge PTFE tubing (Cole-Parmer Inc.).

Once cells are loaded in the microfluidic device, they are allowed in a cell culture incubator for 24 hours in perfusion conditions providing that the cells in chambers receive fresh medium from syringe connected to port 5 and the waste medium is washed through port 1, while all the other ports (2, 6 and 7) are plugged: port 2 is plugged with a node; ports 6 and 7 are connected through a bridge to balance the pressure.

The robust growth and colonization of the device culture chambers by this cell line indicates that application of a temporary on-chip vacuum during loading is not detrimental to cell viability or proliferation and is a novel useful method for delivering cells in suspension into isolated chambers within a microfluidic device [41].

B.2.3 VersaLive Fabrication Protocol

The protocol is adapted from [68]. Microfluidic chips have been fabricated by using a combination of standard photolithography and soft lithography procedures [23]. The geometry of the device is shown in The master mold has been microfabricated via mask photolithography of SU-8 negative photoresist (SU-8 3035, Kayaku Advanced Materials Inc.) on silicon wafer substrate. The photoresist was spin coated to reach a final thickness of 25 microns and processed following the guidelines of the manufacturer Before the first utilization of the master, the passivation of its surface is required to facilitate the release step during soft lithography.

The master was passivated by vapor deposition of perfluorosilane (1H,1H,2H,2H-

perfluorooctyl-trichlorosilane, Merck kGaA). Specifically, the master was placed in a desiccator with a small vial containing 20 μL of perfluorosilane. Vacuum was then applied overnight to allow the perfluorosilane to evaporate and to react with the surface of the silicon wafer, forming a covalently bound super-hydrophobic coating.

The passivated master is then used as a mold for the soft lithography part of the fabrication process of the microfluidic device. The elastomer base of the PDMS is thoroughly mixed with the curing agent in a 10:1 ratio as reported by the datasheet of the manufacturer (Sylgard 184, Dow Corning). Air bubbles are removed from the uncured polymer applying vacuum to the mix for 2 hours or until no bubbles are visible. The mix is then poured onto the master mold for a final thickness of about 5 mm. If required, vacuum can be applied a second time to remove the bubbles formed during the pouring step. The mold with the uncured PDMS is then placed in oven at 80°C for a minimum of 2 hours to accelerate the crosslink of the polymer mix. Once cured, the PDMS is peeled off the master mold. The PDMS slab is then placed with the pattern features facing up to cut out the single chips. Similarly, access ports are opened using a 3-mm biopsy punch (ref. 504649, World Precision Instruments).

The channels of the PDMS chips are sealed by plasma bonding the chips to round glass cover slides (30 mm in diameter, thickness no. 1, Marienfeld). Glass slides and PDMS chips were first cleaned from dust particles using adhesive tape. For the surface activation of glass slides and PDMS chips, 85W air plasma at 0.4 mbar or lower (ZEPTO version B, Diener electronic GmbH & Co. KG) was used. For the permanent bond 30 seconds of air plasma are used respectively. As last step all devices were checked for faults inside and outside the channels.

B.2.4 VersaLive: Wetting and Cell Loading

The protocol is adapted from [68]. To ease the wetting process, the temporary hydrophilicity of the PDMS surface after the plasma activation is exploited. Consequently, the wetting of the channels is carried out within minutes after the bonding procedure. The wetting and the cell loading operations are carried out upon visual check using an inverted stereomicroscope (Leica Microsystems). For the wetting of the microfluidic channels, 10 μL

of PBS are added in port B of the chip until all channels are filled. If required, all ports are filled with 10 μL of PBS and the chip is placed in a desiccator, vacuum is applied for 15 minutes or until all air bubbles disappeared. Successively, the PBS is removed from all reservoirs and 10 μL of cell suspension ($1–5*10^6 cell/mL$) are added to port B of the device. Cells start to flow through the main channel and to enter into the chambers. When a given chamber is filled with the suited number of cells, 10 μL of cell medium are added to the respective port to decrease the flow rate across that chamber. When all chambers are filled, 20 μL of cell media is added to port A and port B is emptied to wash the main channel from undesired cells. Port B is then rinsed and filled with 20 μL of cell media. Next, all input ports from #1 to #5 are filled up to a final volume of 20 μL of fresh cell media. An equal volume of cell media in all ports prevents the formation of pressure drops across the chip and enables the static cell culture. Ultimately, 2.5 μL of mineral oil for cell culture (M8410, Merck kGaA) are added to each reservoir to prevent the evaporation of its content when the chip is placed into the cell incubator. The chips stayed in the incubator overnight at 37° 100% humidity and 5% of CO_2 atmosphere prior to the beginning of the experiments.

B.2.5 VersaLive: Single/Multi-input mode

The protocol is adapted from [68]. After the steps described in Subsection B.2.4 is possible to operate in the perfusion cell culture regime. In order to generate a pressure drop the ports content must be removed according to specific mode used. In the Single-Input mode all the ports are rapidly emptied and ports A is filled with 20 μL of the desired input. Conversely, in the Multi-Input case ports A and B are emptied and the content in ports 1 to 6 is rapidly substituted with 20 μL of the desired input.

B.2.6 Experimental protocol

The protocol is adapted from [64]. The microfluidics experimental platform was initialised as previously described [75]. The microfluidic device is secured on the microscope stage within an environmental chamber maintained at 37 °C with humidified 5% CO_2. The

treatments were provided for the VersaLive platform in a multi-input mode by replacing the growing medium with the treatment using a standard pipette. on the other hand, in the case of the device for dynamic input, 60 mL syringes are connected to its ports and hanged at different heights, in order to regulate the flow from the inlets (ports 6 and 7) to the outlets (ports 5, 1 and 2) according to hydrostatic pressure. The syringes connected to the outlets port contain 10 mL of standard complete culture medium and they serve as a waste tanks. The syringes connected to the inlets port are filled as indicated in each experiment, and secured on the linear actuator.

B.3 Starvation Treatments

For experiments involving complete starvation I utilized HBSS (Gibco) as starvation medium and complete RPMI (supplemented as indicated in Section B.1) as growth medium.

For experiments involving amino acid starvation I utilized the procedure described in [62]. Cells loaded in Versalive microfluidic chips [68] were treated for three hours with growth medium supplemented or depleted with amino acids. The growth medium depleted with amino acids is composed by amino acid-free RPMI (USBiological) supplemented with 10% dialyzed FBS. The growth medium supplemented with amino acids is composed by amino acid-free RPMI (USBiological) supplemented with 10% dialyzed FBS, 1× water-solubilized mix of essential (Thermo Fisher Scientific) and non-essential (Thermo Fisher Scientific) amino acids.

In the amino acid starvation dose test I supplemented RPMI depleted with amino acids with varying doses of RPMI resupplied with amino acids (from 1:5 to 1:10000) to treat cells at various levels of amino acid deprivation.

B.4 Materials

Chemicals used in the studies detailed in Section 3.2 were obtained from the following sources: Torin 1 (Selleck Chemicals); Bafilomycin A1 (Selleck Chemicals); Leptomycin B (Sigma); Bortezomib (Selleck Chemicals); Cycloheximide (Sigma); Actinomycin D (Sigma).

Drug concentrations were indicated in Section 3.2. The pretreatment was performed only where indicated in Section 3.2.

Bibliography

[1] Alan Aderem. Systems biology: its practice and challenges. *Cell*, 121(4):511–513, 2005.

[2] Uri Alon. *An introduction to systems biology: design principles of biological circuits*. Chapman and Hall/CRC, 2006.

[3] Uri Alon. *An Introduction to Systems Biology; Design Principles of Biological Circuits*. Chapman and Hall/CRC, second edition, 2017.

[4] Pedram Argani, Man Yee Lui, Jérôme Couturier, Raymonde Bouvier, Jean-Christophe Fournet, and Marc Ladanyi. A novel cltc-tfe3 gene fusion in pediatric renal adenocarcinoma with t (x; 17)(p11. 2; q23). *Oncogene*, 22(34):5374–5378, 2003.

[5] G. L. Atkins. Multicompartment models for biological systems. 1969.

[6] Nancy G Azizian and Yulin Li. Xpo1-dependent nuclear export as a target for cancer therapy. *Journal of Hematology & Oncology*, 13(1):1–9, 2020.

[7] Shashi Bala and Gyongyi Szabo. Tfeb, a master regulator of lysosome biogenesis and autophagy, is a new player in alcoholic liver disease. *Digestive medicine research*, 1, 2018.

[8] Valerio Benedetti. *Analysis of TFEB nucleo-cytoplasmic shuttling dynamics in response to nutrient availability*. Tesi di dottorato in systems medicine (curriculum in human genetics), xxxi ciclo, European School of Molecular Medicine (SEMM), University of Milan and University of Naples "Federico II", 2018/2019.

[9] Olivier Bensaude. Inhibiting eukaryotic transcription. which compound to choose? how to evaluate its activity? which compound to choose? how to evaluate its activity? *Transcription*, 2(3):103–108, 2011.

[10] Arthur R Birt, Georgina R Hogg, and W James Dubé. Hereditary multiple fibrofolliculomas with trichodiscomas and acrochordons. *Archives of dermatology*, 113(12):1674–1677, 1977.

[11] Owen A Brady, Eutteum Jeong, José A Martina, Mehdi Pirooznia, Ilker Tunc, and Rosa Puertollano. The transcription factors tfe3 and tfeb amplify p53 dependent transcriptional programs in response to dna damage. *Elife*, 7:e40856, 2018.

[12] Alessia Calcagnì, Eric Verschuren, Rossella De Cegli, Nicolina Zampelli, Edoardo Nusco, Stefano Confalonieri, Giovanni Bertalot, Salvatore Pece, Carmine Settembre, Gabriel G Malouf, et al. Modelling tfe renal cell carcinoma in mice reveals a critical role of wnt signaling. *Elife*, 5:e17047, 2016.

[13] Santosh Chauhan, Zahra Ahmed, Steven B Bradfute, John Arko-Mensah, Michael A Mandell, Seong Won Choi, Tomonori Kimura, Fabien Blanchet, Anna Waller, Michal H Mudd, et al. Pharmaceutical screen identifies novel target processes for activation of autophagy with a broad translational potential. *Nature communications*, 6(1):1–15, 2015.

[14] Daniel T Chiu, Noo Li Jeon, Sui Huang, Ravi S Kane, Christopher J Wargo, Insung S Choi, Donald E Ingber, and George M Whitesides. Patterned deposition of cells and proteins onto surfaces by using three-dimensional microfluidic systems. *Proceedings of the National Academy of Sciences*, 97(6):2408–2413, 2000.

[15] Jeremy Clark, Yong-Jie Lu, Sanjiv K Sidhar, Chris Parker, Sandra Gill, Damian Smedley, Rifat Hamoudi, W Marston Linehan, Janet Shipley, and Colin S Cooper. Fusion of splicing factor genes psf and nono (p54nrb) to the tfe3 gene in papillary renal cell carcinoma. *Oncogene*, 15(18):2233–2239, 1997.

[16] Monique P Curran and Kate McKeage. Bortezomib. *Drugs*, 69(7):859–888, 2009.

[17] Mickael Decressac, Bengt Mattsson, Pia Weikop, Martin Lundblad, Johan Jakobsson, and Anders Björklund. Tfeb-mediated autophagy rescues midbrain dopamine neurons from α-synuclein toxicity. *Proceedings of the National Academy of Sciences*, 110(19):E1817–E1826, 2013.

[18] Benjamin Dehay, Jordi Bové, Natalia Rodríguez-Muela, Celine Perier, Ariadna Recasens, Patricia Boya, and Miquel Vila. Pathogenic lysosomal depletion in parkinson's disease. *Journal of Neuroscience*, 30(37):12535–12544, 2010.

[19] Noah Dephoure, Chunshui Zhou, Judit Villén, Sean A Beausoleil, Corey E Bakalarski, Stephen J Elledge, and Steven P Gygi. A quantitative atlas of mitotic phosphorylation. *Proceedings of the National Academy of Sciences*, 105(31):10762–10767, 2008.

[20] Chiara Di Malta, Diletta Siciliano, Alessia Calcagni, Jlenia Monfregola, Simona Punzi, Nunzia Pastore, Andrea N Eastes, Oliver Davis, Rossella De Cegli, Angela Zampelli, et al. Transcriptional activation of ragd gtpase controls mtorc1 and promotes cancer growth. *Science*, 356(6343):1188–1192, 2017.

[21] Ricardo E Dolmetsch, Richard S Lewis, Christopher C Goodnow, and James I Healy. Differential activation of transcription factors induced by ca2+ response amplitude and duration. *Nature*, 386(6627):855–858, 1997.

[22] Mathieu Ferron, Carmine Settembre, Junko Shimazu, Julie Lacombe, Shigeaki Kato, David J Rawlings, Andrea Ballabio, and Gerard Karsenty. A rankl–pkcβ–tfeb signaling cascade is necessary for lysosomal biogenesis in osteoclasts. *Genes & development*, 27(8):955–969, 2013.

[23] Mike S Ferry, Ivan A Razinkov, and Jeff Hasty. Microfluidics for synthetic biology: from design to execution. In *Methods in enzymology*, volume 497, pages 295–372. Elsevier, 2011.

[24] Gianfranco Fiore. *Identification and control of gene networks in living cells*. Biologia computazionale e bioinformatica, xxvii ciclo, University of Naples "Federico II", 2014/2015.

[25] C. Fracassi et al. Automatic control of gene expression in mammalian cells. *ACS synthetic biology*, 5(4):296–302, 2016.

[26] Xuekun Fu, Chao Liang, Fangfei Li, Luyao Wang, Xiaoqiu Wu, Aiping Lu, Guozhi Xiao, and Ge Zhang. The rules and functions of nucleocytoplasmic shuttling proteins. *International journal of molecular sciences*, 19(5):1445, 2018.

[27] Gennaro Gambardella, Leopoldo Staiano, Maria Nicoletta Moretti, Rossella De Cegli, Luca Fagnocchi, Giuseppe Di Tullio, Sara Polletti, Clarissa Braccia, Andrea Armirotti, Alessio Zippo, et al. Gadd34 is a modulator of autophagy during starvation. *Science advances*, 6(39):eabb0205, 2020.

[28] Alexandra Giatromanolaki, Dimitra Kalamida, Efthimios Sivridis, Ilias V Karagounis, Kevin C Gatter, Adrian L Harris, and Michael I Koukourakis. Increased expression of transcription factor eb (tfeb) is associated with autophagy, migratory phenotype and poor prognosis in non-small cell lung cancer. *Lung cancer*, 90(1):98–105, 2015.

[29] W Heinemeyer, PC Ramos, and RJ Dohmen. Ubiquitin-proteasome system. *Cellular and Molecular Life Sciences CMLS*, 61(13):1562–1578, 2004.

[30] Oliver Hilsenbeck, Michael Schwarzfischer, Dirk Loeffler, Sotiris Dimopoulos, Simon Hastreiter, Carsten Marr, Fabian J Theis, and Timm Schroeder. faster: a user-friendly tool for ultrafast and robust cell segmentation in large-scale microscopy. *Bioinformatics*, 33(13):2020–2028, 2017.

[31] Cynthia L Hsu, Elian X Lee, Kara L Gordon, Edwin A Paz, Wen-Chuan Shen, Kohta Ohnishi, Jill Meisenhelder, Tony Hunter, and Albert R La Spada. Map4k3 mediates amino acid-dependent regulation of autophagy via phosphorylation of tfeb. *Nature Communications*, 9(1):1–15, 2018.

[32] Alon Kalo and Yaron Shav-Tal. Acting on impulse: dissecting the dynamics of the nfat transcriptional response. *Genome biology*, 14(1):1–4, 2013.

[33] Pulak Kar, Gary R Mirams, Helen C Christian, and Anant B Parekh. Control of nfat isoform activation and nfat-dependent gene expression through two coincident and spatially segregated intracellular ca2+ signals. *Molecular cell*, 64(4):746–759, 2016.

[34] Pulak Kar, Charmaine Nelson, and Anant B Parekh. Selective activation of the transcription factor nfat1 by calcium microdomains near ca2+ release-activated ca2+ (crac) channels. *Journal of Biological Chemistry*, 286(17):14795–14803, 2011.

[35] Pulak Kar and Anant B Parekh. Distinct spatial ca2+ signatures selectively activate different nfat transcription factor isoforms. *Molecular cell*, 58(2):232–243, 2015.

[36] Kiri Kilpatrick, Yimeng Zeng, Tommy Hancock, and Laura Segatori. Genetic and chemical activation of tfeb mediates clearance of aggregated α-synuclein. *PloS one*, 10(3):e0120819, 2015.

[37] Koray Kırlı, Samir Karaca, Heinz Jürgen Dehne, Matthias Samwer, Kuan Ting Pan, Christof Lenz, Henning Urlaub, and Dirk Görlich. A deep proteomics perspective on crm1-mediated nuclear export and nucleocytoplasmic partitioning. *elife*, 4:e11466, 2015.

[38] Marc W Kirschner. The meaning of systems biology. *Cell*, 121(4):503–504, 2005.

[39] Hiroaki Kitano. Systems biology: a brief overview. *science*, 295(5560):1662–1664, 2002.

[40] Peter Kohl, Edmund J Crampin, TA Quinn, and Denis Noble. Systems biology: an approach. *Clinical Pharmacology & Therapeutics*, 88(1):25–33, 2010.

[41] M. Kolnik et al. Vacuum-assisted cell loading enables shear-free mammalian microfluidic culture. *Lab on a chip*, 12(22):4732–4737, 2012.

[42] Nobuaki Kudo, Nobuaki Matsumori, Hiroshi Taoka, Daisuke Fujiwara, Erwin P Schreiner, Barbara Wolff, Minoru Yoshida, and Sueharu Horinouchi. Leptomycin b inactivates crm1/exportin 1 by covalent modification at a cysteine residue in the central conserved region. *Proceedings of the National Academy of Sciences*, 96(16):9112–9117, 1999.

[43] Nobuaki Kudo, Barbara Wolff, Toshihiro Sekimoto, Erwin P Schreiner, Yoshihiro Yoneda, Mitsuhiro Yanagida, Sueharu Horinouchi, and Minoru Yoshida. Leptomycin b inhibition of signal-mediated nuclear export by direct binding to crm1. *Experimental cell research*, 242(2):540–547, 1998.

[44] Roland P Kuiper, Marga Schepens, José Thijssen, Martien van Asseldonk, Eva van den Berg, Julia Bridge, Ed Schuuring, Eric FPM Schoenmakers, and Ad Geurts van Kessel. Upregulation of the transcription factor tfeb in t (6; 11)(p21; q13)-positive renal cell carcinomas due to promoter substitution. *Human molecular genetics*, 12(14):1661–1669, 2003.

[45] Marc Ladanyi, Man Yee Lui, Cristina R Antonescu, Amber Krause-Boehm, Alfons Meindl, Pedram Argani, John H Healey, Takafumi Ueda, Hideki Yoshikawa, Aurelia Meloni-Ehrig, et al. The der (17) t (x; 17)(p11; q25) of human alveolar soft part sarcoma fuses the tfe3 transcription factor gene to aspl, a novel gene at 17q25. *Oncogene*, 20(1):48–57, 2001.

[46] Chunyan Li, Xin Wang, Xuezhi Li, Kaixin Qiu, Fengjuan Jiao, Yidan Liu, Qingxia Kong, Yan Liu, and Yili Wu. Proteasome inhibition activates autophagy-lysosome pathway associated with tfeb dephosphorylation and nuclear translocation. *Frontiers in cell and developmental biology*, 7:170, 2019.

[47] L. Li et al. A tfeb nuclear export signal integrates amino acid supply and glucose availability. *Nature communications*, 9(1):1–15, 2018.

[48] Yang Li, Meng Xu, Xiao Ding, Chen Yan, Zhiqin Song, Lianwan Chen, Xiahe Huang, Xin Wang, Youli Jian, Guihua Tang, et al. Protein kinase c controls lysosome biogenesis independently of mtorc1. *Nature cell biology*, 18(10):1065–1077, 2016.

[49] Christine Loh, Karen T-Y Shaw, Josephine Carew, Joao PB Viola, Chun Luo, Brian A Perrino, and Anjana Rao. Calcineurin binds the transcription factor nfat1 and reversibly regulates its activity (). *Journal of Biological Chemistry*, 271(18):10884–10891, 1996.

[50] Parisa Lotfi, Dennis Y Tse, Alberto Di Ronza, Michelle L Seymour, Giuseppe Martano, Jonathan D Cooper, Fred A Pereira, Maria Passafaro, Samuel M Wu, and Marco Sardiello. Trehalose reduces retinal degeneration, neuroinflammation and storage burden caused by a lysosomal hydrolase deficiency. *Autophagy*, 14(8):1419–1434, 2018.

[51] Benoît Marchand, Dominique Arsenault, Alexandre Raymond-Fleury, François-Michel Boisvert, and Marie-Josée Boucher. Glycogen synthase kinase-3 (gsk3) inhibition induces prosurvival autophagic signals in human pancreatic cancer cells. *Journal of Biological Chemistry*, 290(9):5592–5605, 2015.

[52] J. A Martina et al. Mtorc1 functions as a transcriptional regulator of autophagy by preventing nuclear transport of tfeb. *Autophagy*, 8(6):903–914, 2012.

[53] José A Martina, Heba I Diab, Owen A Brady, and Rosa Puertollano. Tfeb and tfe 3 are novel components of the integrated stress response. *The EMBO journal*, 35(5):479–495, 2016.

[54] Jose A Martina and Rosa Puertollano. Rag gtpases mediate amino acid–dependent recruitment of tfeb and mitf to lysosomes. *Journal of Cell Biology*, 200(4):475–491, 2013.

[55] Caroline Mauvezin and Thomas P Neufeld. Bafilomycin a1 disrupts autophagic flux by inhibiting both v-atpase-dependent acidification and ca-p60a/serca-dependent autophagosome-lysosome fusion. *Autophagy*, 11(8):1437–1438, 2015.

[56] D. L. Medina et al. Lysosomal calcium signalling regulates autophagy through calcineurin and tfeb. *Nature cell biology*, 17(3):288–299, 2015.

[57] Diego L Medina and Andrea Ballabio. Lysosomal calcium regulates autophagy. *Autophagy*, 11(6):970–971, 2015.

[58] Diego L Medina, Alessandro Fraldi, Valentina Bouche, Fabio Annunziata, Gelsomina Mansueto, Carmine Spampanato, Claudia Puri, Antonella Pignata, Jose A Martina,

Marco Sardiello, et al. Transcriptional activation of lysosomal exocytosis promotes cellular clearance. *Developmental cell*, 21(3):421–430, 2011.

[59] Filippo Menolascina. *Synthetic Gene Networks Identification and Control by means of Microfluidic Devices*. Biologia computazionale e bioinformatica, xxiv ciclo, University of Naples "Federico II", 2010/2011.

[60] Fiona M Menzies, Angeleen Fleming, and David C Rubinsztein. Compromised autophagy and neurodegenerative diseases. *Nature Reviews Neuroscience*, 16(6):345–357, 2015.

[61] Noboru Mizushima and Masaaki Komatsu. Autophagy: renovation of cells and tissues. *Cell*, 147(4):728–741, 2011.

[62] G. Napolitano et al. mtor-dependent phosphorylation controls tfeb nuclear export. *Nature communications*, 9(1):1–10, 2018.

[63] Gennaro Napolitano, Chiara Di Malta, Alessandra Esposito, Mariana EG de Araujo, Salvatore Pece, Giovanni Bertalot, Maria Matarese, Valerio Benedetti, Angela Zampelli, Taras Stasyk, et al. A substrate-specific mtorc1 pathway underlies birt-hogg-dubé syndrome. *Nature*, 585(7826):597–602, 2020.

[64] Sara Napolitano. *Analysis and control of biomolecular networks by microfluidics*. Tesi di dottorato in industrial products and process engineering,xxxiii ciclo, University of Naples "Federico II", 2020/2021.

[65] Derek Narendra, Lesley A Kane, David N Hauser, Ian M Fearnley, and Richard J Youle. p62/sqstm1 is required for parkin-induced mitochondrial clustering but not mitophagy; vdac1 is dispensable for both. *Autophagy*, 6(8):1090–1106, 2010.

[66] Michael L Nickerson, Michelle B Warren, Jorge R Toro, Vera Matrosova, Gladys Glenn, Maria L Turner, Paul Duray, Maria Merino, Peter Choyke, Christian P Pavlovich, et al. Mutations in a novel gene lead to kidney tumors, lung wall defects, and benign tumors of the hair follicle in patients with the birt-hogg-dube syndrome. *Cancer cell*, 2(2):157–164, 2002.

[67] Israel C Nnah, Biao Wang, Chaitali Saqcena, Gregory F Weber, Edward M Bonder, Dustin Bagley, Rossella De Cegli, Gennaro Napolitano, Diego L Medina, Andrea Ballabio, et al. Tfeb-driven endocytosis coordinates mtorc1 signaling and autophagy. *Autophagy*, 15(1):151–164, 2019.

[68] Giovanni Marco Nocera, Gaetano Viscido, Stefania Criscuolo, Simona Brillante, Fabrizia Carbone, Leopoldo Staiano, Sabrina Carrella, and Diego di Bernardo. The versalive platform enables microfluidic mammalian cell culture for versatile applications. *Communications Biology*, 5(1):1–9, 2022.

[69] Michela Palmieri, Rituraj Pal, Hemanth R Nelvagal, Parisa Lotfi, Gary R Stinnett, Michelle L Seymour, Arindam Chaudhury, Lakshya Bajaj, Vitaliy V Bondar, Laura Bremner, et al. mtorc1-independent tfeb activation via akt inhibition promotes cellular clearance in neurodegenerative storage diseases. *Nature communications*, 8(1):1–19, 2017.

[70] Giancarlo Parenti, Generoso Andria, and Andrea Ballabio. Lysosomal storage diseases: from pathophysiology to therapy. *Annual review of medicine*, 66:471–486, 2015.

[71] Nunzia Pastore, Keith Blomenkamp, Fabio Annunziata, Pasquale Piccolo, Pratibha Mithbaokar, Rosa Maria Sepe, Francesco Vetrini, Donna Palmer, Philip Ng, Elena Polishchuk, et al. Gene transfer of master autophagy regulator tfeb results in clearance of toxic protein and correction of hepatic disease in alpha-1-anti-trypsin deficiency. *EMBO molecular medicine*, 5(3):397–412, 2013.

[72] Rushika M Perera, Svetlana Stoykova, Brandon N Nicolay, Kenneth N Ross, Julien Fitamant, Myriam Boukhali, Justine Lengrand, Vikram Deshpande, Martin K Selig, Cristina R Ferrone, et al. Transcriptional control of autophagy–lysosome function drives pancreatic cancer metabolism. *Nature*, 524(7565):361–365, 2015.

[73] Vinicia A Polito, Hongmei Li, Heidi Martini-Stoica, Baiping Wang, LI Yang, Yin Xu, Daniel B Swartzlander, Michela Palmieri, Alberto Di Ronza, Virginia M-Y Lee, et al. Selective clearance of aberrant tau proteins and rescue of neurotoxicity by transcription factor eb. *EMBO molecular medicine*, 6(9):1142–1160, 2014.

[74] L. Postiglione et al. From a discrete to continuous actuation for improved real-time control of gene expression in mammalian cells. *IFAC-PapersOnLine*, 49(26):14–19, 2016.

[75] L. Postiglione et al. Regulation of gene expression and signaling pathway activity in mammalian cells by automated microfluidics feedback control. *ACS synthetic biology*, 7(11):2558–2565, 2018.

[76] Rosa Puertollano, Shawn M Ferguson, James Brugarolas, and Andrea Ballabio. The complex relationship between tfeb transcription factor phosphorylation and subcellular localization. *The EMBO journal*, 37(11):e98804, 2018.

[77] S. J. Rahi et al. Oscillatory stimuli differentiate adapting circuit topologies. *Nature methods*, 14(10):1010–1016, 2017.

[78] Laura R Rega, Elena Polishchuk, Sandro Montefusco, Gennaro Napolitano, Giulia Tozzi, Jinzhong Zhang, Francesco Bellomo, Anna Taranta, Anna Pastore, Roman Polishchuk, et al. Activation of the transcription factor eb rescues lysosomal abnormalities in cystinotic kidney cells. *Kidney international*, 89(4):862–873, 2016.

[79] Agnes Roczniak-Ferguson, Constance S Petit, Florian Froehlich, Sharon Qian, Jennifer Ky, Brittany Angarola, Tobias C Walther, and Shawn M Ferguson. The transcription factor tfeb links mtorc1 signaling to transcriptional control of lysosome homeostasis. *Science signaling*, 5(228):ra42–ra42, 2012.

[80] I. Ruolo et al. Tfeb dynamical model reveals a novel feedback loop biological mechanism. *IFAC-PapersOnLine*, 52(26):213–218, 2019.

[81] I. Ruolo et al. Elucidation of tfeb nuclear translocation dynamics in human cells by means of quantitative modelling and microfluidics. *IFAC-PapersOnLine*, In Press, 2022.

[82] H Sakamoto, K Yamashita, K Okamoto, T Kadowaki, E Sakai, M Umeda, and T Tsukuba. Transcription factor eb influences invasion and migration in oral squamous cell carcinomas. *Oral Diseases*, 24(5):741–748, 2018.

[83] C. Salazar et al. Allosteric regulation of the transcription factor nfat1 by multiple phosphorylation sites: a mathematical analysis. *Journal of molecular biology*, 327(1):31–45, 2003.

[84] Yasemin Sancak, Liron Bar-Peled, Roberto Zoncu, Andrew L Markhard, Shigeyuki Nada, and David M Sabatini. Ragulator-rag complex targets mtorc1 to the lysosomal surface and is necessary for its activation by amino acids. *Cell*, 141(2):290–303, 2010.

[85] Yasemin Sancak, Timothy R Peterson, Yoav D Shaul, Robert A Lindquist, Carson C Thoreen, Liron Bar-Peled, and David M Sabatini. The rag gtpases bind raptor and mediate amino acid signaling to mtorc1. *Science*, 320(5882):1496–1501, 2008.

[86] Marco Sardiello, Michela Palmieri, Alberto Di Ronza, Diego Luis Medina, Marta Valenza, Vincenzo Alessandro Gennarino, Chiara Di Malta, Francesca Donaudy, Valerio Embrione, Roman S Polishchuk, et al. A gene network regulating lysosomal biogenesis and function. *Science*, 325(5939):473–477, 2009.

[87] S Schenone, C Brullo, F Musumeci, M Radi, and M Botta. Atp-competitive inhibitors of mtor: an update. *Current medicinal chemistry*, 18(20):2995–3014, 2011.

[88] Tilman Schneider-Poetsch, Jianhua Ju, Daniel E Eyler, Yongjun Dang, Shridhar Bhat, William C Merrick, Rachel Green, Ben Shen, and Jun O Liu. Inhibition of eukaryotic translation elongation by cycloheximide and lactimidomycin. *Nature chemical biology*, 6(3):209–217, 2010.

[89] C. Settembre et al. Tfeb regulates autophagy: an integrated coordination of cellular degradation and recycling processes. *Autophagy*, 7(11):1379–1381, 2011.

[90] Carmine Settembre, Rossella De Cegli, Gelsomina Mansueto, Pradip K Saha, Francesco Vetrini, Orane Visvikis, Tuong Huynh, Annamaria Carissimo, Donna Palmer, Tiemo Jürgen Klisch, et al. Tfeb controls cellular lipid metabolism through a starvation-induced autoregulatory loop. *Nature cell biology*, 15(6):647–658, 2013.

[91] Carmine Settembre, Roberto Zoncu, Diego L Medina, Francesco Vetrini, Serkan Erdin, SerpilUckac Erdin, Tuong Huynh, Mathieu Ferron, Gerard Karsenty, Michel C

Vellard, et al. A lysosome-to-nucleus signalling mechanism senses and regulates the lysosome via mtor and tfeb. *The EMBO journal*, 31(5):1095–1108, 2012.

[92] Youbao Sha, Lang Rao, Carmine Settembre, Andrea Ballabio, and N Tony Eissa. Stub 1 regulates tfeb-induced autophagy–lysosome pathway. *The EMBO journal*, 36(17):2544–2552, 2017.

[93] Ju-Xian Song, Yue-Ru Sun, Ivana Peluso, Yu Zeng, Xing Yu, Jia-Hong Lu, Zheng Xu, Ming-Zhong Wang, Liang-Feng Liu, Ying-Yu Huang, et al. A novel curcumin analog binds to and activates tfeb in vitro and in vivo independent of mtor inhibition. *Autophagy*, 12(8):1372–1389, 2016.

[94] Wensi Song, Fan Wang, Marzia Savini, Ashley Ake, Alberto Di Ronza, Marco Sardiello, and Laura Segatori. Tfeb regulates lysosomal proteostasis. *Human molecular genetics*, 22(10):1994–2009, 2013.

[95] Carmine Spampanato, Erin Feeney, Lishu Li, Monica Cardone, Jeong-A Lim, Fabio Annunziata, Hossein Zare, Roman Polishchuk, Rosa Puertollano, Giancarlo Parenti, et al. Transcription factor eb (tfeb) is a new therapeutic target for pompe disease. *EMBO molecular medicine*, 5(5):691–706, 2013.

[96] Abraham D Stroock, Stephan KW Dertinger, Armand Ajdari, Igor Mezic, Howard A Stone, and George M Whitesides. Chaotic mixer for microchannels. *Science*, 295(5555):647–651, 2002.

[97] Anderson Tan, Renuka Prasad, Chaerin Lee, and Eek-hoon Jho. Past, present, and future perspectives of transcription factor eb (tfeb): Mechanisms of regulation and association with disease. *Cell Death & Differentiation*, 29(8):1433–1449, 2022.

[98] Nestor V Torres and Guido Santos. The (mathematical) modeling process in biosciences. *Frontiers in Genetics*, 6:354, 2015.

[99] Taiji Tsunemi, Travis D Ashe, Bradley E Morrison, Kathryn R Soriano, Jonathan Au, Ruben A Vázquez Roque, Eduardo R Lazarowski, Vincent A Damian, Eliezer Masliah, and Albert R La Spada. Pgc-1α rescues huntington's disease proteotoxicity

by preventing oxidative stress and promoting tfeb function. *Science translational medicine*, 4(142):142ra97–142ra97, 2012.

[100] Ivan Tyukin. *The problem of adaptation in dynamical systems*, page 44–80. Cambridge University Press, 2011.

[101] Silvia Vega-Rubin-de Celis, Samuel Peña-Llopis, Meghan Konda, and James Brugarolas. Multistep regulation of tfeb by mtorc1. *Autophagy*, 13(3):464–472, 2017.

[102] Marc Vidal. A unifying view of 21st century systems biology. *FEBS letters*, 583(24):3891–3894, 2009.

[103] Rose Willett, José A Martina, James P Zewe, Rachel Wills, Gerald RV Hammond, and Rosa Puertollano. Tfeb regulates lysosomal positioning by modulating tmem55b expression and jip4 recruitment to lysosomes. *Nature communications*, 8(1):1–17, 2017.

[104] Qingli Xiao, Ping Yan, Xiucui Ma, Haiyan Liu, Ronaldo Perez, Alec Zhu, Ernesto Gonzales, Jack M Burchett, Dorothy R Schuler, John R Cirrito, et al. Enhancing astrocytic lysosome biogenesis facilitates aβ clearance and attenuates amyloid plaque pathogenesis. *Journal of Neuroscience*, 34(29):9607–9620, 2014.

[105] Qingli Xiao, Ping Yan, Xiucui Ma, Haiyan Liu, Ronaldo Perez, Alec Zhu, Ernesto Gonzales, Danielle L Tripoli, Leah Czerniewski, Andrea Ballabio, et al. Neuronal-targeted tfeb accelerates lysosomal degradation of app, reducing aβ generation and amyloid plaque pathogenesis. *Journal of Neuroscience*, 35(35):12137–12151, 2015.

[106] Lan Xu and Joan Massagué. Nucleocytoplasmic shuttling of signal transducers. *Nature reviews Molecular cell biology*, 5(3):209–219, 2004.

[107] Nissan Yissachar, Tali Sharar Fischler, Ariel A Cohen, Shlomit Reich-Zeliger, Dor Russ, Eric Shifrut, Ziv Porat, and Nir Friedman. Dynamic response diversity of nfat isoforms in individual living cells. *Molecular cell*, 49(2):322–330, 2013.

[108] P. A. M. Zapata et al. Time course decomposition of cell heterogeneity in tfeb signaling states reveals homeostatic mechanisms restricting the magnitude and duration of tfeb responses to mtor activity modulation. *BMC cancer*, 16(1):1–19, 2016.

[109] Zengli Zhang, Hongfeng Wang, Qifeng Ding, Yufei Xing, Delai Xu, Zhonghua Xu, Tong Zhou, Bin Qian, Chenghong Ji, Xue Pan, et al. The tumor suppressor p53 regulates autophagosomal and lysosomal biogenesis in lung cancer cells by targeting transcription factor eb. *Biomedicine & Pharmacotherapy*, 89:1055–1060, 2017.

[110] Roberto Zoncu, Liron Bar-Peled, Alejo Efeyan, Shuyu Wang, Yasemin Sancak, and David M Sabatini. mtorc1 senses lysosomal amino acids through an inside-out mechanism that requires the vacuolar h+-atpase. *Science*, 334(6056):678–683, 2011.

Acknowledgments

I express my gratitude to the individuals who provided valuable assistance during my doctoral studies. I would like to begin by extending my appreciation to my supervisor, Professor Diego di Bernardo, for granting me this opportunity. Moreover, I would like to acknowledge the contribution of all those who collaborated with me on this project during my tenure as a PhD candidate, including Sara Napolitano, Lorena Postiglione, Barbara Tumaini, Stefania Criscuolo, Gianpio Caringella, and Gianmarco Nocera. I am also grateful to all members of the di Bernardo and Gambardella Labs, with whom I have shared the last three years of my PhD program and beyond.

Furthermore, I offer sincere thanks to the professors and researchers at Tigem who provided their support and guidance during the project, particularly Professor Andrea Ballabio, Professor Gennaro Napolitano, Professor Carmine Settembre, Professor Diego Medina, Professor Luis Galietta, and Mr. Michele Genovese. All of these individuals have contributed significantly to my personal and professional development.

Finally, I acknowledge the generous support provided by the Italian Telethon Foundation, the Dept. of Chemical, Materials and Industrial Engineering of the Unviersity of Naples "Federico II", and the European Project iPC: Pediatric Cure, without which this work would not have been possible.